

POLITECNICO DI TORINO
CENTRE D'ÉNERGÉTIQUE ET DE
THERMIQUE DE LYON (CETHIL)

Master of Science in Energy and Nuclear Engineering

Master Thesis

**Thermal characterization of MOFs for
thermal energy storage**



Supervisors:

Prof. Pietro ASINARI (POLITO, Torino)

Prof. Kevyn JOHANNES (INSA, Lyon)

Candidate:
Noemi FERRIGNO

Academic year 2018/2019

To all the children that in these years
crossed the Mediterranean Sea,
with all their dreams and wishes,
but weren't able to make it.
"Where you live should not decide
whether you live or whether you die"
but unfortunately this is still true
and their broken dreams are proof.
Every effort I did for this thesis
is devoted to them,
who remind me every day how lucky I am.

Acknowledgments

First of all I would like to sincerely thank my supervisor Dr. Pietro Asinari, who gave me the opportunity to get in touch with CETHIL (Centre d'énergétique et de thermique de Lyon) at INSA de Lyon (Institut National des Sciences Appliquées de Lyon) and apply for an exchange program aimed at drafting my master thesis.

I would like to express my gratitude to my supervisor Dr. Kévyne Johannes and to the director of CETHIL, Dr. Frédéric Kuznik, who welcomed me in their team and gave me the opportunity to work on such fascinating investigation on recently developed adsorbent materials for thermal energy storage, namely Metal-organic frameworks. Thank you for making me available the experimental laboratory and all the devices I needed to develop MOFs thermal characterization.

I am especially indebted to a team member, the post-doctorant Larysa Okhrimenko, who was directly involved in all particularities of my everyday research work. I am infinitely grateful for your immense help and support, your patience, your scientific suggestions and all your time you devoted to discussions and analysis of experimental results.

I also would like to thank SUBATECH (Laboratoire de Physique Subatomique et des Technologies Associées) of Nantes, and in particular the post-doctorant Denys Grekov for his essential cooperation in performing nitrogen adsorption isotherms on my samples.

Finally, I would like to sincerely express my gratitude to our prestigious institute, the Polytechnic of Turin, and all the highly qualified teachers and at the same time admirable people that I was lucky to meet in this five-years path. I thank them to let me grow up, teaching me how big the power of knowledge is and how important enthusiasm and dedication are.

Abstract

Nowadays the integration of thermal energy storage (TES) into HVAC systems seems to play a key role in determining a decrease in heating and cooling energy needs in the buildings sector, which will keep growing. Indeed, TES systems allow to decouple generation and demand for heat, power and cooling and to store renewable solar energy, dealing with its intermittency, improving energy efficiency systems and thus leading to a reduction in fossil fuel energy consumption and GHG emissions.

The current state of the art of energy storage technologies requires the design of novel adsorbents to achieve relevant improvements in this field.

Metal-Organic Frameworks (MOFs) are a new class of porous crystalline materials that are organized by the coordination between inorganic metal units and organic ligands. They are particularly attractive because of their tunable amphiphilic character, pore volume, pore size and specific surface area by changing the chemical constituents or adding functionalized linkers. Moreover, they show low desorption temperature and faster kinetics than other physical or chemical adsorbents.

In this work, a series of water stable MOFs have been investigated in order to choose which to synthesize and test. Firstly, screening their energy storage capacity and desorption temperature, compared to those of other adsorbent materials, MOFs and MOF-based composites were found to exhibit the highest energy density at the lowest desorption temperature. Then, since experimental data from literature were found at closed system testing conditions, it was decided to test the most promising ones under open system conditions.

The work was focused on the first exploitation of pristine MIL-125-NH₂ and two composites, MIL-125-NH₂ + (45%)CaCl₂ and MIL-125-NH₂ + (45%)SrBr₂. After synthesis, it was performed X-ray powder diffraction to verify the actual chemical composition of materials, nitrogen adsorption isotherms to assess pore volume, pore size and specific surface area and TG-DSC tests, i.e. simultaneous thermogravimetric and differential scanning calorimetric tests, to both calculate the energy storage capacity and carry out hydrothermal stability and kinetics analyses.

On one hand, results highlight the strong impact that specific surface area has on adsorption properties of MOFs. A decrease of this parameter can badly affect the water uptake and energy storage capacity, as in the case of MIL-125-NH₂.

On the other hand, MOF-based composites confirm their outstanding adsorption properties, showing higher water uptake and energy density values, even if at the expense of kinetics, with respect to the pristine MOF and still keeping lower desorption temperatures than the ones for inorganic salts.

All the materials tested, as expected from literature data, show high hydrothermal stability, which makes them interestingly suitable for thermal energy storage applications.

Contents

Abstract	IV
List of Tables	VII
List of Figures	VIII
Introduction	1
1 The role of thermal energy storage in EU's energy transition	3
1.1 Overview on the present and future energy scenarios	3
1.2 Heating and cooling end-uses impact and the role of the building	4
1.3 Potential for thermal energy storage systems	5
2 Thermal energy storage: the state of the art	7
2.1 General introduction	7
2.2 Sensible heat storage	9
2.2.1 Working principle	9
2.2.2 Materials	9
2.2.3 Sensible TES case study	10
2.3 Latent heat storage	12
2.3.1 Working principle	12
2.3.2 Materials	13
2.3.3 Latent TES case study	14
2.4 Thermochemical or sorption heat storage	15
2.4.1 Terminology	16
2.4.2 Classifications and working principle	16
2.4.3 Materials	20
2.4.4 Thermochemical ES case study	26
2.5 Why decide to study and test metal-organic frameworks?	27
3 Metal-organic frameworks for thermal energy storage	31
3.1 MOFs: the state of the art	31
3.1.1 MOF/H ₂ O working pair: adsorption thermodynamics	32
3.1.2 How to tune adsorption properties on MOFs	37
3.1.3 MOFs hydrothermal stability	41
3.2 MOFs and adsorptive thermal energy storage: the choice	47
3.2.1 Adsorbent selection criteria for TES	47
3.2.2 Selection criteria applied to MOFs: the steps of choice	50

4	Experimental methods	61
4.1	Materials development	61
4.1.1	Chemical constituents	61
4.1.2	Synthesis and activation	62
4.2	Characterization at microscopic scale	63
4.2.1	XRPD	63
4.2.2	Adsorption isotherms	65
4.2.3	TG-DSC analysis	67
4.2.4	Hydrothermal stability	71
4.2.5	Kinetics	72
5	Results and discussion	75
5.1	X-ray diffraction results and discussion	75
5.1.1	(1)MIL-125-NH ₂ and CaCl ₂ -based composite	75
5.1.2	(2)MIL-125-NH ₂ and SrBr ₂ -based composite	76
5.2	Adsorption isotherms results and discussion	77
5.3	TGA/DSC results and discussion	80
5.3.1	Water uptake and energy storage capacity	80
5.3.2	Hydrothermal stability	85
5.3.3	Adsorption kinetics	90
	Conclusions	97
	Annex A	101
	Bibliography	105

List of Tables

2.1	Desirable properties of sensible heat storage materials	9
2.2	Desirable properties of latent heat storage materials	13
2.3	Harp Brewery energy system technical data [10]	15
2.4	Details of literature data of different adsorption materials categories, also shown in Fig. 2.13 (*energy density expressed in kWh/m ³ , thus not plotted in Fig. 2.13).	29
3.1	The minimal desorption temperature and corresponding relative pressure of water vapor (in parentheses) [36].	49
3.2	Adsorbent selection criteria for open and closed TES - space heating application.	50
3.3	MOF selection - pore and surface characteristics and adsorption behavior from water adsorption isotherms at 298 K (^a position of steep increase in water uptake from adsorption isotherms).	51
3.4	MOF selection - adsorption properties at test conditions (^a heat of adsorption from Henninger et al. [43]; ^b energy storage capacity calculated).	51
4.1	Ti-MIL-125-NH ₂ chemical constituents [39].*quantities multiplied by five wrt ref.	61
4.2	Ti-MIL-125-NH ₂ +(45%)CaCl ₂ composite chemical constituents [19].	61
4.3	Ti-MIL-125-NH ₂ +(45%)SrBr ₂ composite chemical constituents.	62
4.4	TGA-DSC set-up for thermal analysis.	70
5.1	Porosimetry values by nitrogen adsorption isotherms at 77 K (^a at a relative pressure 0.175; ^b at a relative pressure 0.150).	77
5.2	TG-DSC results - water uptake and energy storage capacity (^a at first cycle).	80
5.3	TG-DSC results - hydrothermal stability (^a after six cycles).	85

List of Figures

1.1	Fuel mix (left) and carbon emissions (right) - ET scenario [2]	4
1.2	Final energy demand for EU28 by end-use for H/C in all sectors in 2012 [TWh] [3]	4
1.3	Final energy demand for EU28 for H/C by end-use and sector [TWh] in 2012 [3]	5
1.4	Seasonal shift between solar irradiation and heat demand (University of Technology Eindhoven, 2012)	6
2.1	Energy density of high energy storage methods (left); Volume required to store 1850 kWh (With consideration of 25% heat losses, based on a 70 °C temperature increase for water) (right) [5, 11].	8
2.2	Main concepts for seasonal thermal energy storage [9].	10
2.3	Simplified schematic of the principal energy components in the DLSC (Courtesy of DLSC) [10].	11
2.4	Classification of phase change materials [7].	13
2.5	(a) The nodule for STL system (Courtesy of Cristopia Energy Systems), and (b) a capsule for the new STL latent TES (Courtesy of Mitsubishi Chemical Co.) [10].	15
2.6	Sorption thermal storage classification [5].	17
2.7	Operation principle of closed sorption thermal storage system [5].	18
2.8	Operation principle of open sorption thermal storage system [5].	19
2.9	The working principle of a composite adsorbent [12], with permission from Springer Nature, 2007.	25
2.10	Thermal energy storage concept: discharging phase during winter (left) and charging phase during summer (right). [16].	26
2.11	Isotherms of sorption and desorption at 25 °C of the zeolite and ZM15 - Belsorp Analyzer [33].	27
2.12	Experimental setup for hydration tests [16].	27
2.13	Energy storage capacity of sorption materials as a function of desorption temperature. Graph adjusted from Fig. 8 [5].	28
3.1	Prototypical linkers with selected metal nodes and secondary building units in corresponding MOFs (with acronyms) [19, 35].	32
3.2	Adsorption isotherms - Brunauer classification	37
3.3	Water adsorption isotherms at 298 K on isorecticular CPO-27 solids: (left) Ni-CPO-27 and (right) Mg-CPO-27 [37].	38

3.4	Water adsorption isotherms at 298 K of: (left) Ti-MIL-125 (square) and Ti-MIL-125-NH ₂ (circle)[38] and (right) two consecutive water adsorption/desorption cycles for UiO-66 (regeneration at 353 K under an inert atmosphere) [37].	38
3.5	Water adsorption isotherms at 298 K of: (left) MIL-100 made from Fe ³⁺ , Cr ³⁺ or Al ³⁺ and (right) Cr-MIL-101 [37].	39
3.6	Water adsorption isotherms at 298 K of: (left) Cr-MIL-101 and (right) Cr-MIL-101-NH ₂ (square) and Cr-MIL-101-NO ₂ (circle). The full and empty symbols are the adsorption and desorption branches, respectively [38].	40
3.7	Water adsorption isotherms at 298 K of: (left) Zr-UiO-66 (square) and Zr-UiO-66-NH ₂ (circle); (right) Ti-MIL-125 (square) and Ti-MIL-125-NH ₂ (circle). The full and empty symbols correspond to the adsorption and desorption branches, respectively [38].	41
3.8	Steam stability map of MOFs [37].	43
3.9	PXRD patterns before and after exposure to water vapor and subsequent reactivation [40].	43
3.10	Stability under numerous adsorption–desorption cycles (p $\frac{1}{4}$ 12.5 mbar) of (a) MIL-100(Fe)/CaCl ₂ (46 wt%) and (b) MIL-101(Cr)/ CaCl ₂ (62 wt%) [19].	44
3.11	Hydrothermal cycle stress tests with temperature profile and load signal of (a) H ₂ N-UiO-66 and (b) H ₂ N-MIL-125 [42].	45
3.12	Thermogravimetric analysis profile for multiple cycles of water adsorption-desorption of MIL-160. Test conditions: adsorption at 303 K in humid nitrogen (RH 80%) and desorption at 373 K in nitrogen (RH 0.03%) [48].	45
3.13	Thermogravimetric cycling test of CAU-10-H at constant humidity [46].	46
3.14	Temperature profile and load signal of the MIL-100(Fe) cycling experiment, acquired at p = 5.6 kPa [50].	46
3.15	The van’t Hoff diagram of the ideal cycle [43].	49
3.16	(Above) Structure of MIL-100(Fe): Iron atoms are shown in orange, oxygen in red and carbon in grey; (below) Structure of MIL-101(Cr) representing two mesoporous cages of 2.9 nm and 3.4 nm: Chromium atoms are shown in grey and others (carbon and oxygen) in black [45].	52
3.17	Water adsorption and desorption isotherms at 25 °C: (left) MIL-100 [19] and (right) MIL-101 [43].	53
3.18	(Left) UiO-66-NH ₂ : Zirconium atoms are shown in Cambridge blue, oxygen in red, nitrogen in Oxford blue and carbon in grey; (right) MIL-125-NH ₂ : Titanium atoms are shown in orange, oxygen in red, nitrogen in Oxford blue and carbon in grey [45].	53
3.19	Water adsorption and desorption isotherms at 25 °C of UiO-66 (in violet), UiO-66(Zr)-NH ₂ (in red) and MIL-125-NH ₂ (in blue); (Adsorption: filled symbols; desorption: empty symbols) [42].	54
3.20	(Left) CAU-10(Al): Aluminum atoms are shown in blue, oxygen in red and carbon in grey; (right) MIL-160(Al): Aluminum atoms are shown in rose, oxygen in red and carbon in grey [45].	55
3.21	Water adsorption and desorption isotherms: (left) CAU-10 at 25 °C (red), 40 °C (black) and 60 °C (blu) [42]; (right) MIL-160 (Adsorption: filled symbols; desorption: empty symbols) [48].	55

3.22	Crystal structure of CPO-27(Ni) with the adsorbed water molecules (H, O, C, Ni are in white, red, grey and violet respectively) [23].	56
3.23	Water adsorption and desorption isotherms of CPO-27(Ni) at 25 °C [47].	57
3.24	Water uptake capacity of water stable and recyclable MOFs in different pressure ranges: 0-0.1; 0.1-0.3; 0.3-0.5. The large portion of water uptake capacity indicates that the pore filling or condensation occurs in this pressure range. [45].	59
4.1	MIL-125-NH ₂ sample 1 (left), anhydrous CaCl ₂ (middle), MIL-125-NH ₂ +(45%)CaCl ₂ composite (right).	62
4.2	MIL-125-NH ₂ sample 2 (left), anhydrous SrBr ₂ (middle), MIL-125-NH ₂ +(45%)SrBr ₂ composite (right).	63
4.3	Powder diffractometer.	64
4.4	Bragg's low illustration.	64
4.5	Cross-sectional view of the configuration of adsorbate molecules in a cylindrical pore of radius L. [52].	66
4.6	SETARAM SETSYS evo TG-DSC analyzer (left) and its internal composition (right).	68
4.7	SETARAM WETSYS controlled humidity generator (left) and its schematic working principle (right).	68
4.8	Schematic temperature pattern (pressure specification) - TGA/DSC tests.	69
4.9	Schematic temperature pattern - TGA/DSC cyclability tests.	71
4.10	Schematic temperature pattern (pressure specification) - TGA/DSC kinetics tests.	72
5.1	XPRD patterns: comparison between MIL-125-NH ₂ + (45%)CaCl ₂ (black) and MIL-125-NH ₂ sample 1 (red); CaCl ₂ in green.	75
5.2	XPRD patterns: comparison between MIL-125-NH ₂ + (45%)SrBr ₂ (black) and MIL-125-NH ₂ sample 2 (red); SrBr ₂ in green.	76
5.3	Nitrogen adsorption-desorption isotherms of (1)MIL-125-NH ₂ at 77 K.	78
5.4	Nitrogen adsorption-desorption isotherms of (2)MIL-125-NH ₂ at 77 K.	78
5.5	Nitrogen adsorption-desorption isotherms of MIL-125-NH ₂ + CaCl ₂ at 77 K.	79
5.6	Nitrogen adsorption-desorption isotherms of MIL-125-NH ₂ + SrBr ₂ at 77 K.	79
5.7	(1)MIL-125-NH ₂ first adsorption/desorption cycle: T _{ads} =20 °C, p/p ₀ =0.5, T _{des} =80 °C, p/p ₀ =0.0003.	81
5.8	(1)MIL-125-NH ₂ heat of adsorption at first cycle.	82
5.9	MIL-125-NH ₂ + CaCl ₂ first adsorption/desorption cycle: T _{ads} =20 °C, p/p ₀ =0.5, T _{des} =80 °C, p/p ₀ =0.0003.	83
5.10	MIL-125-NH ₂ + CaCl ₂ heat of adsorption at first cycle.	83
5.11	MIL-125-NH ₂ + SrBr ₂ first adsorption/desorption cycle: T _{ads} =20 °C, p/p ₀ =0.5, T _{des} =80 °C, p/p ₀ =0.0003.	85
5.12	MIL-125-NH ₂ + SrBr ₂ heat of adsorption at first cycle.	86
5.13	(1)MIL-125-NH ₂ cyclability test upon six adsorption/desorption cycles with T _{ads} 20 °C, p/p ₀ =0.5, T _{des} 80 °C, p/p ₀ =0.0003.	87
5.14	(1)MIL-125-NH ₂ heat of adsorption after six consecutive adsorption/desorption cycles.	88
5.15	MIL-125-NH ₂ +CaCl ₂ cyclability test upon six adsorption/desorption cycles with T _{ads} 20 °C, p/p ₀ =0.5, T _{des} 80 °C, p/p ₀ =0.0003.	89

5.16 MIL-125-NH ₂ +CaCl ₂ heat of adsorption after six consecutive adsorption/desorption cycles.	89
5.17 MIL-125-NH ₂ +SrBr ₂ cyclability test upon six adsorption/desorption cycles with T _{ads} 20 °C, p/p ₀ =0.5, T _{des} 80 °C, p/p ₀ =0.0003.	90
5.18 MIL-125-NH ₂ +Srbr ₂ heat of adsorption after six consecutive adsorption/desorption cycles.	91
5.19 (1)MIL-125-NH ₂ adsorption kinetics at three different pressure levels (T _{ads} = 20 °C).	92
5.20 (1)MIL-125-NH ₂ adsorption at T _{ads} = 20 °C, p _{ads} = 18.5 mbar: water condensation in micropores.	93
5.21 MIL-125-NH ₂ +CaCl ₂ adsorption kinetics at three different pressure levels (T _{ads} = 20 °C).	94
5.22 MIL-125-NH ₂ +CaCl ₂ adsorption at T _{ads} = 20 °C, p _{ads} = 18.5 mbar: water condensation in micropores.	94
5.23 MIL-125-NH ₂ +SrBr ₂ adsorption kinetics at three different pressure levels (T _{ads} = 20 °C).	95
5.24 MIL-125-NH ₂ +SrBr ₂ adsorption at T _{ads} = 20 °C, p _{ads} = 18.5 mbar: water condensation in micropores.	96
5.25 Adsorption kinetics comparison between all the samples: T _{ads} = 20 °C, p _{ads} = 11.6 mbar.	96
5.26 XPRD pattern of MIL-125-NH ₂ sample 1.	101
5.27 XPRD pattern of MIL-125-NH ₂ sample 2.	102
5.28 XPRD pattern of MIL-125-NH ₂ + (45%)CaCl ₂ composite (CaCl ₂ in green).	102
5.29 XPRD pattern of MIL-125-NH ₂ + (45%)SrBr ₂ composite (SrBr ₂ in green).	103
5.30 XPRD patterns: comparison between MIL-125-NH ₂ + (45%)CaCl ₂ (black) and MIL-125-NH ₂ sample 1 (red); CaCl ₂ in green.	103
5.31 XPRD patterns: comparison between MIL-125-NH ₂ + (45%)SrBr ₂ (black) and MIL-125-NH ₂ sample 2 (red); SrBr ₂ in green.	104

Nomenclature

ΔG_{ads} Differential adsorption Gibbs free energy $\left[\frac{\text{kJ}}{\text{mol}}\right]$

ΔH Differential adsorption molar enthalpy $\left[\frac{\text{kJ}}{\text{mol}}\right]$

ΔH_{ads} Differential heat of adsorption $\left[\frac{\text{J}}{g_{\text{water}}}\right]$

ΔS Differential adsorption molar entropy $\left[\frac{\text{kJ}}{\text{mol}\cdot\text{K}}\right]$

λ Thermal conductivity $\left[\frac{\text{W}}{\text{m}\cdot\text{K}}\right]$

ϕ Pore width [nm]

ρ_{pack} Packing density $\left[\frac{g_{\text{ads}}}{\text{m}^3_{\text{ads}}}\right]$

$\rho_{\text{Q-m}}$ Energy storage capacity $\left[\frac{\text{Wh}}{\text{kg}}\right]$

$\rho_{\text{Q-m}}$ Energy storage density $\left[\frac{\text{kWh}}{\text{m}^3}\right]$

c_p Specific heat capacity $\left[\frac{\text{kJ}}{\text{kg}\cdot\text{K}}\right]$

L Specific latent heat $\left[\frac{\text{kJ}}{\text{kg}}\right]$

p_{ads} Adsorption temperature [kPa] or [mbar]

q_{st} Isostatic heat of adsorption $\left[\frac{\text{kJ}}{\text{mol}}\right]$

s Specific molar entropy $\left[\frac{\text{kJ}}{\text{mol}\cdot\text{K}}\right]$

T_{ads} Adsorption temperature [°C]

T_{des} Desorption temperature [°C]

$T_{\text{max,dehyd}}$ Dehydration temperature [°C]

v Specific molar volume $\left[\frac{\text{m}^3}{\text{mol}}\right]$

x Working capacity $\left[\frac{g_{\text{adsorbed}}}{g_{\text{sorbent}}}\right]$

x_{cycl} Cycling loading lift $\left[\frac{g_{\text{exchanged}}}{g_{\text{sorbent}}}\right]$

Introduction

To cut back both on conventional sources of energy and green house gases emissions and to deal with the increasing energy demand: those are the main issues in the EU's energy transition.

Since the heating and cooling sector is responsible for half of all consumed final energy in Europe and the 85% of the energy demand is fulfilled by fossil fuels, substantial measures to steer energy sources toward renewable energy in that field seems to be the fastest way to reach Europe's sustainability goals. In particular, 45% of energy for heating and cooling in the EU is used in the residential sector, thus allowing us to focus efforts on buildings energy consumption [1].

Solar energy is considered as one of the most promising substitutes for traditional energy sources. However, new challenges in terms of intermittent sources management and grid balancing come from the integration of a higher share of non-dispatchable renewable energy sources into power, heating and cooling infrastructure [1].

Energy storage will play a key role in providing the required flexibility and reducing that mismatch between energy supply and energy demand. This is true especially for thermal energy storage at different scales: at larger scale for district heating/cooling networks and industrial applications, but also at smaller scale for commercial and residential buildings [1].

In the past few decades, focusing attention on thermal energy storage (TES) integrated into HVAC (Heating, Ventilation and Air Conditioning) systems, sorption heat storage was discovered to be particularly interesting and adsorbent materials more and more suitable are being studying and testing.

The aim of this thesis was to investigate the thermal properties and potential of recently developed adsorbent materials, namely Metal-organic frameworks (MOF), for thermal energy storage and perform a thermal characterization on the most promising ones.

After briefly scanning the potential for thermal energy storage systems in Europe's energy transition (chapter 1) and a literature review on their present developments (chapter 2), a deepening on MOFs was undertaken in order to make a choice (chapter 3). Since, after this screening, it has been pointed out a lack of knowledge on MOFs performances upon open systems operating conditions, it was decided to deepen in that direction. Pristine MIL-125-NH₂ and two composite, MIL-125-NH₂+(45%)CaCl₂ and MIL-125-NH₂+(45%)SrBr₂ have been characterized. The methodology and set-up of each test are described in chapter 4 and the results are shown and discussed in chapter 5.

After synthesis, for each sample, it was performed X-ray powder diffraction to verify the actual chemical composition of materials, nitrogen adsorption isotherms to assess pore volume, pore size and specific surface area and TG-DSC tests, i.e. simultaneous thermogravimetric and differential scanning calorimetric tests, to both calculate the energy

storage capacity and carry out hydrothermal stability and kinetics analyses.

Chapter 1

The role of thermal energy storage in EU's energy transition

In this chapter, the potential for thermal energy storage systems in the present and future Europe's energy transition to a lower carbon economy will be briefly explained.

1.1 Overview on the present and future energy scenarios

According to the “Evolving Transition” (ET) scenario [2], which assumes that government policies, technology and social preferences continue to evolve in a manner and speed seen over the recent past:

- global GDP is projected to grow at a similar rate to past 25 years, driven by increasing prosperity in the developing world;
- increasing global prosperity will drive growth in energy demand, partly offset by more rapid falls in energy intensity (energy used per unit of GDP): global GDP more than doubles over the Outlook, but energy consumption increases by only 35%;
- the gradual transition in the fuel mix is set to continue with renewables (see Fig. 1.1), expected to account for half of the growth in energy supplies over the next 20 years with the fastest rate of growth (7% p.a.): this leads to the most diversified fuel mix ever seen but also to concerns about grid balancing and intermittency of the source;
- carbon emissions from energy use continue to grow, increasing by around 10% by 2040, far slower than that seen in the past 25 years, when carbon emissions increased by 55%.

As shown in Fig. 1.1, even if this slowdown in carbon emissions growth, the trend is not sufficient to reach the Paris climate goals, thus underlining the need for a decisive strategy that allows to significantly cut back on emissions [2].

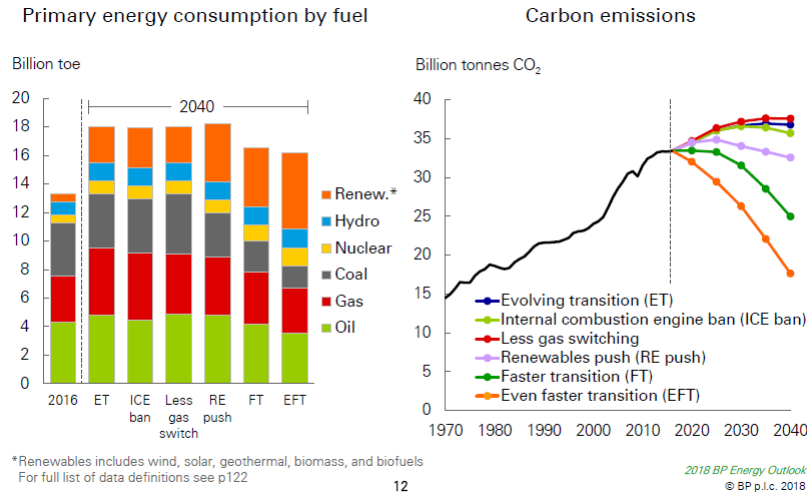
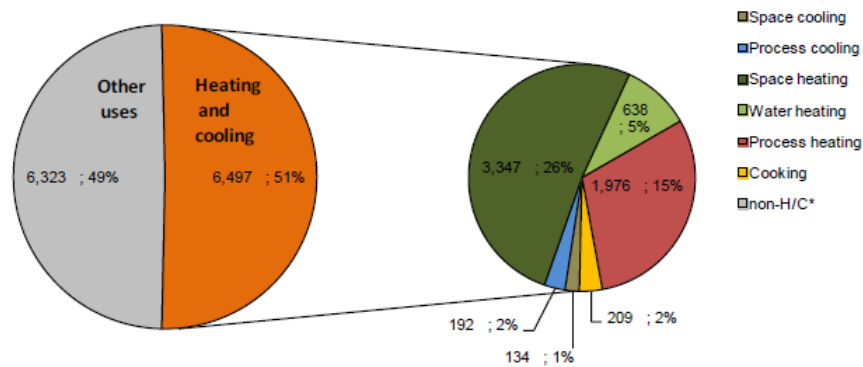


Figure 1.1. Fuel mix (left) and carbon emissions (right) - ET scenario [2]

1.2 Heating and cooling end-uses impact and the role of the building

Heating and cooling in buildings and industry is the biggest energy end-use sector in EU, accounting about 51% of the total final energy demand [3], as shown in Fig. 1.2. Still, more than 50% of the total energy demand of a modern building is caused by air conditioning processes [7].

In 2012, space heating was the most relevant end-use with a share of 52% of the total final energy demand for H/C (3250 TWh), followed by process heating which made up for 30% (2000 TWh) [3]. The main aim and for sure the starting point of any strategy to reduce the energy demand and reach COP21 goals should be to make heating and cooling more efficient and sustainable [4].



* Non-H/C comprises end-uses like transportation, mechanical energy in industry as well as residential and service sector appliances

Figure 1.2. Final energy demand for EU28 by end-use for H/C in all sectors in 2012 [TWh] [3]

The prospective given by the BM Energy Outlook 2018 about sector contributions to energy demand growth exhibits a slowdown on the rate of growth of both the industrial sector, benefiting from measures for improving energy efficiency, and the transport one, thanks to improvements in vehicle efficiency [2].

The building sector, on the contrary, will continue to grow: a combination of growing population and increasing prosperity, allowing people to live and work in greater comfort, leads to an increase in demand for space heating/cooling, lighting and electrical appliances [2].

Focusing on the European context, the allocation of end-uses to the residential, industry and tertiary sectors is shown in Fig. 1.3. Accordingly, the residential sector is the one which impacts the most on the heating/cooling demand and it is dominated by space heating with a share of 78%.

This allows to state that improving both efficiency in heating/cooling systems and thermal characteristics of building envelope but also integrating thermal energy storage systems will lead to a decrease in H/C energy needs.

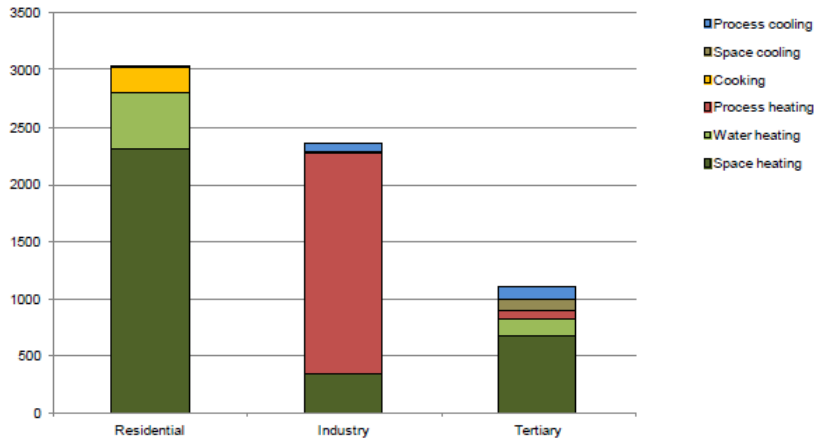


Figure 1.3. Final energy demand for EU28 for H/C by end-use and sector [TWh] in 2012 [3]

1.3 Potential for thermal energy storage systems

In the previously described present international energy context, thermal energy storage systems are able to play a pivotal role to deal with some important issues.

The most relevant abilities of a TES system are:

- decoupling production from consumption of energy [1];
- improving energy system efficiency, by storing waste heat coming from industrial processes or by supporting the implementation and management of renewable heat sources such as geothermal and solar energy in district heating and cooling networks;
- dealing with the intermittency of renewable energy sources:

- solar energy is a clear example of the huge mismatch between the energy need and the availability of the source at a daily or seasonal (see Fig. 1.4) scale: TES systems can enhance the fraction of energy utilization and make solar energy products more practical and attractive [5];
- the integration of wind power and electricity from photovoltaics into the electricity distribution system increases fluctuations concerns [6]: TES systems can both ensure security of supply, diversifying the options to supply heat and power in times of high demand, and lower the peak demand, reducing the need for peak power installations, which operate occasionally, therefore leading to high energy costs [1, 6];
- reducing the carbon footprint of heating/cooling and transport sectors using variable, flexible and base load renewable energy technologies, such as wind, solar thermal and PV, biomass and geothermal based ones and assisting in the heat management of energy systems for hybrid and electric vehicles and transport systems [1, 6].

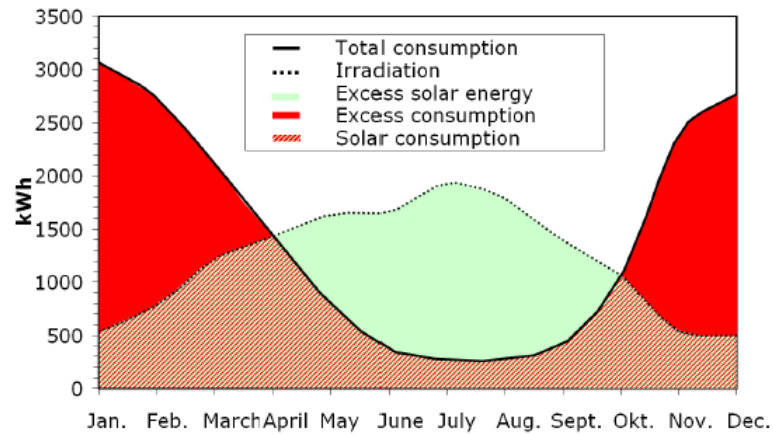


Figure 1.4. Seasonal shift between solar irradiation and heat demand (University of Technology Eindhoven, 2012)

Chapter 2

Thermal energy storage: the state of the art

This chapter has the aim to show the state of the art of sensible, latent and thermochemical heat storage technologies, by specifying for each one the storage working principle, the most common storage materials used and also giving an example of practical application in an existing prototype. Then, the last section is dedicated to motivate our interest in investigating on MOFs for TES, among the whole scenario of adsorbent materials.

2.1 General introduction

In recent years, thermal energy storage has become a very important topic in many engineering applications but also the subject of a great deal of research activity [7].

Thermal energy storage (TES) is a technology that allows to stock thermal energy by heating or cooling a storage material and use it hours, days (short term) or months (long term) later for heating and cooling applications and power generation [1].

TES systems can be classified according to:

- storage principle: sensible, latent or thermochemical (which can be based on sorption or chemical reaction without sorption);
- time length of stored thermal energy: short (daily) term or long (months/seasonal) term.

For all the energy storage methods mentioned, their performance is strongly dependent on the nature of the storage material chosen in the system.

Different parameters play an important role both in improving the performance of the heat storage system and in the investigation of its viability, therefore they should be taken into account during the design of such systems.

These are:

- the *environmental impact* and *safety conditions*, since they should be recyclable, non-poisonous and have a low CO₂ footprint;
- the *temperature range* at which they can store/release heat, related to the specific application;

- the *cost*, which has to be low, considering that, especially for building applications, to invest in a TES system is often not the primary concern for the owner;
- the *thermal stability*, since it must not deteriorate at the operating temperature range;
- the *energy storage density* and the *specific power*, which should be high because they express respectively the amount of energy that can be stored and released and the rate at which the storage process happens.

These last parameters are two important figures of merit in the design of an energy storage system to obtain a compact and efficient one.

Energy storage capacity, ρ_{Q-m} , and *energy storage density*, ρ_{Q-v} , are defined as the amount of energy stored in a given system or region of space per unit mass and per unit volume, respectively. They can be calculated per unit of mass/volume of the storage material or the prototype.

They are defined as follows:

$$\rho_{Q-m} = \frac{\text{heat storage capacity output}}{\text{mass of storage material or prototype}} \quad \left[\frac{Wh}{kg} \right] \quad (2.1)$$

$$\rho_{Q-v} = \frac{\text{heat storage capacity output}}{\text{volume of storage material or prototype}} \quad \left[\frac{kWh}{m^3} \right] \quad (2.2)$$

Specific power is defined as the energy rate, i.e. the power, delivered by a region of space per unit of mass of the material or prototype. It provides the information on the velocity at which the charging/discharging process happens.

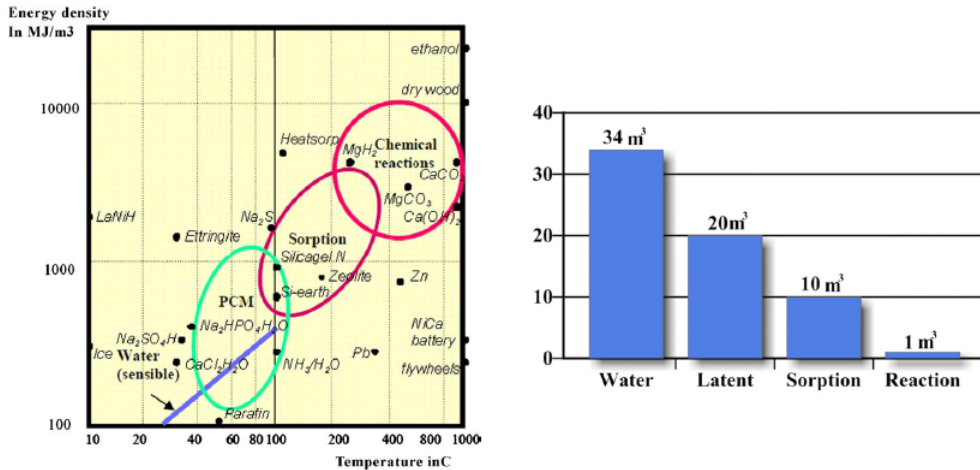


Figure 2.1. Energy density of high energy storage methods (left); Volume required to store 1850 kWh (With consideration of 25% heat losses, based on a 70 °C temperature increase for water) (right) [5, 11].

According to Fig. 2.1(a), the energy density increases going from sensible to thermochemical technologies. Fig. 2.1(b) shows how the value of this parameter impacts on the compactness of a TES system and, in particular, how the higher the energy density, the lower the volume of storage medium needed.

2.2 Sensible heat storage

2.2.1 Working principle

Sensible heat storage systems are able to store heat in the specific heat capacity (c_p) of the material chosen. During the heat energy absorption process, there is no phase change happening and materials experience a raise in temperature.

The thermal energy stored by sensible heat can be expressed as,

$$Q = m \cdot c_p \cdot \Delta T \quad (2.3)$$

where m is the mass (kg), c_p is the specific heat capacity ($\text{kJ} \cdot \text{kg}^{-1} \cdot \text{K}^{-1}$) and ΔT is the raise in temperature during charging process.

The amount of heat stored is proportional to the density, volume, specific heat and variation of temperature of the storage material [8].

2.2.2 Materials

Sensible heat storage materials have been widely investigated.

The most relevant characteristics that a material for sensible TES should meet are resumed in Table 2.1.

Properties	Desirable characteristics
Thermo-physical	High energy density, high thermal conductivity, high specific heat capacity, high density, long term thermal cycling stability
Chemical	Long term chemical stability, non-toxic, non-explosive, low corrosion
Economic	Cheap and abundant materials with low cost of manufacturing
Environmental	Low manufacturing energy requirement and CO ₂ footprint

Table 2.1. Desirable properties of sensible heat storage materials

These materials can be divided in two main groups: liquid and solid storage media. Liquids are most often water and thermal oil, and solids are rocks, bricks, concrete, iron, dry and wet earth, and many others.

Water has high specific heat ($4.184 \text{ kJ kg}^{-1} \cdot \text{K}^{-1}$), easy availability, cheap cost and it is non-toxic, non-flammable so it is completely harmless to people. Ice is used in cold

storage, liquid phase for low temperature heat energy storage, below 100 °C, and steam phase for high temperature heat energy storage.

Thermal oils are organic fluids, which have an operating temperature range between 12 °C and 400 °C, that means higher ΔT and more heat stored, but their specific heat capacity is lower than water ($2 \text{ kJ kg}^{-1} \cdot \text{K}^{-1}$). They have low viscosity and good flow properties, but mediocre heat transfer characteristics. They are expensive and they degrade at elevated temperatures, above their operating range, due to reactions like oxidation by air, which may cause corrosion of containers and pipes. Thermal oil vapor is a fire hazard risk when mixed with atmospheric air [8].

Molten salts can handle higher operating temperatures, up to 565 °C [8], which means higher ΔT and more heat stored. They are cheap, easily available, non-toxic and non-flammable. The main disadvantage is the high melting point (above 200 °C), which may cause their freezing in pipelines so that eutectic mixtures are widely used to bring down the melting point, while still maintaining a very high boiling point. Moreover they have high viscosity and mediocre heat transfer properties.

Liquid metals are characterized by a wide gap between their melting and boiling points, which gives a broad operational temperature range ΔT and a large sensible heat storage capacity [8]. Their heat transfer properties are outstanding but they are expensive and may be corrosive.

Earth materials like rocks, sand, gravel are used as fillers in single tank thermocline thermal heat storage systems, where they are arranged in a packed bed structure inside a container [8]. They are cheap, easily available, non-toxic, non-flammable and act as both heat transfer surface and storage medium for operating temperatures up to 350 °C.

Concrete blocks, composed by a mixture of cement, gravel and sand, are characterized by low cost, easy construction, good mechanical properties, non-toxicity and non-flammability. They were found suitable for TES up to 550 °C.

2.2.3 Sensible TES case study

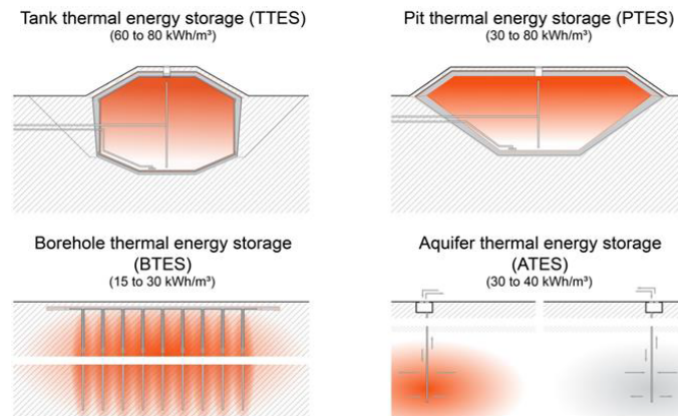


Figure 2.2. Main concepts for seasonal thermal energy storage [9].

Water is the most widely used storage medium for sensible TES with temperatures lower than 100 °C, for example solar-based warm water and space heating applications. That is

because of its availability, low cost, and, most important, its relatively high specific heat. On the other side, its low energy density leads to large storage volumes, specially in the case of seasonal thermal storage. It is therefore more advantageous to have large scale TES systems and moreover underground ones (UTES, Underground Thermal Energy Storage). The different storage techniques, as shown in Fig. 2.2, are:

- tank thermal energy storage (TTES);
- pit thermal energy storage (PTES);
- borehole thermal energy storage (BTES);
- aquifer thermal energy storage (ATES).

Here, a case study is reported as an outstanding example of sensible TES coupled with several other sustainable energy technologies. It is the case of the Drake Landing Solar Community (DLSC), located in Okotoks, Alberta, Canada, in which 52 low-rise detached homes are supplied with space heating and hot water [10].

Its energy system is illustrated in Fig. 2.3.

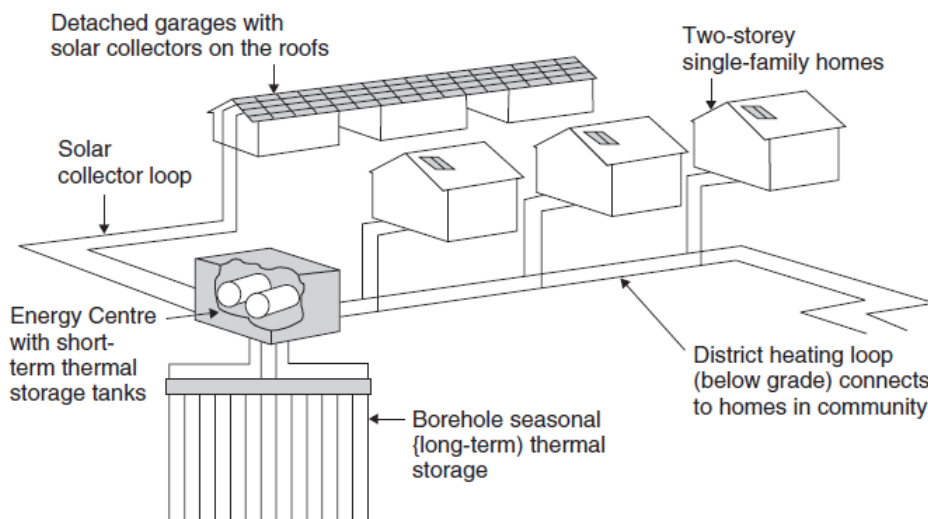


Figure 2.3. Simplified schematic of the principal energy components in the DLSC (Courtesy of DLSC) [10].

It is composed by:

- 800 single-glazed flat-plate solar thermal collectors, covering nearly 2300 m² (glycol as heat transport fluid), generating 1.5 MW of thermal power on a typical summer day;
- two 125,000 L steel tanks containing a volume of 240 m³ of water, which act as short-term storages;
- a district heating network connecting the DLSC homes;

- a borehole thermal energy storage (BTES), having 144 boreholes 35 m deep and linked in 24 parallel circuits, each with 6 boreholes in series, acts as seasonal storage;
- additional auxiliary systems, including a natural gas-fired hot water boiler for peaking requirements during winter and a separate cooling system for the solar collector loop;
- a separate solar domestic hot water system, using rooftop solar panels, and natural gas-based hot water units act as backups when solar energy is not available.

In a heat exchanger, the glycol solution from the solar collector loop transfers thermal energy to the water contained in the short-term TES, which is able to receive and discharge heat at a much greater rate than the BTES storage, which has a much higher thermal storage capacity.

For that reason, it acts as a buffer:

- during periods of high insulation, heated water from the solar collector loop is temporarily stored in the short-term TES tanks and subsequently transferred to the BTES at night;
- during winter peak heating demands, when heat cannot be discharged from the BTES sufficiently quickly, heated water is taken from the short-term TES, which is continually fed by the long-term TES.

Through the district heating network, heated water at 80 °C is transferred directly to the DLSC homes. At each home, it passes through an air handler, warming air that is then distributed throughout the house via ducting. The network capacity is 4.5 MW and the annual heat demand per house is 50 GJ.

For the homes in DLSC, thanks to this solar energy system integrated with TES, 90% of heating and 60% of hot water needs are designed to be met using solar energy. Annually, each home uses approximately 110.8 GJ less energy and emits about 5.65 t fewer GHGs than a conventional Canadian home. Thus, the DLSC avoids about 260 t of GHG emissions annually [10].

2.3 Latent heat storage

2.3.1 Working principle

Latent heat storage systems working principle is to store heat in the storage medium latent heat L , absorbing or releasing it when the material undergoes a phase change from one physical state to another. It could be a constant temperature process, if the material is a pure substance, otherwise it deals with a specific temperature range in the case of mixtures.

The thermal energy stored by latent heat can be expressed as,

$$Q = m \cdot L \tag{2.4}$$

where m is the mass (kg), L is the specific latent heat ($kJ \cdot kg^{-1}$).

The higher the latent heat, the greater the energy density of the TES.

Solid-gas and liquid-gas phase changes have the highest latent heat values, but the enormous change in the volume of the storage materials leads to more stringent containment requirements so they are not used. Solid–liquid phase change materials (PCMs) are widely used because they can store and release a relatively large quantity of heat within a narrow temperature range, without a large volume change [7].

2.3.2 Materials

The most important features that a solid-liquid PCM should possess, apart from the general criteria mentioned in section 2.1 and valid for all the storage materials, are a melting point fitted to the application, a high phase change enthalpy near the operating temperature and a high thermal conductivity in both liquid and solid phase [7]. All the desired characteristics are resumed in Table 2.2.

Properties	Desirable characteristics
Thermo-physical	Desirable melting point, high heat of fusion, high thermal conductivity, high density, small volume change during phase transition, little or no subcooling during freezing
Chemical	Long term chemical stability, non-toxic, non-explosive mixture, low corrosion potential
Economic	Cheap and abundant materials
Environmental	Low manufacturing energy requirement and CO ₂ footprint

Table 2.2. Desirable properties of latent heat storage materials

PCMs can be classified into three major categories: inorganic, organic and eutectic PCMs. Fig. 2.4 shows a further categorisation, which will be explained in the following paragraphs.

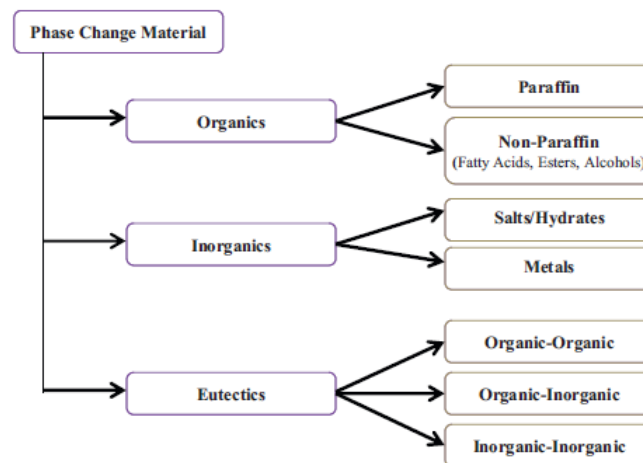


Figure 2.4. Classification of phase change materials [7].

Organic PCMs are divided into: paraffins, which are mixtures of alkanes, and non-paraffin organic materials, which include fatty acids, some alcohols, and esters.

Paraffins, with the chemical formula C_nH_{2n+2} , have a melting temperature in the range $6 \div 80$ °C, increasing with the number of alkane chains present within the molecules [7]. Their average heat of fusion is 170 MJ/m^3 , almost half the value of that of salts hydrates. Their low thermal conductivity λ [0.2 W/(mK)] and the significant volume change occurring during their phase change are their major drawbacks.

Non-paraffin organic PCMs, among which fatty acids are the ones of major interest, have a melting temperature in the range $10 \div 70$ °C, a heat of fusion that ranges from 128 to 183 MJ/m^3 , a low thermal conductivity and a varying level of toxicity. Their main drawbacks are that they are highly flammable and expensive.

Inorganic PCMs are constituted of salt hydrates and metals.

Salt hydrates can be considered as alloys of inorganic salts (AB) and water (H_2O), with a general formula $AB \cdot xH_2O$. Their phase change transition consists in the dehydration or hydration of the salt. The main advantages are a high volumetric storage density (350 MJ/m^3), a relatively high thermal conductivity (0.5 W/(mK)), compared to organic PCMs and a low cost [7]. The main problem is the decrease of their energy storage density with cycling, due to incongruent melting, which is an irreversible process that causes the segregation of a minor anhydrous salt. Subcooling before crystallization is another serious problem, which happens when the velocity of nucleation during the solidification phase is too low.

Metals are mostly fusible alloys of bismuth with other metals such as lead, tin, indium and cadmium. They have high volumetric fusion heat and high thermal conductivity [7] but their scarce availability and their high cost make them less used.

Eutectics are alloys of inorganics (mostly hydrated salts) and/or organics, having a single melting temperature, which is lower than that of any of the constitutive compounds, in the range $14 \div 80$ °C [7]. Their phase transition happens without phase segregation and they have a heat of fusion that ranges from 95 to 200 kJ/kg .

2.3.3 Latent TES case study

As mentioned above, two of the most important services delivered by TES systems are the shift of electrical consumption to off-peak periods to avoid demand charges associated to on-peak hours and the reduction of the peak period electrical demand. That could be beneficial for buildings and industrial processes, often having peak loads much greater than the average load.

A PCM-based cold thermal energy storage (CTES) case study is here reported, as a successful example in achieving those aims, briefly describing its composition and pointing out the technical, financial and environmental advantages.

It is the case of Harp Brewery in Dundalk, Ireland, an Irish brewery home, producing 1000000 hl of lager per year and consuming 12 GWh of electricity, 4 GWh of them for the refrigerant plant [10].

On the existing system, consisting in two circuits, a high-temperature circuit at -8 °C and a low-temperature circuit at -12 °C, it was decided to install a Cristopia TES system (STL). The STL (le *stockage latent* in French, or latent heat storage) is composed of a cylindrical black steel tank filled with spherical nodules. The nodules contain the PCM,

as shown in Fig. 2.5.

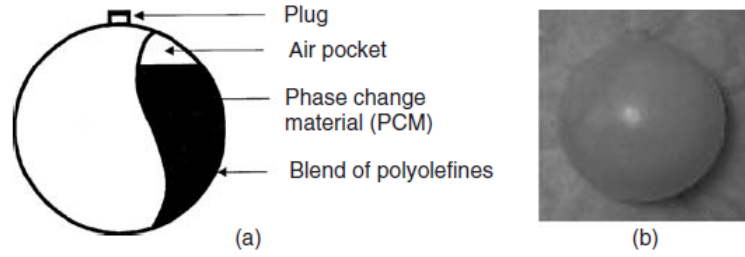


Figure 2.5. (a) The nodule for STL system (Courtesy of Cristopia Energy Systems), and (b) a capsule for the new STL latent TES (Courtesy of Mitsubishi Chemical Co.) [10].

The technical data and consumption of Harp Brewery are listed in Table 2.3. The STL-N10-200 TES system is able to store 10000 kWh at $-10\text{ }^{\circ}\text{C}$ during the night-time off-peak tariff period and it also reduces daytime chiller power by 1000 kW_{el}. As a consequence, a smaller chiller capacity is needed, the refrigeration efficiency is improved and a backup system is at disposal. In economic terms, the TES generates savings on demand charges, on maintenance costs and also due to the reduced electrical supply.

TECHNICAL DATA

Daily energy consumption [kWh]	44000
Maximum cooling demand [kW]	4000
Cooling energy stored [kWh]	10000
Storage temperature [$^{\circ}\text{C}$]	-10.4
Cooling energy stored [kWh]	10000
Store type	STL-N10-200
Number of tanks	2
Volume of tank [m^3]	100
Energy density (of prototype) [MJ/m^3]	180

Table 2.3. Harp Brewery energy system technical data [10]

From an environmental point of view, a smaller chiller capacity leads to reduced refrigerant charge, which is beneficial for avoiding ozone depletion, while the reduced electrical supply allows to cut back on greenhouse gases emissions, like CO₂, SO₂, and N₂O.

2.4 Thermochemical or sorption heat storage

The expressions “chemical”, “thermochemical”, “thermochemical sorption”, “compact” and “sorption” have all been used in different contexts by many authors regarding thermal energy storage [5]. In this thesis, “thermochemical” and “sorption” have been used

as synonyms to define, in contrast to sensible and latent *direct* heat storage methods, an *indirect* method operating in two ways: chemical reactions and sorption processes. In the former, energy is stored as the heat of reaction of reversible reactions. The latter stores thermal energy either through adsorption (physical bonding) or absorption (uptake/dissolution of a material) [1].

2.4.1 Terminology

Sorption heat storage is based on sorption, which can be defined as a phenomenon of capture of a gas or a vapour, called *sorbate*, by a substance in condensed state (solid or liquid), called *sorbent*.

It includes both absorption and adsorption:

- *absorption* is the phenomenon in which the molecules of the adsorbate penetrate the surface layer and enter the structure of the bulk solid/liquid, causing the change of the composition of one or both bulk phases [5], but considering storage applications, this term is usually relating to the absorption of a gas by a liquid (absorbent);
- *adsorption*, which is a phenomenon of binding of a gas on a surface of a solid or porous material [11], could be:
 - physical adsorption (*physisorption*), if the forces involved are non-bonded interactions, i.e. Van der Waals and electrostatic forces;
 - chemical adsorption (*chemisorption*), if the forces of valence bonding are involved, i.e. of the same kind as those operating in the formation of chemical compounds.

2.4.2 Classifications and working principle

According to the classification suggested by Yu et al.[5], sorption thermal storage can be distributed into four categories, as shown in Fig. 2.6:

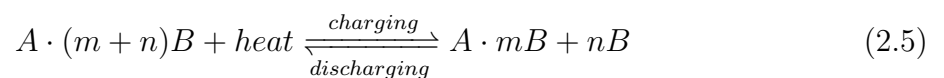
LIQUID ABSORPTION, in which the absorbent is liquid and the absorbate is gas;

SOLID ADSORPTION, in which the adsorbent is solid and the adsorbate is gas;

CHEMICAL REACTION, which consists in coordination reaction of ammoniate with ammonia and hydration reaction of salt hydrate with water;

COMPOSITE MATERIALS, which represent a combination of the previous processes.

All of these categories have in common the mechanism of sorption, which can be represented by the following equation:



where A is the sorbent, B is the sorbate and A/B is called a sorption working pair or sorption couple.

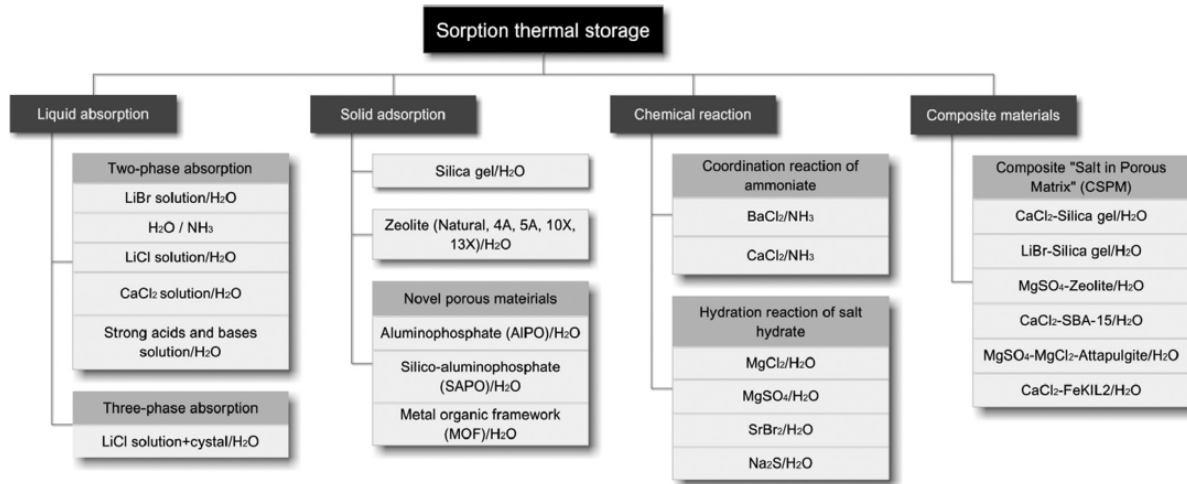


Figure 2.6. Sorption thermal storage classification [5].

Translating equation 2.5 into the different categories:

- for a liquid absorption process, $A \cdot (m + n)B$ represents a solution with a lower concentration of A than $A \cdot mB$;
- for a solid adsorption process, $A \cdot (m + n)B$ is the enrichment of B on the surface of A, as $(m + n)$ mole B is adsorbed;
- for a chemical reaction process, $A \cdot (m + n)B$ and $A \cdot mB$ signify a compound of one mole A with $(m + n)$ mole B and m mole B, respectively.

The charging process, called *desorption*, is an endothermic process, i.e. requires to supply heat to break the binding force and remove the sorbate B from the sorbent A, which can be stored separately.

The discharging process, called *adsorption*, is an exothermic process, i.e. releases heat when the sorbate and the sorbent get in touch, regardless of the time span between the desorption and the adsorption process.

Unlike direct heat storage, in an indirect method heat and entropy are released to the environment instead of being stored in the storage vessel. Energy is stored in terms of chemical potential, transferred to thermal energy during the discharging process. This feature makes sorption thermal storage a promising solution for long-term energy storage applications, because it is possible to decouple the sorption and desorption processes in time, for example storing solar energy in summer to meet with heating demand in winter, without significant heat losses.

Another classification of sorption thermal energy storage is made according to the system configuration:

CLOSED SYSTEMS In closed systems, materials are isolated from the environment and the entropy is exchanged with the environment via a heat exchanger. As shown in Fig. 2.7, the system is composed by two vessels: a reactor where the sorbent

is located and a condenser/evaporator where liquid water is collected. The vessels are connected by a conduct as a passage for vapor and, by means of a valve, the operation mode is switched from charging to discharging.

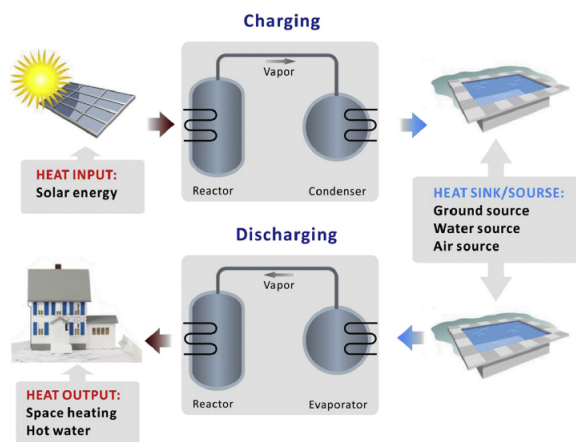


Figure 2.7. Operation principle of closed sorption thermal storage system [5].

In the adsorption (discharging) phase:

- a working fluid is evaporated, taking its evaporation heat, from the surroundings (low temperature level) and thereby producing useful cold in cooling applications;
- then vapour is adsorbed by the sorbent material, generating adsorption heat (medium temperature level), which is larger than the latent heat of vaporization: this heat is released to the environment in the cooling case or produces useful heat in heating applications.

In the storage phase:

- the dry adsorbent is separated from the liquid working fluid (the connecting valve is closed). As long as these components stay separate, long-term heat storage without losses is possible (sensible heat loss can be neglected).

In the desorption (charging) phase:

- the sorbent material is regenerated by supplying heat (high temperature level), from various external heat sources (solar thermal energy, industrial waste heat, local cogeneration of heat and power, district heating);
- the desorbed fluid condenses, releasing the heat of condensation (medium temperature level): this is useful heat in heating applications, while it is released to the environment in cooling applications.

The main issue is to choose the heat source for the discharging process:

- air source is suitable for areas with warm climate in winter otherwise it would be too cold to provide evaporation; moreover, it is great for its availability and freedom from location restrictions;
- ground source is warmer and more stable, but construction of heat exchangers is time-consuming and costly;
- water is a good option but only if the storage system is near to waters or swimming pools (not below 0 °C, better ammonia or methanol in cold areas).

Moreover, expected energy density of closed systems is reduced as compared to open storage one, since the working fluid (water vapor) is part of the storage system as it has to be stored as well.

In contrast to open systems, the main advantages are the possibility to recover energy from the condensation of water vapor during the charging phase. In this manner, the energy storage density can be enhanced. On the contrary, for the open adsorption TES, the heat of condensation is dumped to the environment and not recovered [12].

OPEN SYSTEMS Open systems operate at atmospheric pressure, i.e. the reactor is connected with the environment to allow the release and sorption of the sorbate. Thus, only water can be used as working fluid and air as carrier gas in those systems. As shown in Fig. 2.8, during the charging process, the reactor containing the sorbent encounters a cross airflow, previously heated by an heat source, like solar energy, becoming a dry hot air stream. It carries away the sorbate by desorption, regenerating the sorbent and thus getting wetter and cooler. During the storage phase, the storage material is not supplied by air so that no transfer of water vapor from or to the material is possible. During the discharging process, a humid, cool air stream (that may be exhaust air from the ventilation system) goes into the previously desorbed reactor. Here, water vapor in the air is adsorbed by the sorbent. The released heat of sorption makes the air become hotter and this hot air can be used for heating purposes, such as for heating the fresh air of the ventilation system [5].

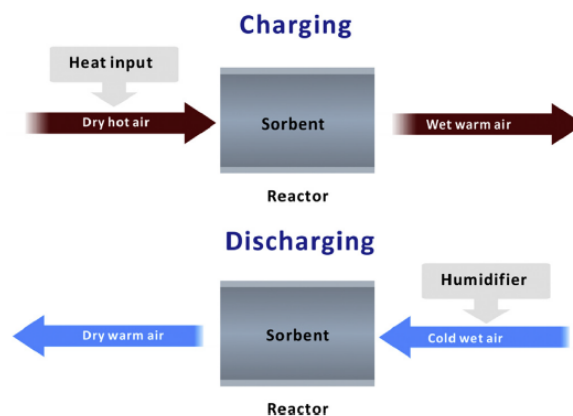


Figure 2.8. Operation principle of open sorption thermal storage system [5].

The main issues are to ensure that the ambient moisture is sufficiently high for a good discharging rate, otherwise an additional humidifier is needed, and to limit the pressure loss when blowing humid air through the reaction system, in order to keep the electricity demand for the blower on a low level [5].

At the same time, the lower cost of investment, due to the absence of condensers, evaporators, water storage reservoirs and maintenance of system pressure and the better heat and mass transfer conditions, make the open systems become an attractive solution for thermal energy storage, compared to the closed ones.

2.4.3 Materials

The most important features that a material for sorption TES, also known as TCM (Thermochemical storage material), should possess are:

- high energy storage capacity and density (Wh/kg and kWh/m³, respectively);
- water sorption behavior suitable for the operating conditions;
- low charging temperature;
- high uptake of sorbate ($g_{\text{sorbate}}/g_{\text{sorbent}}$), also called *working capacity*;
- appropriate heat and mass transfer properties, i.e. fast kinetics of reaction to ensure designed output power;
- hydrothermal stability (stability over large numbers of cycles);
- thermal stability, i.e. no deterioration upon operating temperatures;
- excellent reversibility, with no undesired by-products;
- easy to handle, non poisonous;
- low cost per kWh of heat stored.

In fact, no currently available material could satisfy all listed requirements [5]. For example, it is desirable a material having a high enthalpy of reaction, which leads to a high energy density but it is often true that these materials also need a high temperature source to be charged. Since the energy storage density is determined by both charging conditions (charging temperature and pressure) and discharging conditions (discharging temperature and pressure), a good compromise between the highest possible enthalpy of reaction and the lowest possible charging temperature should be found to optimize the energy density.

A part from this, TCMs exhibit the highest energy storage densities, in a range 200-500 kWh/m³, thus providing more compact energy storage systems compared to latent and sensible TES (see Fig. 2.1). Moreover, thermochemical energy storage allows to neglect heat losses between the storage and the recovery period because the energy is stored as chemical potential, thus making possible their use for long term storage applications.

Working pairs for liquid absorption

In thermal energy storage systems based on absorption, the higher the amount of refrigerant available for absorption, the greater the amount of sorption heat that can be recovered. To reach this goal, the largest difference between the solution concentration limits should be reached:

- the minimum concentration (the diluted solution concentration) should be as low as possible and it is fixed by the desired absorption temperature and evaporator temperature;
- the maximum concentration (the concentrated solution concentration) is limited by the absorbent solubility (saturation concentration) at the storage tank temperature.

The storage density of the absorbent aqueous solution, in the following paragraphs, is relative to the diluted solution.

1) LiBr/H₂O

LiBr/H₂O single effect absorption machines are suitable for solar cooling applications due to good performance at the temperatures available from conventional collectors.

Simulations made by N'Tsoukpoe et al.[20], based on an evaporation temperature of 5-10 °C to produce heat at 25-33 °C in winter, showed long-term storage densities between 180 and 310 kWh/m³.

A solar powered absorption refrigeration system with an energy storage function, using LiBr solution, proposed by Xu et al., achieved a storage density of 102.36 kWh/m³.

2) H₂O/NH₃

In the field of absorption thermal storage, efforts dedicated to the H₂O/NH₃ working pair mainly focus on the function of shifting the electricity demand from peak hours to off-peak hours, using an internal vapor compression heat pump. However, the energy densities obtained from the calculations were somewhat low, ranging from 32.8 to 33.8 kWh/m³.

Working pairs for solid adsorption

Most common adsorption storage materials include silica gel and zeolites, but novel microporous materials, like aluminophosphates (AlPOs), silico-aluminophosphates (SAPOs) and metal-organic frameworks (MOFs) are being widely investigated in the recent years.

1) Silica gel/H₂O

Silica gel is the most widely used desiccant in the class of mesoporous silicates because of its low cost and low desorption temperature. It can be easily employed with heat sources at temperatures lower than 100 °C (e.g., flat-plate solar thermal collectors) [12]. The main drawback is the low hydrophilic characteristic, meaning that the water adsorption mainly occurs at too high relative pressures, which leads to a low water exchange within a typical cycle, especially for closed systems (for which the adsorption/desorption process occurs in the pressure range between 0.1 and 0.3 p/p₀). As shown from Table 2.4, it seems that using silica gel in closed sorption thermal storage systems is not sufficiently competitive for short-term applications, due to its low energy density, even lower than that of water.

Nevertheless, they still represent a possible option if employed for long-term heat storage applications.

2) Zeolite/H₂O

Zeolites are crystalline aluminosilicates, based on the tetrahedral networks of silicon and aluminum, SiO₄ and AlO₄. Among more than 180 types of zeolite framework known, types 4A, 5A, 10X, 13X and Y remain the dominant zeolites that have been developed for commercial use [5]. They are characterized by a high specific surface area (i.e., about 800 m²/g) and a microporous structure that make them more hydrophilic than silica gel. This high affinity with water is reflective of strong bonding, that leads, on one hand, to high adsorption capacities even at low partial pressures, but on the other hand, to higher desorption temperatures, above 150 °C or even 200 °C, which is the major drawback for solar energy storage.

Experimental tests in both closed and open systems revealed energy storage densities up to 160 kWh/m³.

Their crystalline structure leads to higher hydrothermal stability under multiple adsorption/desorption cycles, compared to the amorphous structure of silica gels [12].

3) Novel porous materials

Several new classes of adsorption materials have been recently proposed as promising candidates for sorption thermal energy storage. These are aluminophosphates (AlPOs), silico-aluminophosphates (SAPOs) and metal-organic frameworks (MOFs).

- **AlPOs and SAPOs**

Aluminophosphates (AlPOs) and silico-aluminophosphates (SAPOs) are also referred to as zeo-like materials, as their crystalline structure is somewhat similar to those of classical zeolites. Unlike the hydrophilic zeolites or the less hydrophilic silica gels, these materials show a partially hydrophobic behavior, that is reflected in an S-shaped adsorption isotherm. This means that they behave as hydrophobic materials at low relative pressures, but they show a high hydrophilic behavior, i.e. a high amount of water vapor exchange, in a quite narrow pressure range. This behavior is advantageous for the use in adsorption heat transformation applications, especially if the steep increase lies within the working window of the application. Since the overall energy storage capacity is highly dependent on the water vapor exchange, these materials can guarantee very high energy storage capacities.

Among these two classes, the most attractive materials are known as AlPO-18 and SAPO-34 [12]. In a measurement reported by Henninger et al.[13], the storage capacities of SAPO-34 and AlPO-18 were found to be 203 Wh/kg and 243 Wh/kg respectively, at a desorption temperature of about 90 °C.

- **MOFs**

Metal-organic frameworks (MOFs) are both microporous and mesoporous crystalline materials composed of metal ions (or metal clusters) and organic linkers. Their high specific surface area and their tunable pore size and chemical composition to obtain the ideal adsorption properties are the most attractive features.

Among those materials, the Titanium based MIL-125-NH₂ is identified as one of the highly interesting candidates, as it is stable even over several cycles and shows a high

storage density, up to 322 Wh/kg, obtained at a quite low charging temperature of 80 °C, an adsorption temperature of 30 °C and an adsorption pressure of 12.5 mbar, in line with the typical practical closed TES operation conditions [19]. The main drawback is their higher cost, compared with traditional adsorbents like silica gels and zeolites. However, MOFs will be deeply examined in Chapter 3.

Working pairs for chemical reaction

Chemical reaction with sorption or *chemisorption* differs from physical adsorption/absorption in the thermodynamic variance, which equals to one for the former whereas it equals to two for the latter. Indeed, systems involving chemisorption require only one state variable to be specified (e.g. pressure or temperature), while two state variables (temperature, pressure or degree of sorbate loading) are needed to describe completely a physical adsorption/absorption equilibrium.

The main chemical reactions involved are:

- coordination reaction of ammoniate with ammonia;
- hydration reaction of salt hydrate with water.

Instead of adsorption process, chemical reaction involves changing in molecules configuration: in particular, ammonia and water vapour are attracted by metal ions to form coordinate bonds.

1) Coordination reaction of ammoniate with ammonia

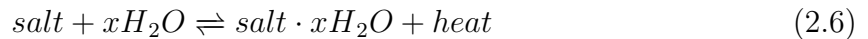
Metal halides are the most used ammoniates for the coordination reactions with ammonia, like NH_4Cl , NaBr , BaCl_2 , SrCl_2 and others. They cover a wide range of temperatures, from 48 °C (NH_4Cl) to 334 °C (NiI_2) [5].

They have been tested in existing sorption cooling plants, realizing cold storage capacity ranging from 95 to 125 Wh/kg.

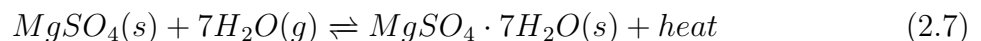
2) Hydration reaction of salt hydrate with water

For chemical heat storage reactions, hygroscopic salts such as calcium chloride (CaCl_2), magnesium chloride (MgCl_2), aluminum sulfate (Al_2SO_4), and magnesium sulfate (MgSO_4), show good potential and can lead to significant amounts of heat stored.

In these materials, thermal energy is stored by drying the salt hydrate and storing the dry salt and the water separately. The reversible reaction of hydration and dehydration of a salt hydrate is shown in Eq. 2.6,



which becomes Eq 2.7, for example, in the case of MgSO_4 :



As mentioned above, since chemical reactions are involved in the hydration/dehydration of inorganic salts, a large amount of heat is required to break covalent bonds, which leads to higher energy stored but some big concerns limit the application of those materials in

TES systems.

Equation 2.7, for example, represents the complete hydration/dehydration reaction, at which corresponds an energy density above 640 kWh/m³. That seems an outstanding result, outperforming all the previous mentioned sorption materials, but some observations must be considered.

Firstly, that energy density value is achieved only if all the seven H₂O molecules are taken up and released, phenomenon that happens at dehydration temperature of 275 °C, too much higher than the maximum temperature delivered by vacuum tube solar collectors, $T_{\text{max,dehyd}}=150$ °C [14]. Thus, a solar powered TES is able to cover the dehydration of at maximum 6 H₂O molecules, but still releasing the largest amount of heat, i.e. about 610 kWh/m³.

Secondly, the operation conditions (temperature and pressure) need to be taken into account. In fact, according to Van Essen et al.[14] experiments, MgSO₄ is not able to take up water at atmospheric pressure under the operating conditions of an open solar heat storage system. Instead, they concluded that MgSO₄ can be considered suitable for closed systems, operating under low-pressure conditions.

Thirdly, to avoid problems during storing and releasing of energy, it is necessary to know the melting and deliquescence points.

Melting is a problem, since it reduces the bed porosity of the material, and consequently the vapor transport through the bed, which limits the ability of the material to take up water again [14].

Deliquescence is defined as a first order phase transformation of the solid to a saturated solution, instead of a salt hydrate as product of the hydration, that happens when the relative humidity (RH) reaches a certain threshold value, namely, the deliquescence relative humidity (DRH) [5]. The forming of liquid film on the surface of salt crystal will not only prevent the hydration reaction from proceeding, but also cause corrosion problems due to the dripping of solution to other metal components.

Agglomeration phenomenon represents another issue, which occurs when the material is rehydrated (discharged), resulting in both low power output and low total energy output, badly affecting the cycling stability.

Composite materials

Though chemical reactions possess excellent storage potential, based on the analysis at the material level, their performance in actual systems requires further research.

Indeed, the high energy density results from large amount of enthalpy of reaction (compared to the weaker surface phenomenon of physisorption), due to stronger sorbate-sorbent interaction that leads to slow sorption kinetics. Moreover, due to deliquescence and agglomeration phenomena after several cycles, it is very difficult to keep the reaction. To avoid or at least reduce those phenomena, but at the same time to enhance the sorption ability under the typical working boundary conditions of adsorption TES, composite materials have been tested. They combine the higher energy densities of chemical reactions with the faster kinetics of physisorption.

Also known as Composites “Salt in Porous Matrix” (CSPM), they are based on inorganic salts (e.g., CaCl₂, LiCl, LiBr) dispersed in a host porous matrix (e.g. zeolites, silica gel, vermiculite, metal-organic frameworks). Typical examples are the well-known Selective Water Sorbents (SWSs), which are composite materials specifically developed for water adsorption. It is possible to change the chemical nature of the confined salt, its particle

size inside the matrix pores, the amount of the confined salt and the synthesis conditions, in order to nano-tailor the achievable adsorption properties of the synthesized material [15].

Figure 2.9 illustrates the working principle, showing that the reaction between salt and adsorbate is always confined inside the pores of the host matrix: this makes the adsorption/desorption more stable and less affected by the adsorbate diffusion phenomena [12].

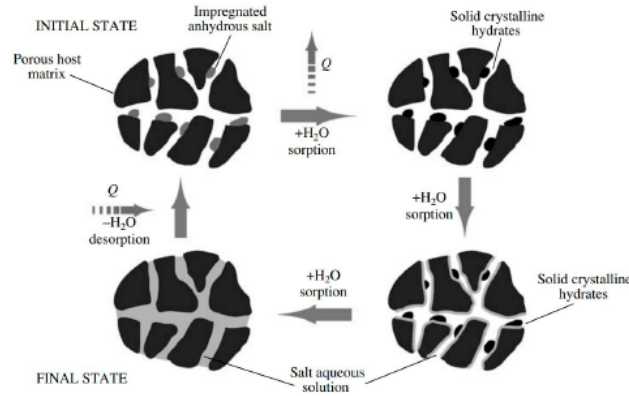


Figure 2.9. The working principle of a composite adsorbent [12], with permission from Springer Nature, 2007.

CSPMs have been tested for adsorptive heat transformation (AHT), demonstrating attractive performance in terms of heat storage density at typical operation conditions and in some cases showing also low regeneration temperatures.

Zeolite/MgSO₄(15 wt.%) composite (ZM15) was tested by Hongois et al. [16], obtaining an energy density of 166 kWh/m³ with an airflow rate RH of 50% and a desorption temperature of 150 °C from vacuum tube solar collectors in an open TES.

Jänchen et al. [17] found that 30 wt.% CaCl₂ impregnated in aluminosilicate shows a storage density of 172 kWh/m³ with a desorption temperature of 120 °C.

CaCl₂(30 wt.%) impregnated in silica gel showed the highest and most stable storage capacity of 283 Wh/kg at a quite low desorption temperature of 90 °C but one should also take into account the test operation conditions [18]. An adsorption temperature T_{ads} of 30 °C and an adsorption pressure p_{ads} of 33.9 mbar were set as test boundary conditions, but they correspond to a RH of 80 %, which is too high relative humidity with respect to the practical conditions of a TES.

MOFs composites were found to exhibit excellent performances. MIL-100(Fe) and MIL-101(Cr) impregnated by CaCl₂ solution, having a concentration of salt respectively of 46 wt.% and 62 wt.% [19], outperform all the above mentioned composites. Indeed, the lowest desorption temperature of 80 °C and a lower, and also in line with the practical operation conditions, RH of 30% (T_{ads} 30 °C and p_{ads} 12.5 mbar), lead to an energy density of 208 kWh/m³ for the former and 310 kWh/m³ for the latter composite, which are also higher than the silica gel/CaCl₂ composite tested in more favourable conditions.

2.4.4 Thermochemical ES case study

Among a lot of working pairs, some of them shown in Table 2.4 and many others illustrated in scientific papers, a Composite “Salt in Porous Matrix” has been chosen as thermochemical energy storage system case study.

It is the case of a seasonal TES based on the hydration/dehydration cycle of ZM15 composite, i.e. 15 wt.% MgSO_4 impregnated in a zeolite 13X host matrix. Microcalorimetry and macrocalorimetry tests were carried out at Institut National des Sciences Appliquées de Lyon (INSA LYON), in collaboration with Institut de Recherches sur la Catalyse et l’Environnement de Lyon (IRCE LYON).

Fig. 2.10 shows the storage system working principle. In the case of an open system that uses humid air contained into the ventilation exhaust air flow from the building, having almost a temperature of 20 °C and relative humidity of 50%, as a source of water vapor for the exothermic adsorption reaction. Indeed, the discharging mode provides useful heat, during in winter, to heat up incoming fresh air via a mechanical heat recovery heat exchanger, for heating applications in buildings. The charging phase of the adsorbent material occurs typically during summer, when hot air between 80 °C and 180 °C, coming from solar thermal collectors, is used to desorb water vapour from the material and regenerate it [16].

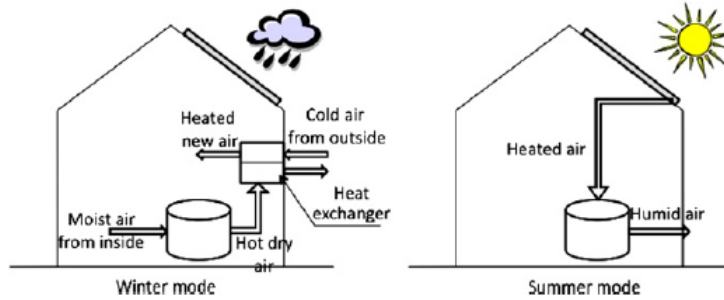


Figure 2.10. Thermal energy storage concept: discharging phase during winter (left) and charging phase during summer (right). [16].

Thermogravimetric analyses (TGA) were performed on a small sample of adsorbent: the dehydration test revealed that 80% of the initial water content of the hydrated zeolite– MgSO_4 material is lost at temperatures minor than 150 °C.

Microcalorimetry tests were carried out on a 100 mg of ZM15 sample using the Belsorp volumetric sorption analyzer and the adsorption isotherm of water vapor, shown in Fig 2.11, was obtained at 25 °C.

Macrocalorimetry tests on 200 g of composite sample, carried out in the macro-reactor described in Fig. 2.12, let a sensitivity analysis be performed on two main controlling parameters: the air mass flow and air relative humidity (at fixed temperature of 25 °C).

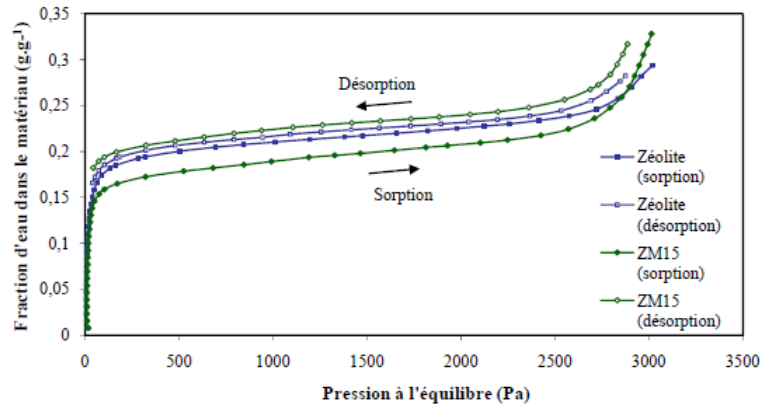


Figure 2.11. Isotherms of sorption and desorption at 25 °C of the zeolite and ZM15 - Belsorp Analyzer [33].

The energy density achieves the maximum value of 180 Wh/kg or 166 kWh/m³ with an airflow rate of 8 L/min and inlet air at 50% RH and a temperature of 25 °C [33]. Based on these results, the zeolite-based composite seems to be a promising thermal energy storage material suitable for long-term storage purposes, thanks to its good thermal properties and thermal and chemical reliability [33], even if it cannot be ranked among the lowest desorption temperature composites, as also shown in Table 2.4.

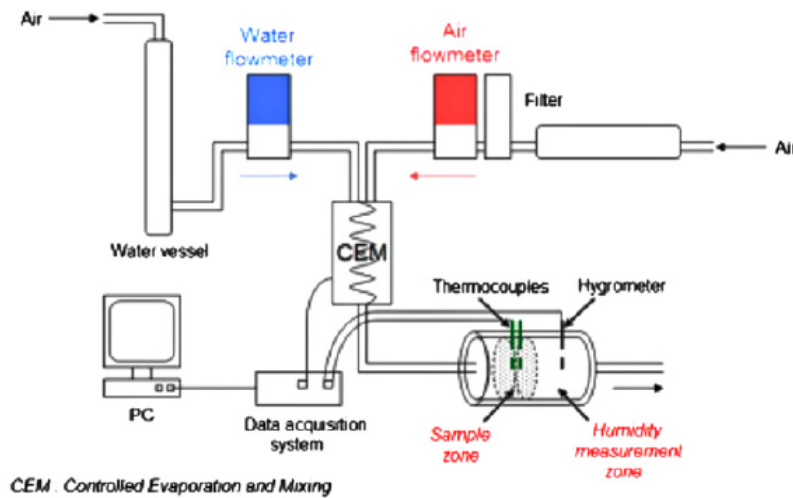


Figure 2.12. Experimental setup for hydration tests [16].

2.5 Why decide to study and test metal-organic frameworks?

The analysis of the state of the art of thermal energy storage, firstly, let us conclude that, due to the reduced sensible heat losses and to the storage mechanisms involved, sorption

(or thermochemical) heat storage systems represent the ones able to store the largest amount of energy in the lowest volume, i.e. showing the highest energy density. Thus, it is worth trying to screen all adsorbent material categories, in order to find the most promising one.

Since energy storage density and desorption temperature represent two important figures of merit in TES systems design, it is reasonable to perform a first screening taking into account these values. According to the results obtained from experimental tests on different adsorbent materials, Fig. 2.13 and literature data details shown in Table 2.4 allow to compare energy storage capacity values as a function of desorption temperature.

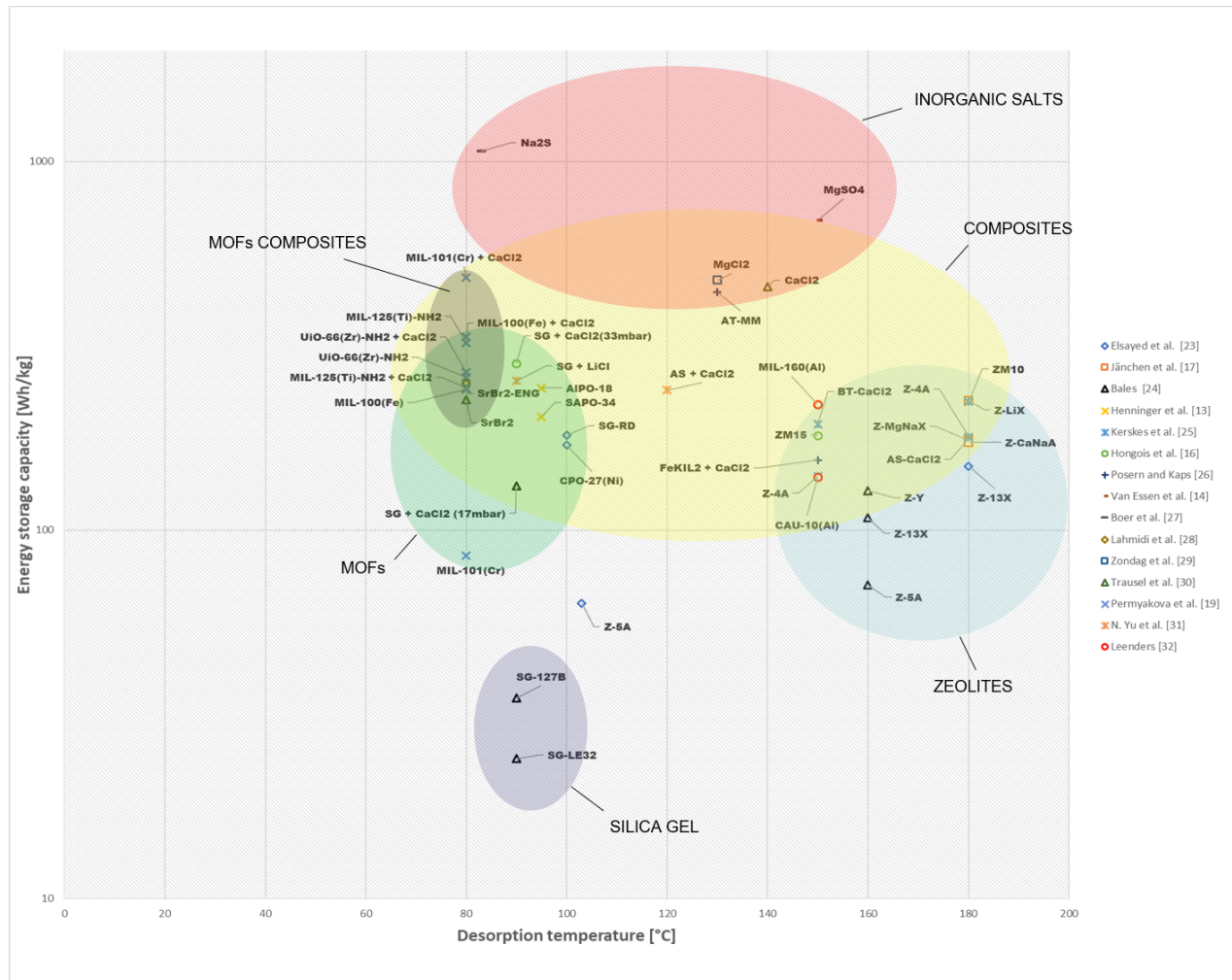


Figure 2.13. Energy storage capacity of sorption materials as a function of desorption temperature. Graph adjusted from Fig. 8 [5].

It can be easily noticed that MOFs represent the adsorbent materials category that exhibits the highest energy storage capacity at the lowest desorption temperature of 80 °C, in particular:

1. MIL-101(Cr) + (62%)CaCl₂ with 485 Wh/kg, among MOF-based composites;

2. MIL-125(Ti)-NH₂ with 322 Wh/kg, among pristine MOFs.

It is noteworthy that inorganic salts show the highest energy densities and in the case of sodium sulfide Na₂S, the value (1067 Wh/kg) reported by Boer et al. [27] has been found at 83 °C desorption temperature but we must not forget all issues of deliquescence and agglomeration phenomena, which deeply influence the long term performance of these materials.

REFERENCE	LABEL	DESCRIPTION	DISCHARGING PRESSURE [mbar]	DESORPTION TEMPERATURE [°C]	ENERGY DENSITY [Wh/kg]	SYSTEM TYPOL.
Elsayed et al.[23]	Z-13X	Zeolite type 13X	23.1	180	149	closed
Elsayed et al.[23]	Z-5A	Zeolite type NaCa 5A	23.1	103	63	closed
Elsayed et al.[23]	SG-RD	Microporous silica gel	23.1	100	181	closed
Elsayed et al.[23]	CPO-27(Ni)	MOF Nickel based	23.1	100	170	closed
Jänchen et al.[17]	AS-CaCl ₂	Aluminosilicate+30wt.%CaCl ₂	-	180	177	closed
Jänchen et al.[17]	Z-MgNaX	Zeolite type MgNaX	-	180	175	closed
Jänchen et al.[17]	Z-LiX	Zeolite type LiX	-	180	225	closed
Jänchen et al.[17]	Z-CaNaA	Zeolite type CaNaA-60	-	180	173	closed
Bales[24]	Z-13X	Zeolite type 13X	-	160	108	closed
Bales[24]	Z-5A	Zeolite type NaCa 5A	-	160	71	closed
Bales[24]	Z-Y	Zeolite type Y	-	160	128	closed
Bales[24]	SG-127B	Microporous silica gel	-	90	35	closed
Bales[24]	SG-LE32	Macroporous silica gel	-	90	24	closed
Bales[24]	SG+CaCl ₂ (17mbar)	Mesoporous silica gel+33.7wt.%CaCl ₂	17	90	132	closed
Henninger et al.[13]	SAPO-34	Silico-aluminophosphate type 34	12	95	203	open
Henninger et al.[13]	AIPO-18	Aluminophosphate type 18	12	95	243	open
Kerskes et al.[25]	Z-4A	Zeolite type 4A	-	180	179	open
Kerskes et al.[25]	Z-4A	Zeolite type 4A	-	150	140	open
Kerskes et al.[25]	ZM10	Zeolite 4A+10wt.%MgSO ₄	-	180	223	open
Kerskes et al.[25]	BT-CaCl ₂	Bentonite+40wt.%CaCl ₂	-	150	194	open
Hongois et al.[16]	ZM15	Zeolite 13X+15wt.%MgSO ₄	15.9	150	180	open
Hongois et al.[16]	SG+CaCl ₂ (33mbar)	Mesoporous silica gel+CaCl ₂	33.9	90	283	open
Posern and Kaps[26]	AT-MM	Attapulgite+MgSO ₄ and MgCl ₂ (mass ratio 20/80)	31.8	130	442	open
Posern and Kaps[26]	FeKIL2+CaCl ₂	Iron silicate with CaCl ₂	12	150	155	open
Van Essen et al.[14]	MgSO ₄	-	21	150	694	open
Boer et al.[27]	Na ₂ S	-	-	83	1067	open
Lahmidi et al.[28]	SrBr ₂ -ENG	SrBr ₂ with expanded natural graphite	-	80	250	closed
Zondag et al.[29]	MgCl ₂	-	-	130	477	closed
Trausel et al.[30]	SrBr ₂	-	-	80	226	open
Trausel et al.[30]	CaCl ₂	-	-	140	458	open
Permyakova et al.[19]	MIL-100(Fe)	Iron based MOF	12.5	80	243	closed
Permyakova et al.[19]	MIL-101(Cr)	Chromium based MOF	12.5	80	86	closed
Permyakova et al.[19]	MIL-125(Ti)-NH ₂	Titanium based MOF	12.5	80	322	closed
Permyakova et al.[19]	UiO-66(Zr)-NH ₂	Zirconium based MOF	12.5	80	260	closed
Permyakova et al.[19]	MIL-100(Fe) + CaCl ₂	Iron based MOF + 46wt.%CaCl ₂	12.5	80	335	closed
Permyakova et al.[19]	MIL-101(Cr) + CaCl ₂	Chromium based MOF + 62wt.%CaCl ₂	12.5	80	485	closed
Permyakova et al.[19]	MIL-125(Ti)-NH ₂ + CaCl ₂	Titanium based MOF + 45wt.%CaCl ₂	12.5	80	243	closed
Permyakova et al.[19]	UiO-66(Zr)-NH ₂ + CaCl ₂	Zirconium based MOF + 43wt.%CaCl ₂	12.5	80	268	closed
N. Yu et al.[31]	SG + LiCl	Silica gel + 35wt.%LiCl	-	90	254	open
N. Yu et al.[31]	AS + CaCl ₂	Aluminosilicate + 30wt.%CaCl ₂	-	120	240	open
Leenders[32]	CAU-10(Al)	Aluminium based MOF	10	150	139	open
Leenders[32]	MIL-160(Al)	Aluminium based MOF	10	150	219	open
N'Tsoukpoe et al.[20]	LiBr(sol)/H ₂ O	-	12.5	60	310*	closed
Xu et al.[21, 22]	H ₂ O(sol)/NH ₃	-	-	-	35*	closed

Table 2.4. Details of literature data of different adsorption materials categories, also shown in Fig. 2.13 (*energy density expressed in kWh/m³, thus not plotted in Fig. 2.13).

Another comment arises from the comparison between MOF and MOF-based composites energy density and the one of other composites. Silica gel + CaCl₂ [16] shows 283 Wh/g energy capacity, which is comparable to MOFs ones and it is also related to quite low desorption temperature (90 °C). Now, if we look at adsorption temperature (30 °C) and pressure (33.9 mbar), which correspond to 80% relative humidity (instead of 30 % for MOFs), we can easily discover that more favourable conditions were applied to test silica composite.

Thus, this graph allows to consider that it is worth investigating in those new adsorbent materials, known as metal-organic frameworks, but it still does not allow to make a choice. Indeed, the last comment, underlining the importance of boundary conditions related to energy density values, enables us to move to the next chapter, in which a deepening on MOFs adsorption behavior and on the ideal characteristics that an adsorbent should meet, will be carry out.

Chapter 3

Metal-organic frameworks for thermal energy storage

In this chapter, section 3.1 is dedicated to a deepening on metal-organic framework materials has been carried out in order to show their state of the art and their potential as adsorbent material for sorption thermal storage. Then, in section 3.2, since this thesis is focused on the thermal characterization of water/MOF working pairs, selection criteria to choose the most promising MOFs or MOF-based composites for TES have been shown.

3.1 MOFs: the state of the art

Metal-organic frameworks (MOFs), also known as porous coordination polymers (PCPs), are porous crystalline materials in powder form organized by the coordination between metal ions or metal clusters and organic ligands.

As shown in Fig. 3.1, MOFs are made by linking organic and inorganic units via strong chemical bonds: the organic linkers (e.g. polycarboxylates, polyphosphonates, imidazolates, polypyrazolates, polytetrazolates), when linking to metal-containing units (i.e. Fe^{3+} , Cr^{3+} , Ti^{4+} , Zr^{4+} , Al^{3+} , Zn^{2+} , Co^{2+} , Cu^{2+} , Ni^{2+} , Mg^{2+}) can yield architecturally three-dimensional structures with well-defined pore size distributions [34].

Why did metal-organic frameworks catch the attention of researchers in the field of adsorption materials?

The most attractive features of MOFs are:

- high specific surface area, typically ranging from 600 to 10000 m^2/g , which often leads to higher water uptakes, compared to the classical sorbent materials;
- water uptakes up to 1.43 $\text{g}_{\text{water}}/\text{g}_{\text{ads}}$ (MIL-101(Cr) [43]), very often outperforming that of any inorganic porous material such as silica gel, zeolites, or SAPO/AIPO;
- faster kinetics: since adsorption processes are based on physisorption, mass and thermal transport are a lot faster than most chemisorption based materials, which means also lower desorption temperatures;
- hydrothermal stability, recently verified for a large range of them;

- tunable adsorption behaviour: among more than 20000 MOF structures currently known, their quite diverse adsorption properties, in terms of water uptake capacity, pressure at which pore filling occurs, and shape of the adsorption isotherms, are programmable by changing the metal ion and/or the organic linker, but also with direct or postsynthetic modifications, i.e. adding functionalised linkers that bear various hydrophilic ($-\text{NH}_2$) or hydrophobic ($-\text{NO}_2$) groups.

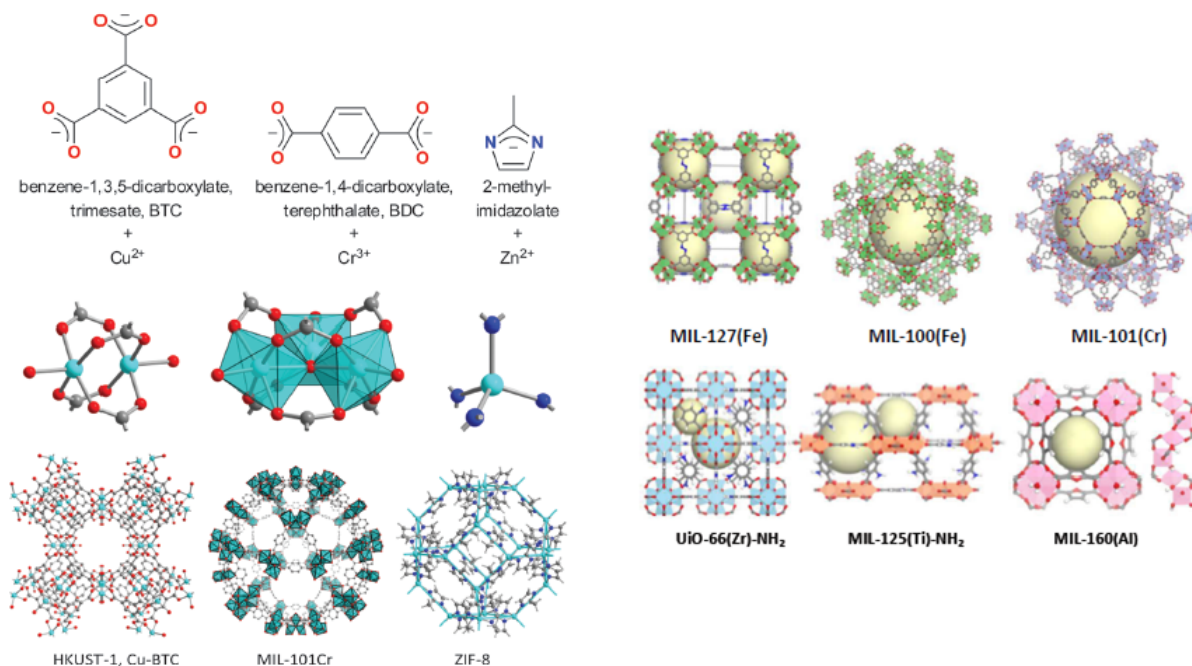


Figure 3.1. Prototypical linkers with selected metal nodes and secondary building units in corresponding MOFs (with acronyms) [19, 35].

In particular, the latter feature allows to obtain the ideal adsorption properties, the most suitable to the specific application. This is the reason why this new class of porous materials is being investigated for numerous potential applications, such as for gas storage and separation processes, drug delivery, heterogeneous catalysis, and, recently, water sorption for heat transformation and storage, which was first suggested by Aristov [36]. In particular, series of MILs (MIL stands for Materials from Institut Lavoisier) or UiO's (UiO stands for Materials from University of Oslo) that are made by three- and four-valent metal cations (Cr^{3+} , Al^{3+} , Fe^{3+} , Zr^{4+} and Ti^{4+}) and aromatic polycarboxylate linkers were considered for water sorption applications.

3.1.1 MOF/ H_2O working pair: adsorption thermodynamics

Since the prevalent adsorption mechanism is physisorption, the following section is dedicated to thermodynamic concepts describing it.

The physical adsorption, *physisorption*, is a phenomenon of binding of a gas or a vapour on the surface of a porous material, in which the forces involved are non-bonded interactions, and in particular Van der Waals forces.

Unlike chemisorption, the physical adsorption equilibrium is said to be *divariant*, (i.e. thermodynamic variance equal to two), which means that it requires two state variables to be fully described. Thus, it has three degrees of freedom: temperature, pressure and working capacity (or water uptake). According to these variables, it is possible to study the adsorption equilibrium in three ways:

- *isobaric* conditions, obtaining the working capacity as a function of the temperature;
- *isothermal* conditions, obtaining the working capacity as a function of the pressure;
- *isosteric* conditions, obtaining the pressure as a function of the temperature.

Physisorption mechanisms

In this context, one should differentiate the physisorption mechanisms that happen, according to the pore size of the material.

Indeed, adsorption materials can be divided, according to their pore size ϕ , into:

- *microporous* materials, if their pore width does not exceed about 2 nm,

$$\phi < 2 \text{ nm } (20 \text{ \AA})$$

- *mesoporous* materials, if their pore width falls between 2 nm and 50 nm,

$$2 \leq \phi \leq 50 \text{ nm}$$

- *macroporous* materials, if their pore width exceeds 50 nm.

$$\phi > 50 \text{ nm } (500 \text{ \AA})$$

The adsorption process that occurs in microporous material is called *micropore filling*. It can be regarded as a reversible and continuous volumetric phenomenon of pore filling, starting from the smallest and more energetic pores, followed by a nucleation-growth process, in which the interaction adsorbate-adsorbate becomes significant rather than the adsorbate-adsorbent one.

Instead, physisorption in mesopores takes place in three distinct stages: *monolayer adsorption*, *multilayer adsorption* and *capillary condensation*. In monolayer adsorption, all the adsorbed molecules are in contact with the surface of the adsorbent. Then, as the pressure increases, multilayer adsorption takes place, i.e. overlapped layers of molecules are formed so that not all the adsorbed molecules are in direct contact with the adsorbent surface. A further pressure increase causes capillary condensation, which is the phenomenon whereby a gas condenses to a liquid-like phase in a pore, at a pressure p less than the saturation pressure p_0 of the bulk liquid. If mesopores exceed a certain critical width, capillary condensation is accompanied by hysteresis, i.e. the adsorption and desorption curves do not coincide.

Working capacity and cycling loading lift

An *isosteric* transformation is a thermodynamic process that happens at constant *working capacity* x , i.e. the mass of adsorbed water at fixed conditions of temperature and pressure per unit of anhydrous adsorbent mass:

$$x = \frac{m_{\text{adsorbed}}}{m_{\text{sorbent}}} \quad \left[\frac{g_{\text{adsorbed}}}{g_{\text{sorbent}}} \right] \quad (3.1)$$

The equilibrium of the adsorption process is reached when the water uptake becomes constant, i.e. when the same amount of sorbate molecules is adsorbed and desorbed, thus adsorption isosteres are very important to be obtained.

Different is the definition of the *cycling loading lift* x_{cycl} , i.e. the working fluid exchange between the adsorption and desorption steps of the entire cycle at fixed conditions of temperature and pressure (conditions for the adsorption step on the one hand and conditions for the desorption step on the other hand):

$$x_{\text{cycl}} = \frac{m_{\text{exchanged}}}{m_{\text{sorbent}}} \quad \left[\frac{g_{\text{exchanged}}}{g_{\text{sorbent}}} \right] \quad (3.2)$$

If the sorbate is water, working capacity and cycling loading lift can be also expressed in $\left[\frac{\text{cm}^3}{g_{\text{sorbent}}} \right]$.

Isosteric heat of adsorption

Since adsorption is a spontaneous process, it is characterized by a negative Gibbs free energy variation, ΔG_{ads} . Indeed, the transition of the sorbate from the gas to the condensate state leads to an entropy loss. Thus, it follows that adsorption must always be an exothermic process, i.e. $\Delta H < 0$, since:

$$\begin{aligned} \Delta G_{\text{ads}} &= \Delta H - T\Delta S < 0 \\ \Delta H &= H_{\text{a}} - H_{\text{g}} \end{aligned} \quad (3.3)$$

where the subscripts “a” and “g” are referred to the adsorbed (condensate) and gaseous phases, respectively.

The mass transfer will proceed in the direction of lower free energy until the equilibrium is reached, i.e. the chemical potential of the gas phase and the adsorbed phase are equal. Thus:

$$\begin{aligned} \Delta G_{\text{ads}} &= 0 \\ \mu_{\text{a}} &= \mu_{\text{g}} \end{aligned} \quad (3.4)$$

but also,

$$\Delta H = T\Delta S \quad (3.5)$$

Starting from the total derivative of both sides of equation 3.4 and combining with Gibbs-Duhem relation, Clausius-Clapeyron relation 3.6 is obtained:

$$\begin{aligned} -s_{\text{a}}dT + v_{\text{a}}dP &= -s_{\text{g}}dT + v_{\text{g}}dP \\ \frac{dP}{dT} &= \frac{(s_{\text{g}} - s_{\text{a}})}{(v_{\text{g}} - v_{\text{a}})} \end{aligned} \quad (3.6)$$

where s and v are the specific molar entropy and specific molar volume of the substance, respectively.

Two approximations allow to simplify the relation:

1. below the critical temperature, the specific volume of the condensate phase, v_a , is considered negligible, being three orders of magnitude lower than the one of the vapour phase in the case of water:

$$v_g - v_a \approx v_g \quad (3.7)$$

2. the ideal gas behaviour of the vapour is assumed:

$$v_g = \frac{R \cdot T}{P} \quad (3.8)$$

From the combination of equations 3.6 and 3.7, we obtain the change in entropy upon adsorption:

$$\Delta S(n_a) = -\left(\frac{dP}{dT}\right)_{n_a} v_g \quad (3.9)$$

At equilibrium, combining equations 3.8, 3.9 and 3.5, it is obtained the change in enthalpy upon adsorption:

$$\Delta H(n_a) = -\frac{R \cdot T^2}{P} \left(\frac{dP}{dT}\right)_{n_a} \quad (3.10)$$

Equation 3.10 is often rearranged in the van't Hoff form:

$$\Delta H(n_a) = R \left(\frac{d \ln P}{d\left(\frac{1}{T}\right)}\right)_{n_a} \quad (3.11)$$

The isosteric heat of adsorption, q_{st} is given a positive value:

$$q_{st} = -\Delta H(n_a) = -R \left(\frac{d \ln P}{d\left(\frac{1}{T}\right)}\right)_{n_a} > 0 \quad \left[\frac{kJ}{mol}\right] \quad (3.12)$$

It is an indicator of the strength of the interaction between an adsorbate and a solid adsorbent and, divided by the universal gas constant, R [kJ/(mol K)], it represents the isosteric curve slope on a Clapeyron diagram, having $\left(-\frac{1}{T}\right)$ on the x-axis and $(\ln P)$ on the y-axis.

Adsorption isotherms classification

The isosteric field, i.e. the set of isostere curves specific of a working pair, is generated starting from the concept of adsorption isotherm.

An adsorption isotherm is a curve that describes the relation, at constant temperature, between the amount adsorbed, i.e. the working capacity x , and the equilibrium pressure of the gas. The uptakes are often plotted as a function of the relative pressure p/p_0 , where p is the equilibrium pressure and p_0 corresponds to the saturation vapour pressure of the adsorbate at the adsorption temperature, since this allows an easier comparison of

adsorption isotherms recorded at slightly different temperatures.

According to Brunauer (Brunauer et al., 1938, Brunauer et al., 1940) classification, then better specified by the International Union of Pure Applied Chemistry (IUPAC, 1985), six categories of adsorption isotherms can be found, as shown in Fig. 3.2:

- TYPE I isotherm is characterized by a steep water uptake at very low pressure and a long saturation plateau; this is due to enhanced adsorbent-adsorbate interactions in narrow micropores; it is the typical behaviour of very hydrophilic microporous adsorbents, such as zeolites, CPO-27 (also known as MOF-74), whose limiting uptake is governed by the accessible micropore volume rather than by the internal surface area, i.e. the surface of all pore walls.
- TYPE II isotherm is given by the physisorption of most gases on non-porous or macroporous adsorbents; the shape is the result of unrestricted monolayer-multilayer adsorption up to high p/p_0 ; the knee represents the switch from monolayer to multilayer adsorption, while the thickness of the adsorbed multilayer generally appears to increase without limit when $p/p_0 = 1$;
- TYPE III isotherm is typical of hydrophobic materials, characterized by weak adsorption/adsorbate interactions, since very high pressure should be reached to release the adsorbed molecules clustered around the most favorable (strong) sites.
- TYPE IV isotherm is typical of mesoporous adsorbents (e.g. silica gel), whose behaviour is firstly determined by the adsorbent/adsorbate interactions in the same way as type-II, i.e. through monolayer-multilayer adsorption; then capillary condensation occurs; at the end, a saturation plateau of variable length. If mesopores exceed a certain critical width, capillary condensation is accompanied by hysteresis, i.e. the adsorption and desorption curves do not coincide.
- TYPE V isotherm, typical of water adsorption on both microporous (e.g. UiO-66, MIL-125) and mesoporous (e.g. MIL-100, MIL-101) adsorbents, is characterized by an hydrophobic behaviour at low p/p_0 , similarly to type-III, but at higher p/p_0 a steep water uptake occurs, in a narrow pressure range, up to saturation, giving the so-called “S” shape.
- TYPE VI isotherm is representative of layer-by-layer adsorption on a highly uniform non-porous surface. The step-height now represents the capacity for each adsorbed layer, while the sharpness of the step is dependent on the system and the temperature. Amongst the best examples of type-VI isotherms are those obtained with argon or krypton at low temperature on graphitised carbon blocks.

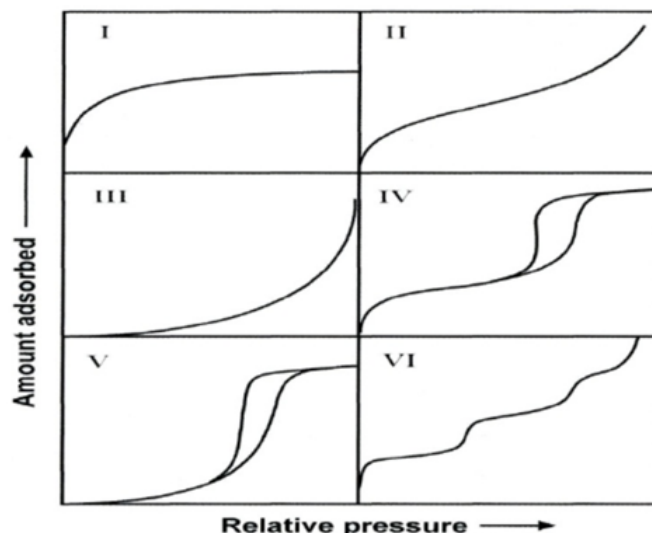


Figure 3.2. Adsorption isotherms - Brunauer classification

3.1.2 How to tune adsorption properties on MOFs

Tunable adsorption properties is the most attractive feature of MOFs. It can be performed:

- modifying the pore distribution by changing the chemical composition: this means changing the ligand and/or metal cluster at the stage of synthesis, thus obtaining microporous or mesoporous materials, which have, as mentioned above, different adsorption behaviours;
- adding amino-functionalized groups that enhance hydrophilic or hydrophobic behaviour, both through direct and post-synthetic modifications.

In the following paragraph, how and how much pore size, chemical composition and amino-functionalized modifications affect water adsorption properties will be shown, providing examples of MOFs on which these influences are significant.

Pore size and chemical composition influence

As already mentioned, pore size has a relevant impact on the adsorption mechanism that occurs and, of course, also on the adsorption isotherm shape.

Microporous materials, i.e. whose pores widths are lower than 2 nm, show a pore-filling adsorption mechanism, which is continuous and reversible, thus excluding the possibility to have hysteresis loops due to irreversible capillary condensation. Nevertheless, different chemical composition also results in adsorption isotherms changes.

Here we compare four different MOFs, which despite of being microporous, show diverse water uptakes and relative pressure of steep increase in adsorption: Ni-CPO-27, Mg-CPO-27, MIL-125 and UiO-66.

The crystal structure of CPO-27 resembles a honeycomb and can be obtained with Ni^{2+} , Mg^{2+} , Co^{2+} , Zn^{2+} as metal ions and 2,5-dihydroxyterephthalic acid as the organic linker

[37]. Taking nichel and magnesium based CPO-27 as examples, they both have a pore size of 1.2 nm and both adsorption isotherms exhibit a type-I profile, characterized by a large water uptake at low pressure and a long saturation plateau, as usually found for zeolites [37]. Despite that, the water uptake of Ni-CPO-27 and Mg-CPO-27 is of 0.47 and 0.68 cm³/g, respectively, due to the larger molar mass of the latter.

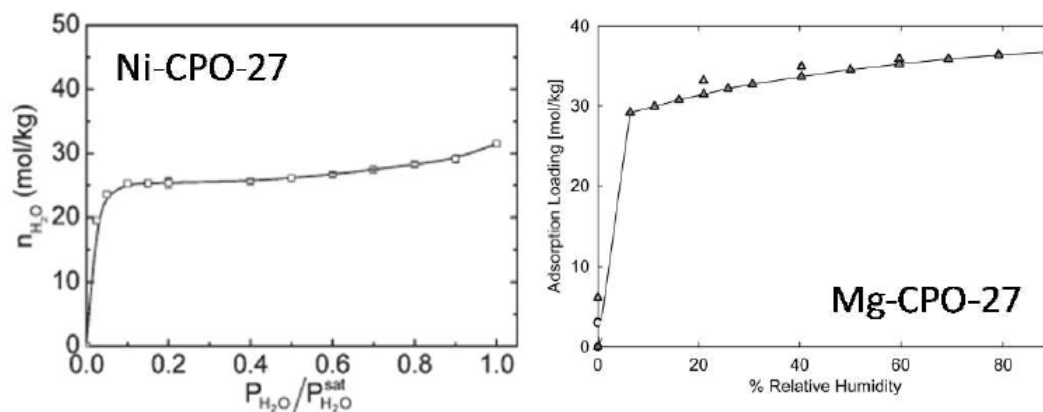


Figure 3.3. Water adsorption isotherms at 298 K on isoreticular CPO-27 solids: (left) Ni-CPO-27 and (right) Mg-CPO-27 [37].

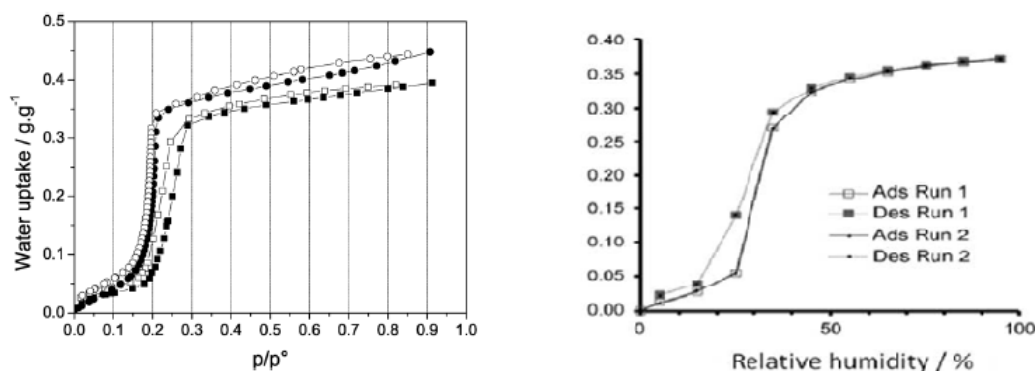


Figure 3.4. Water adsorption isotherms at 298 K of: (left) Ti-MIL-125 (square) and Ti-MIL-125-NH₂ (circle)[38] and (right) two consecutive water adsorption/desorption cycles for UiO-66 (regeneration at 353 K under an inert atmosphere) [37].

The inorganic cluster of UiO-66 solid is a Zr₆O₄(OH)₄ octahedron, forming lattices with 12-fold connection through a 1,4-benzenedicarboxylate organic linker [37]. It exhibits two types of cavity of diameter 0.75 nm and 1.1 nm.

MIL-125, keeping the same organic linker of UiO-66, has clusters made by different cations, i.e. TiO₅(OH), and exhibits two types of cage, whose accessible diameters are 0.6 nm and 1.2 nm [37].

Both UiO-66 and MIL-125 show the same water capacity of 0.36 cm³/g [38] and similar

adsorption isotherms, i.e. type-V “S” shaped. What differs is the relative pressure at which the steep increase in water uptake happens, which is at p/p_0 equal to 0.25 and 0.33 for MIL-125 and UiO-66, respectively [38]. As shown in Fig. 3.4, the desorption branches do not perfectly coincide with the adsorption branches, but for such small pore sizes, well below the critical diameter of 2.0 nm at 25 °C, irreversibility cannot be associated with capillary condensation and it has been tentatively assigned to minor modifications of the porous structure due to guest-host interactions and network flexibility [37].

Despite the same pore size, only changing the metal cluster, a different water uptake, pressure range at which pore filling occurs and also isotherm shape is detected, as shown in Fig. 3.3 and 3.4.

Mesoporous materials, on the contrary, having pores widths higher than 2 nm, exhibit a monolayer-multilayer adsorption mechanism, i.e. a step-wise process (in contrast, pore filling is continuous), often accompanied by irreversible capillary condensation that generates hysteresis loops between adsorption and desorption branches.

It is the case of MIL-100 and MIL-101. These materials are built from the assembly of trinuclear clusters of trivalent cations among Cr^{3+} , Fe^{3+} , Al^{3+} and terephthalate-based linkers for MIL-101 and trimesate for MIL-100. Two dimensions of pore are detected in their structure: 2.5 and 2.9 nm for MIL-100 and 2.9 and 3.4 nm for MIL-101 [37].

They have similar type-V adsorption isotherms, as shown in Fig. 3.5, but different water uptakes and pressures at which the steep increase in adsorption happens:

- the maximum water uptake is about $0.8 \text{ cm}^3/\text{g}$ for MIL-100 while $1.43 \text{ cm}^3/\text{g}$ for MIL-101 (reported by Henninger et al. [43]), thanks to the higher pore volume of the latter [37];
- the relative pressure is about 0.35 for MIL-100 and 0.46 for MIL-101, thus letting us consider MIL-100 more hydrophilic than MIL-101 [37].

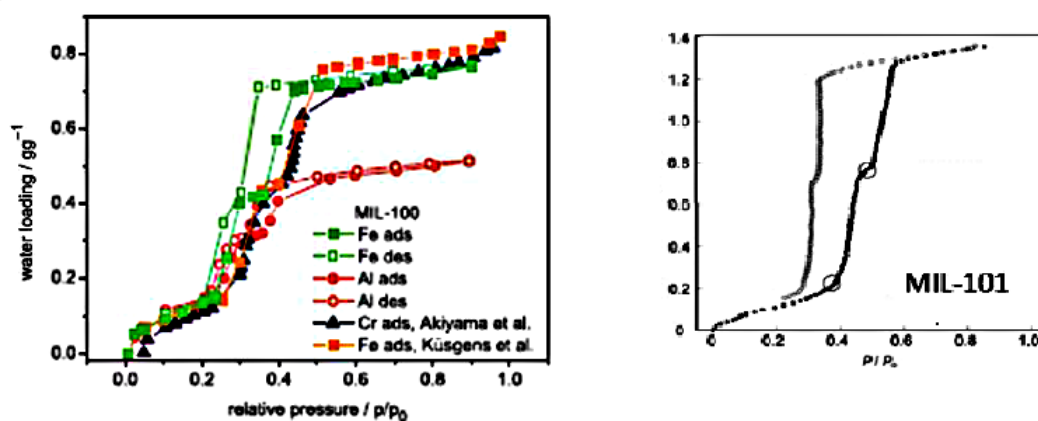


Figure 3.5. Water adsorption isotherms at 298 K of: (left) MIL-100 made from Fe^{3+} , Cr^{3+} or Al^{3+} and (right) Cr-MIL-101 [37].

As shown in Fig. 3.5, a two-step process is observed, both in MIL-100 and MIL-101, which is thought to arise from the filling of the smaller class of pores closely followed by that of the larger ones.

Amino-functionalized linkers influence

The adsorption properties of MOFs can be also tuned by modifying the surface properties of their porous framework. This can be achieved, both directly during synthesis and post-synthesis, adding functionalized groups (e.g. $-\text{NH}_2$, $-\text{NO}_2$, $-\text{OH}$, $-\text{OCH}_3$, $-\text{CH}_3$) able to enhance the hydrophilic or hydrophobic behaviour and sometimes also to enhance water uptakes.

In particular:

- $-\text{NH}_2$, $-\text{OH}$ are known to be hydrophilic groups since they shift adsorption to lower relative humidity;
- $-\text{NO}_2$, $-\text{OCH}_3$, $-\text{CH}_3$, instead, are known to be hydrophobic groups since they shift adsorption to higher relative humidity.

Here follow examples of MOFs surface decoration.

Figure 3.6 shows modified MIL-101 with two different groups: Cr-MIL-101- NH_2 and Cr-MIL-101- NO_2 . As we can see, the relative pressure at which corresponds the steep increase in water adsorption is 0.47, 0.45 and 0.35 for Cr-MIL-101, Cr-MIL-101- NO_2 and Cr-MIL-101- NH_2 , respectively [38]. This also leads to an higher water uptake of $0.9 \text{ cm}^3/\text{g}$ for the most hydrophilic Cr-MIL-101- NH_2 , compared to the one of pristine MIL-101 ($0.87 \text{ cm}^3/\text{g}$).

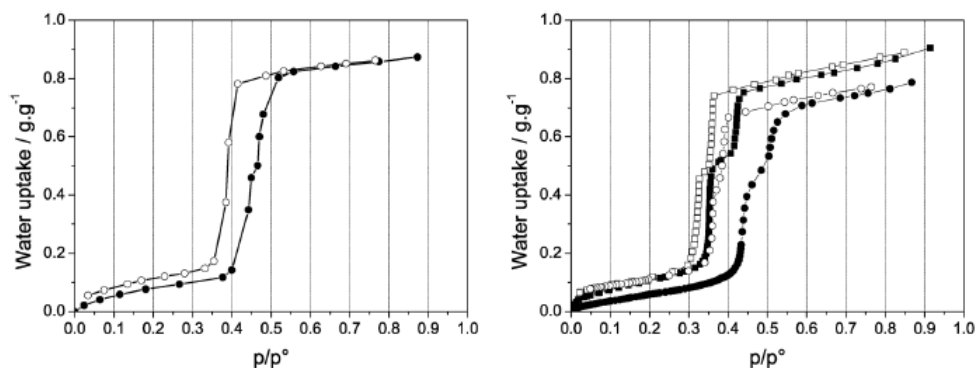


Figure 3.6. Water adsorption isotherms at 298 K of: (left) Cr-MIL-101 and (right) Cr-MIL-101- NH_2 (square) and Cr-MIL-101- NO_2 (circle). The full and empty symbols are the adsorption and desorption branches, respectively [38].

It is interesting to point out how functionalized modifications can impact on capillary condensation. Since desorption takes place at very similar pressures for all MIL-101, equal to 0.37, the hysteresis loops are wider for MIL-101 and MIL-101- NO_2 . This can be explained as follows: thanks to its higher hydrophilicity, Cr-MIL-101- NH_2 shows a water uptake that is twice that of Cr-MIL-101- NO_2 . As a result, the cavity that gets

filled upon capillary condensation is smaller for Cr-MIL-101-NH₂ than for MIL-101 and Cr-MIL-101-NH₂ [38].

Figure 3.7 shows both UiO-66 and MIL-125 modified with the hydrophilic amino-functionalized group -NH₂.

In the case of UiO-66, the amino and non-amino functionalized materials show the same water uptake of 0.36 cm³/g but different relative pressure of inflection point: 0.33 and 0.15 for UiO-66 and UiO-66-NH₂, respectively.

The same happens for MIL-125: the water uptake is about 0.36 cm³/g for both pristine MIL-125 and MIL-125-NH₂ but the relative pressure decreases from 0.25 to 0.2 for MIL-125-NH₂, due to its higher hydrophilicity.

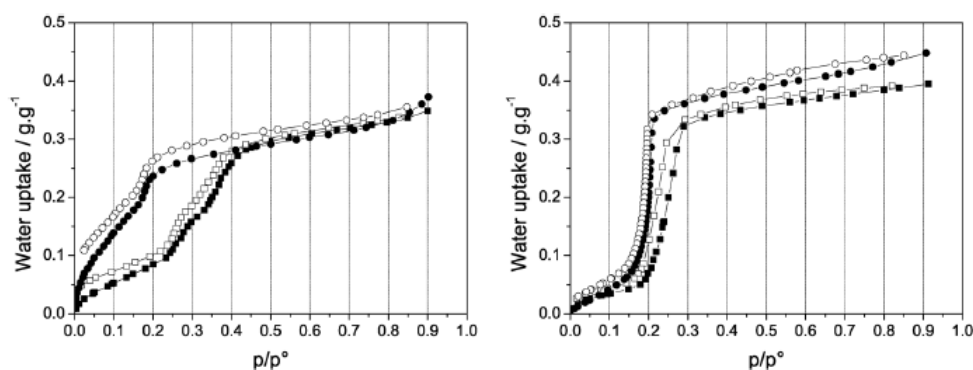


Figure 3.7. Water adsorption isotherms at 298 K of: (left) Zr-UiO-66 (square) and Zr-UiO-66-NH₂ (circle); (right) Ti-MIL-125 (square) and Ti-MIL-125-NH₂ (circle). The full and empty symbols correspond to the adsorption and desorption branches, respectively [38].

3.1.3 MOFs hydrothermal stability

Metal-organic frameworks exhibit, as mentioned above, high surface areas, pore volumes and regular porous structures with various chemical functionalities. However, a number of reports have shown that some of them can lose their structures quickly under humid conditions. Moreover, they may be subjected to cyclical thermal stresses, since esothermic/endothermic adsorption reactions cyclically take place.

Thus, it is very important to investigate their stability upon both cycling and high temperatures and the effect of exposure to humid vapours, such as water vapour, i.e. their hydrothermal stability.

Thermal stability has been assessed up to 200-300 °C, but considering MOFs low desorption temperatures (80-100 °C), this source of degradation can be excluded.

That is not the case for water vapour. Due to the electrophilic character of metal coordination centers and nucleophilic character of organic linkers, adsorbed water molecules may disorder the framework by two different degradation methods:

- by hydrolysis, i.e. the metal-ligand bond is broken and water dissociates to form a hydroxylated cation and a free protonated ligand;

- by ligand displacement, i.e. the insertion of a water molecule into the M-O metal-ligand bond of the framework, leading to the formation of a hydrated cation and to the release of a free ligand [37].

The stability of the framework upon water is generally attributed to the metal-ligand bond strength, which depends on the combined metal-ligand properties.

On one side, the coordination number of metal cation influence stability: MOFs containing metals of IV group in their highest oxidation state (e.g. Ti^{4+} , Zr^{4+}) tend to be more stable compared with metal clusters with +2 oxidation state. High coordination number of metal cluster, also from a kinetic point of view, plays an important role, due to crowding effect which prevents water clusters from forming near the metal center.

On the other side, ligand pK_a can be a useful indicator of the metal-ligand bond strength, since this interaction is based on Lewis acid-base coordination chemistry.

Moreover, the activation energy for the metal-ligand dissociation has a relevant impact. That depends not only on the kinetics of water exchange, in fact the higher the exchange rate, the higher the activation energy of hydrolysis, but also on the hydrophobicity of the framework and the electronic configuration. The latter, for example, explains the high stability of MIL-101(Cr): since chromium has electrons on d-orbital, the transition from octahedral (initial state of substitution reaction) to square pyramidal state (transition state of substitution reaction) can be more complicated and requires more activation energy.

The main effects of hydrothermal instability are the loss of surface area and/or the loss of crystallinity, but it can happen that crystallinity, specific surface surface and porous volume do not change even if a part of the solid is dissolved. Thus, cycling water adsorption isotherms is more appropriate for the evaluation of the stability under moisture exposure: if the desorption branch in such water adsorption isotherms crosses the adsorption branch, it can be concluded that the porous framework has collapsed totally or partially [37].

Here a variety of experimental tests are reported: all of them investigate MOFs stability through PXRD and porosimetry tests performed before and after water exposure.

Low and co-workers monitored by X-Ray Diffraction (PXRD) the stability of a series of ten MOFs having different organic linker, pore structure, metal node nature and coordination, after their exposure to steam for few hours. The result was the steam stability map, shown in Fig. 3.8, in which each position for a given MOF represents its maximum structural stability. Thus, it is possible to conclude, that MIL-110, MIL-101, CPO-27 (or MOF-74), ZIF-8, Al-MIL-53 and HKUST-1 are water vapore stable [37].

More recently, the stability of a series of MOFs was estimated after water adsorption measurement under 80% relative humidity at room temperature. Except for DMOF-1 and UMCM-1, any loss of crystallinity was exhibited for all the sample, whose stability was ranked according to the surface area loss: $\text{UiO-66-NH}_2 > \text{CPO-27}, \text{HKUST-1} \gg \text{DMOF-1}, \text{UMCM-1}$ [37].

UiO-66-NH_2 structural stability upon water vapour exposure has been confirmed by Walton et al. [40], by comparing PXRD patterns of the samples (see Fig. 3.9) before and after the adsorption measurements.

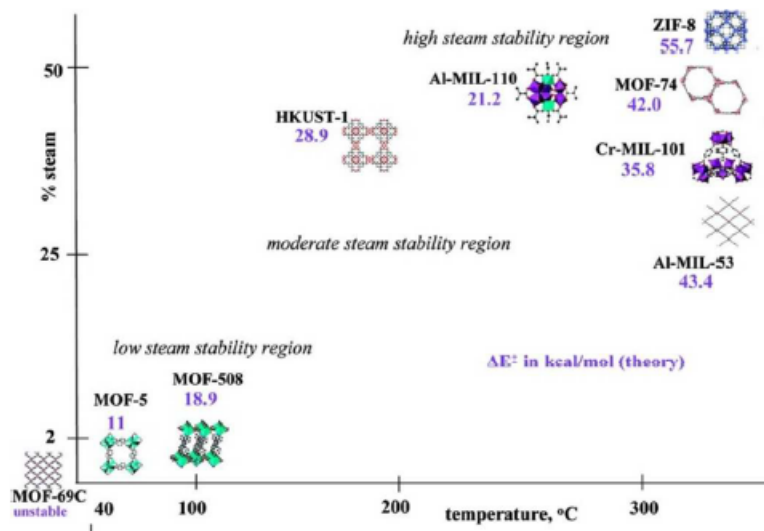


Figure 3.8. Steam stability map of MOFs [37].

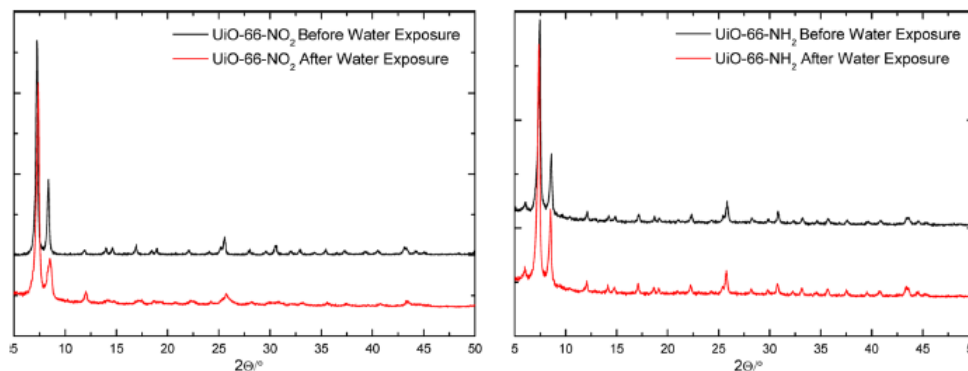


Figure 3.9. PXRD patterns before and after exposure to water vapor and subsequent reactivation [40].

Moreover, Permyakova and co-workers verified the stability of two composites, MIL-100(Fe)/CaCl₂ (46 wt%) and MIL-101(Cr)/CaCl₂ (62 wt%), by collecting SEM (Scanning Electron Microscopy), TGA and nitrogen sorption porosimetry measurements after ageing the samples for about 18 and 6 months, respectively. It was confirmed their cycling stability and no evidence of framework degradation was found [19].

Hydrothermal stability is also a synonym of water cycle stability or cyclability, i.e. the extent to which water uptake is cyclable with subsequent adsorption/desorption cycles by a material. It is essential to investigate on it, since the energy density of a material depends on the cyclable water uptake, also called cycling loading lift.

Permyakova performed continuous water adsorption and desorption cycles between 30 and 80 °C under 12.5 mbar (representative conditions of seasonal energy storage) on MIL-100(Fe)/CaCl₂ (46 wt%) and MIL-101(Cr)/CaCl₂ (62 wt%), as shown in Fig. 3.10.

The former shows a decrease of about 11% of its initial water uptake after 11 adsorption–desorption cycles, but reaches a steady state after 7 cycles. This results in a slight

decrease of its energy storage capacity from 335 to 298 Wh/kg.

The latter presents only 8% loss under 10 adsorption–desorption cycles and reaches a steady state after 4 cycles, resulting in a reduction of its initial energy storage capacity from 485 to 446 Wh/kg.

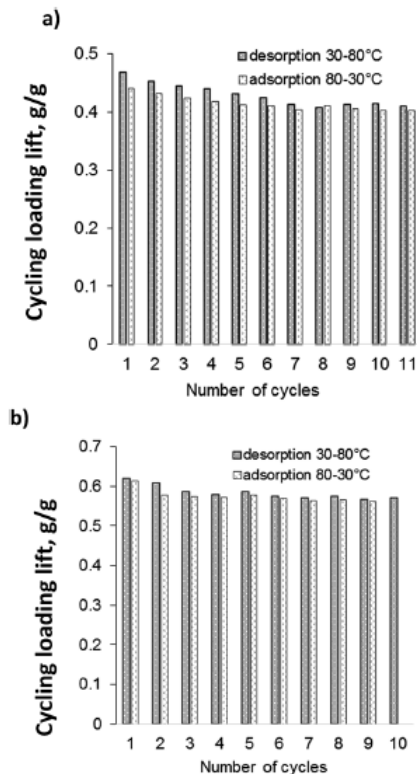


Figure 3.10. Stability under numerous adsorption–desorption cycles ($p \frac{1}{4}$ 12.5 mbar) of (a) MIL-100(Fe)/CaCl₂ (46 wt%) and (b) MIL-101(Cr)/CaCl₂ (62 wt%) [19].

Khutia et al. [41] investigated hydrothermal stability of Cr-MIL-101-NH₂ and Cr-MIL-101-NO₂, by exposing to forty continuous water adsorption and desorption cycles between 40 and 140 °C under a water vapor pressure of 5.2 kPa. They showed an exchanged water mass loss very low, about 16 and 18 % respectively. They have also carried out powder X-ray diffraction (PXRD) as well as BET surface and pore measurements by nitrogen adsorption of those compounds after 40 water sorption cycles, without finding any significant change in crystallinity of the materials.

Jeremias et al. [42] performed multi-cycle ad-/desorption experiments on UiO-66-NH₂ and MIL-125-NH₂ in the same conditions as Khutia et al., but interposing a 20 h thermodynamic analysis cycle before the cycling experiment, after 20 and 40 cycles each, letting the equilibrium be reached with slower kinetics. It was found a decrease in water mass exchanged of about 13 % and less than 1 %, respectively. Moreover, powder X-ray diffractograms of both UiO-66-NH₂ and MIL-125-NH₂ obtained before and after 40 water ad-/desorption cycles do not show any alteration of the crystal structure.

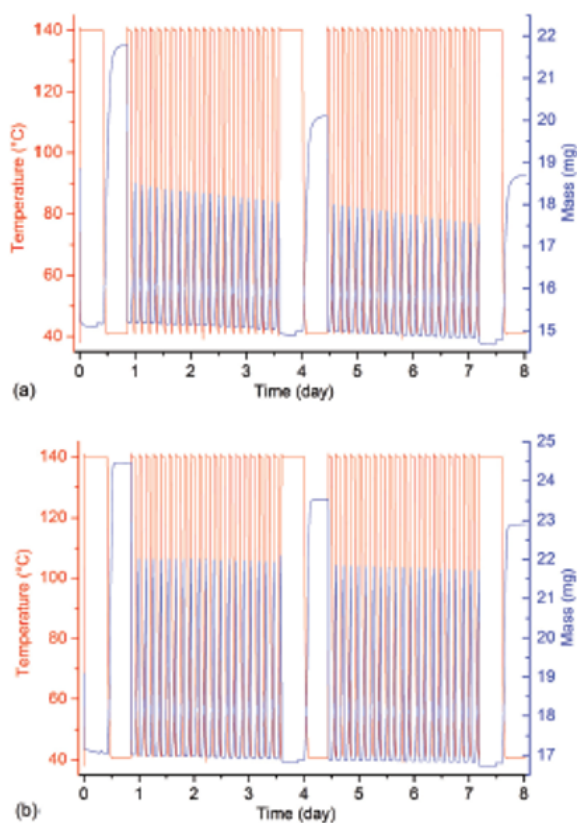


Figure 3.11. Hydrothermal cycle stress tests with temperature profile and load signal of (a) $\text{H}_2\text{N-UiO-66}$ and (b) $\text{H}_2\text{N-MIL-125}$ [42].

Recently Cadiau et al. [48] reported a multiple cycle experiment on MIL-160, demonstrating excellent hydrothermal stability of this MOF (adsorption at 303 K in humid nitrogen (RH 80%) and desorption at 373 K in nitrogen (RH 0.03%)).

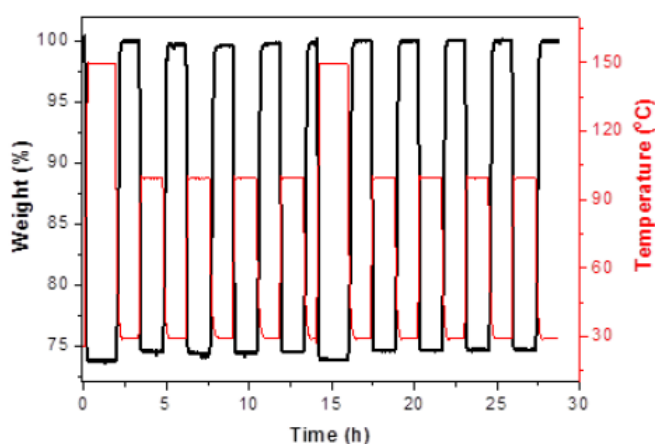


Figure 3.12. Thermogravimetric analysis profile for multiple cycles of water adsorption-desorption of MIL-160. Test conditions: adsorption at 303 K in humid nitrogen (RH 80%) and desorption at 373 K in nitrogen (RH 0.03%) [48].

Good stability is shown also by CAU-10(Al), isostructural to MIL-160, after 100 cycles between 40 °C and 140 °C under constant water vapour pressure of 5.6 kPa [46].

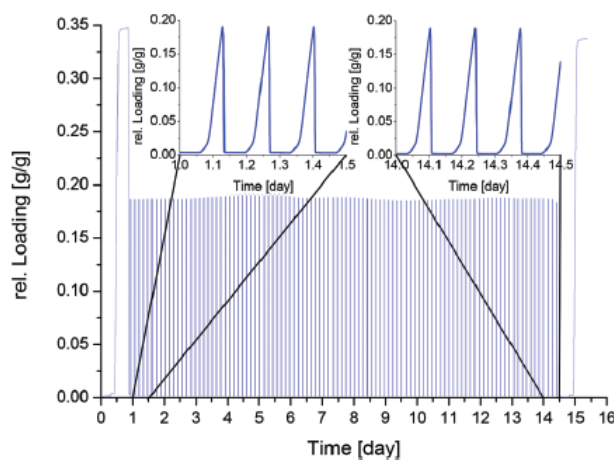


Figure 3.13. Thermogravimetric cycling test of CAU-10-H at constant humidity [46].

Hydrothermal stability experiment MIL-100(Fe) has been performed with very promising results, showing only a slight degradation of approximately 3% compared to the initial load after 40 cycles.

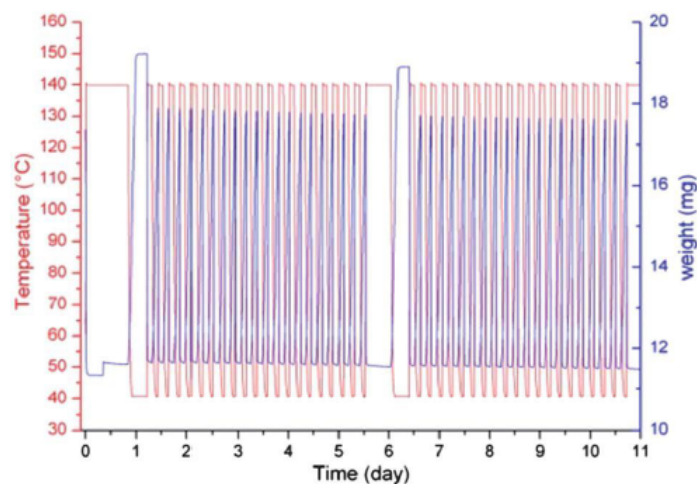


Figure 3.14. Temperature profile and load signal of the MIL-100(Fe) cycling experiment, acquired at $p = 5.6$ kPa [50].

At the end, we can conclude that MIL-100, MIL-101, UiO-66, MIL-125, CPO-27, MIL-160, CAU-10 and MIL-53 families and some composites and functionalization of them, which are the most used or tested for thermal energy storage, do not show degradation upon water vapour exposure neither big decrements in water uptake upon cycling, so they are hydrothermally stable.

3.2 MOFs and adsorptive thermal energy storage: the choice

Achieving the aim to improve the current state of the art of adsorptive thermal energy storage passes through the discovery and development of materials with adsorption properties that practically suit the operating conditions of open and closed TES systems. It means that simply screening energy storage density or water uptake values and choosing the highest ones represents a misleading method to select the appropriate sorbent.

Indeed, on one hand, comparing energy densities of two materials without taking into account the boundary conditions of temperature and pressure at which they have been tested is useless. Since one could have a higher energy density maybe resulting from a thermal characterization performed, compared to the other, at higher relative vapour pressure, which does not suit the application needs, this approach leads to misjudgments. On the other hand, high water uptakes come from high affinity between sorbate and sorbent, which, in turn, leads to higher desorption temperatures ($> 200 - 300$ °C), excluding the possibility of using low temperature heat sources (e.g. solar radiation, engine wastes, industrial wastes etc.). Weak sorbate-sorbent interactions, of course, are auspicious for desorption but unfavorable for adsorption, since they do not lead to sufficient driving force for sorbate sucking [36].

Therefore, a careful analysis that takes into account all these parameters and find a compromise between best performances and practical boundary conditions should be carried out. The following paragraphs will show the assessments that have been issued to choose which MOFs characterize and at which conditions.

3.2.1 Adsorbent selection criteria for TES

The parameters considered to perform the selection of MOFs are:

- energy storage capacity $\left[\frac{Wh}{kg_{ads}} \right]$;
- desorption temperature [°C];
- position of relative vapour pressure at which steep increase in adsorption occurs, p/p_0 ;
- hydrothermal stability.

In the field of thermal energy storage, energy storage density is the most important figure of merit. As mentioned above, the energy storage density of a material is defined as the amount of energy stored per unit of volume of the material. Respectively, the energy storage capacity of a material is defined as the amount of energy stored per unit of mass of the material. In the particular case of TCMs, they can be expressed by the following equations:

$$\rho_{Q-m} = \Delta H_{ads} \cdot (x_{max} - x_{min}) \quad (3.13)$$

$$\rho_{Q-v} = \Delta H_{ads} \cdot (x_{max} - x_{min}) \cdot \rho_{pack} \quad (3.14)$$

where, ΔH_{ads} is the differential heat of adsorption (or heat of reaction) in [J/g_{water}], x_{max} and x_{min} [g_{water}/g_{ads}] are the maximum and minimum adsorption amount of water over

the anhydrous adsorbent material mass, i.e. the maximum cycle loading lift, and ρ_{pack} [$\text{g}_{\text{ads}}/\text{m}^3_{\text{ads}}$] is the packing density of adsorbent.

Usually, energy density is preferable because the occupied volume can be an issue, for instance, in the domestic sector. Nevertheless, since the packing density depends not only on crystallographic density, but also on particle size and shaping treatment, it is easier to use energy storage capacity, in order to compare different adsorbent materials.

As mentioned above, energy storage capacity cannot be considered an absolute value, since it depends on the boundary conditions at which it is evaluated. Thus, the choice of the optimal adsorbent for thermal energy storage relies on the evaluation of these two criteria:

1. the desorption temperature range, which depends on the heat source used: in case of solar energy source (conventional flat solar collectors) ¹, an adsorbent able to be regenerated in the range 80-100 °C would be desirable;
2. the correlation between operating conditions and water sorption behavior of material: an adsorbent performing adsorption-desorption at a relative vapour pressure range p/p_0 , which both is in line with operating conditions given by the application and maximizes the cycling loading lift, should be found.

The first criterion, desorption temperature, has apparently more degrees of freedom, since it depends on the heat source used. In fact, the purpose is to use green energy, e.g. solar energy, or to recover waste heat from industrial processes or engines, which means that we are dealing with low temperature heat sources, thus low desorption temperatures are desirable.

The second criterion depends on both the thermal energy storage system adopted, i.e. closed or open one, and the application domain.

In the following paragraphs, these two criteria will be quantified for open and closed systems, focusing on winter solar driven space heating application boundary conditions.

The optimal adsorbent for a *closed system* can be graphically represented in an Arrhenius diagram (see Fig. 3.15), as the one which maximizes the water exchange between adsorption and desorption, i.e. the difference between the richest (green) and the weakest (red) isostere of the cycle.

The adsorption-desorption closed cycle is defined by two temperatures and two pressures:

- the highest desorption temperature (point D), which depends on the heat source and in case of solar collectors ranges from 80 to 100 °C;
- the minimum adsorption temperature (point B), which depends on the user needs and in case of space heating application is 30 °C;
- the condenser and evaporator pressure (and the relative temperatures), which depend on the heat source/sink available.

¹In the case of conventional flat collectors, the maximum available level of temperature to design a storage process can be estimated around 70/80 °C. At temperatures higher than 80 °C, the flat collectors efficiency which depends on the temperature of the heat transfer fluid falls quickly and penalizes the whole process.

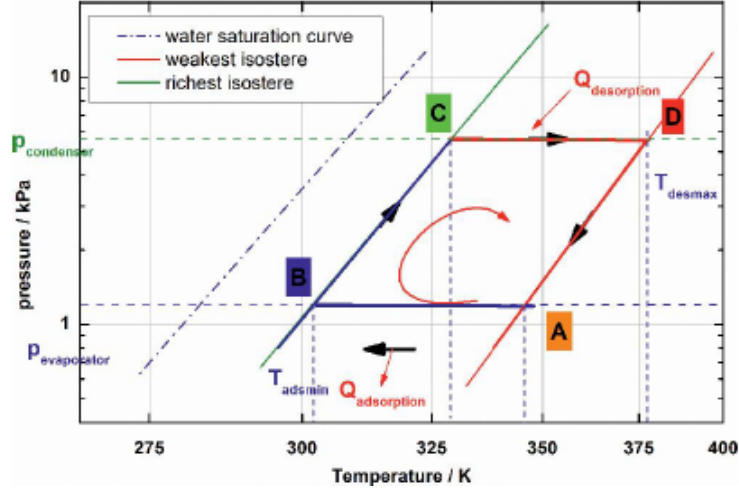


Figure 3.15. The van't Hoff diagram of the ideal cycle [43].

In Table 3.1, Aristov [36] reports the minimal desorption temperature and the corresponding relative pressure of water vapor for several sets of boundary evaporation and condensation temperatures, which are practically important for adsorptive heat transformations.

The ideal water adsorbent for closed TES driven by low temperature heat, i.e. at less than 100 °C, should have a steep increase of sorption at p/p_0 between 0.10 and 0.30 and it should be possible to regenerate it at relative pressure above 0.02. The adsorbents which exchange water at p/p_0 between 0.30 and 0.45 might be used only at the marginal (and more difficult to reach) conditions: $T_{\text{eva}} > 10 - 15^\circ\text{C}$ and $T_{\text{cond}} < 30^\circ\text{C}$ [36].

		$T_{\text{cond}} [^\circ\text{C}]$				
		25	30	35	40	45
T_{eva} [$^\circ\text{C}$]	0	52 (0.23)	63 (0.19)	74 (0.15)	85 (0.13)	97 (0.11)
	5	46 (0.31)	57 (0.25)	68 (0.20)	79 (0.16)	91 (0.13)
	10	41 (0.41)	51 (0.33)	62 (0.26)	73 (0.21)	85 (0.17)
	15	35 (0.56)	46 (0.42)	56 (0.34)	66 (0.28)	78 (0.22)

Table 3.1. The minimal desorption temperature and corresponding relative pressure of water vapor (in parentheses) [36].

The choice of the optimal water adsorbent for an *open system*, since it does not require evaporation and condensation, depends only on temperature and water vapour content (i.e. relative humidity) of the air stream that charges/discharges the storage medium. For space heating application, in case of open reactor:

- during discharging, humid air from the ventilation system, in winter period, is at 20 °C and 50% relative humidity;
- during charging, dry air is provided to the adsorbent at 80-100 °C (considering low temperature heat sources) and almost 0% relative humidity.

This means that the ideal adsorbent should adsorb water at relative pressure p/p_0 0.5 and desorb at p/p_0 almost zero and also maximize in this range of pressures the cycling loading lift.

Summarizing, low desorption temperatures and adsorption properties that both suit operating conditions given by the application and maximize the cycling loading lift, are the main criteria that should be adopted in choosing the ideal adsorbent material. However, it should not forget, before this screening procedure, to take into account hydrothermal stability, i.e. stability upon cycling, in order to ensure that estimated performances can be actually realized.

	ADSORPTION		DESORPTION	
	T [°C]	p/p ₀ [-]	T [°C]	p/p ₀ [-]
OPEN	20	0.5	80 ÷ 100	0
CLOSED	30	0.1 ÷ 0.3	80 ÷ 100	> 0.02

Table 3.2. Adsorbent selection criteria for open and closed TES - space heating application.

3.2.2 Selection criteria applied to MOFs: the steps of choice

Low temperature driven regeneration, suitable adsorption step position (p/p_0), combined with the highest possible cycling loading lift and energy density, as well as hydrothermal stability seem to be the key factors to choose the best adsorbent for thermal energy storage. The latest research studies have pointed out that MOFs are promising candidates as sorption materials in this field.

Among a huge number of different metal-organic frameworks known in literature, water stable ones have been selected and it has been looking for the ones showing the best performances. Thus, a first screening was carried out just looking at the energy storage capacities of already tested MOFs, as a function of desorption temperature, comparing them with all adsorbent material categories.

Then, adsorption step position has been compared in order to assess their suitability for open or closed systems. Since MOFs have been mostly tested at temperature and pressure conditions typical of closed systems, it has made the choice to test the most promising ones at open systems boundary conditions.

Here, all the steps of choice and remarks made are reported.

Firstly, a water stable set of MOFs and MOF-based composites have been selected, according to literature knowledge as already shown in subsection 3.1.3, and their properties are shown in the following paragraphs and resumed in Tables 3.3 and 3.4.

Here, the selected set: (Cr)MIL-101, (Zr)UiO-66-NH₂, (Ti)MIL-125-NH₂, (Fe)MIL-100, (Al)CAU-10, (Al)MIL-160, (Ni)CPO-27, (Fe)MIL-100 + CaCl₂, (Cr)MIL-101 + CaCl₂, (Ti)MIL-125-NH₂ + CaCl₂ and (Zr)UiO-66-NH₂ + CaCl₂.

REF.	LABEL	PORE SIZE [nm]	PORE VOLUME [cm ³ /g]	SURFACE AREA [m ² /g]	^a p/p ₀ [-]	WATER UPTAKE MAX [g/g]
[47]	CPO-27(Ni)	1.2	0.5	1226	0.02	0.47
[37]	MIL-100(Fe)	2.5/2.9	0.82	1549	0.25 ÷ 0.35	0.8
[38]	MIL-101(Cr)	2.9/3.4	1.22	2500	0.4 ÷ 0.5	1.43 [43]
[38]	MIL-125(Ti)-NH ₂	0.6/1.2	0.51	1230	< 0.2	0.36
[38]	UiO-66(Zr)-NH ₂	0.75/1.1	0.35	830	0.1 ÷ 0.3	0.36
[19]	MIL-100(Fe) + (46%)CaCl ₂	-	0.13	290	-	0.57
[19]	MIL-101(Cr) + (62%)CaCl ₂	-	0.19	330	-	0.75
[19]	MIL-125(Ti)-NH ₂ + (45%)CaCl ₂	-	0.24	360	-	0.46
[19]	UiO-66(Zr)-NH ₂ + (43%)CaCl ₂	-	0.13	310	-	0.47
[42]	CAU-10(Al)	0.5	0.27	525	0.15	0.33
[48]	MIL-160(Al)	0.5	0.4	1070	0.08	0.37

Table 3.3. MOF selection - pore and surface characteristics and adsorption behavior from water adsorption isotherms at 298 K (^aposition of steep increase in water uptake from adsorption isotherms).

REF.	LABEL	T _{ads} [°C]	P _{ads} [mbar]	T _{des} [°C]	P _{des} [mbar]	P/P ₀ [-]	CYCL. LOAD. LIFT [g/g]	HEAT ADSORP. [kJ/mol]	ENERGY STOR. CAPACITY [Wh/kg]	SYSTEM TYPE
[23]	CPO-27(Ni)	25	23.1	100	32.5	0.7	-	-	170	CLOSED
[19]	MIL-100(Fe)	30	12.5	80	12.5	0.3	0.32	^a 48.83	^b 241	CLOSED
[19]	MIL-101(Cr)	30	12.5	80	12.5	0.3	0.12	^a 46	^b 85	CLOSED
[19]	MIL-125(Ti)-NH ₂	30	12.5	80	12.5	0.3	0.37	56.45	^b 322	CLOSED
[19]	UiO-66(Zr)-NH ₂	30	12.5	80	12.5	0.3	0.32	52.68	^b 260	CLOSED
[19]	MIL-100(Fe) + (46%)CaCl ₂	30	12.5	80	12.5	0.3	0.47	-	335	CLOSED
[19]	MIL-101(Cr) + (62%)CaCl ₂	30	12.5	80	12.5	0.3	0.58	-	485	CLOSED
[19]	MIL-125(Ti)-NH ₂ + (45%)CaCl ₂	30	12.5	80	12.5	0.3	0.35	-	243	CLOSED
[19]	UiO-66(Zr)-NH ₂ + (43%)CaCl ₂	30	12.5	80	12.5	0.3	0.33	-	268	CLOSED
[32]	CAU-10(Al)	25	10	150	10	0.3	-	-	139	CLOSED
[32]	MIL-160(Al)	25	10	150	10	0.3	-	-	219	CLOSED

Table 3.4. MOF selection - adsorption properties at test conditions (^aheat of adsorption from Henninger et al. [43]; ^b energy storage capacity calculated).

Mesoporous (Cr)MIL-101 and (Fe)MIL-100

MIL-101 and MIL-100 mesoporous MOFs are made by trinuclear clusters (Cr³⁺ and Fe³⁺, respectively) and 1,3,5-benzene tricarboxylate organic linker for MIL-100 and benzene-1,4-dicarboxylate for MIL-101. Two dimensions of pore are detected in their structure: 2.5 and 2.9 nm for MIL-100 and 2.9 and 3.4 nm for MIL-101.

They have similar type-V adsorption isotherms, as shown in Fig. 3.17, but different water uptakes and pressures at which the step increase in adsorption happens:

- the maximum water uptake is about 0.8 cm³/g for MIL-100 while 1.43 cm³/g for MIL-101;
- the relative pressure falls between 0.25 and 0.35 for MIL-100, corresponding to consecutive filling of first the 2.5 nm mesopores, then the 2.9 nm ones; for MIL-101, the filling of the 2.9 nm pores closely followed by that of the 3.4 nm pores happens in pressure range 0.4-0.5.

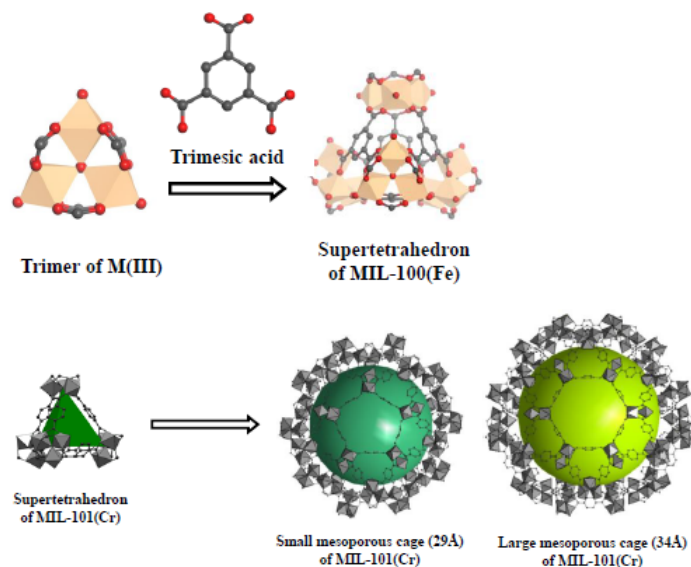


Figure 3.16. (Above) Structure of MIL-100(Fe): Iron atoms are shown in orange, oxygen in red and carbon in grey; (below) Structure of MIL-101(Cr) representing two mesoporous cages of 2.9 nm and 3.4 nm: Chromium atoms are shown in grey and others (carbon and oxygen) in black [45].

MIL-101 shows a higher water uptake and a more hydrophobic behavior (higher relative pressure at which adsorption occurs), compared to MIL-100: the first result is due to increased pore volume of MIL-101 (see Table 3.3) while the second can be explained with the higher organic content of MIL-101.

Heat of adsorption of MIL-101 and MIL-100 was measured by Henninger et al. [43] and results, respectively, 46 kJ/mol and 48.83 kJ/mol, which are close to the evaporation enthalpy of water (44 kJ/mol at 25 °C). Thus, their enthalpy of adsorption result 828 kJ/g_{H₂O} and 878.94 kJ/g_{H₂O}.

Energy storage capacity can be calculated by multiplying enthalpy of adsorption by the cycling loading lift (water exchange between adsorption and desorption), which Permyakova found equal to 0.12 g_{H₂O}/g_{sample} and 0.32 g_{H₂O}/g_{sample}, respectively. The result is 85 Wh/kg for MIL-101 and 241 Wh/kg for MIL-100.

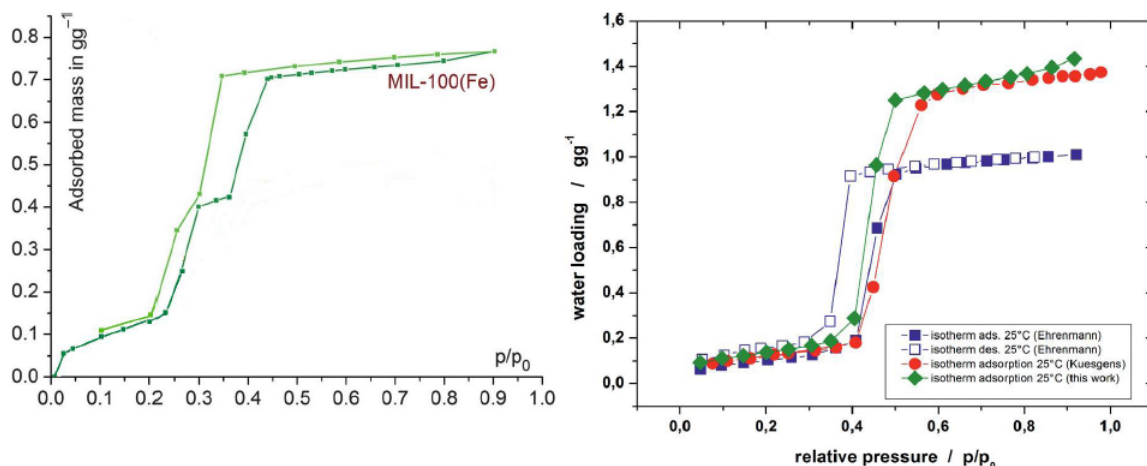


Figure 3.17. Water adsorption and desorption isotherms at 25 °C: (left) MIL-100 [19] and (right) MIL-101 [43].

Microporous (Zr)UiO-66-NH₂ and (Ti)MIL-125-NH₂

UiO-66-NH₂ and MIL-125-NH₂ microporous MOFs are made by octahedra, Zr₆O₄(OH)₄ and TiO₅(OH) respectively, forming lattices with 12-fold connection through 2-amino-benzene-1,4-dicarboxylate organic linker. Two dimensions of pore are detected in their structure: 0.8 and 1.1 nm for UiO-66-NH₂ and 0.6 and 1.2 nm for MIL-125-NH₂.

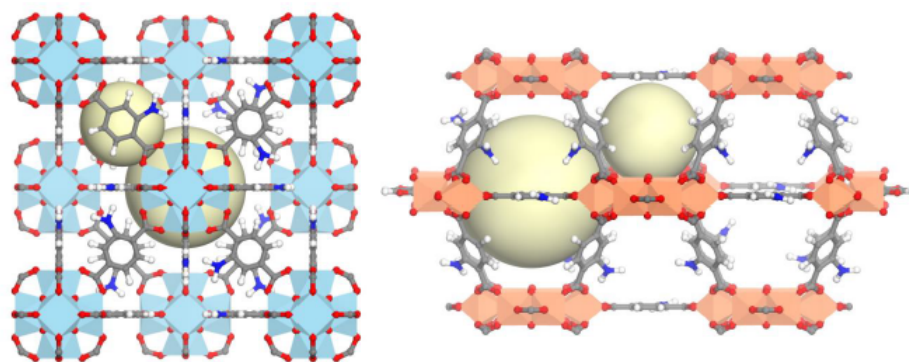


Figure 3.18. (Left) UiO-66-NH₂: Zirconium atoms are shown in Cambridge blue, oxygen in red, nitrogen in Oxford blue and carbon in grey; (right) MIL-125-NH₂: Titanium atoms are shown in orange, oxygen in red, nitrogen in Oxford blue and carbon in grey [45].

They have similar type-V adsorption isotherms, as shown in Fig. 3.19, and the same water uptake, 0.36 cm³/g, but different pressures at which the step increase in adsorption happens:

- the relative pressure falls between 0.1 and 0.3 for UiO-66-NH₂, due to the enhanced hydrophilicity by NH₂-groups; for MIL-125-NH₂, even more pronounced hydrophilic

behavior is shown, since 73% of its total loading occurs at a relative pressure below $p/p_0 = 0.2$.

Heat of adsorption of UiO-66-NH₂ and MIL-125-NH₂ was measured by Permyakova [19] and results, respectively, 52.68 kJ/mol and 56.45 kJ/mol. Thus, their enthalpy of adsorption results 948.24 kJ/g_{H₂O} and 1016.1 kJ/g_{H₂O}.

Energy storage capacity can be calculated by multiplying enthalpy of adsorption by the cycling loading lift, which Permyakova found equal to 0.32 g_{H₂O}/g_{sample} and 0.37 g_{H₂O}/g_{sample}, respectively. The result is 260 Wh/kg for UiO-66-NH₂ and 322 Wh/kg for MIL-125-NH₂.

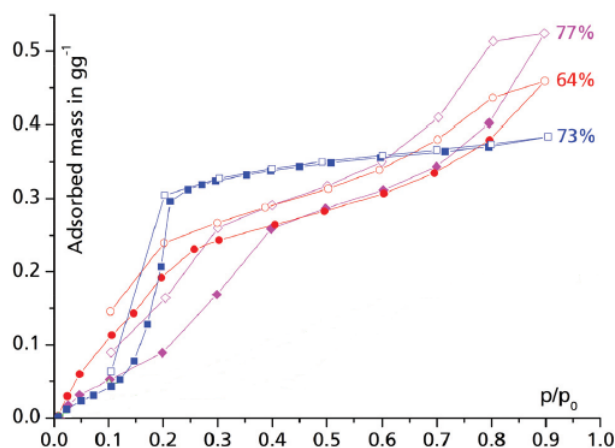


Figure 3.19. Water adsorption and desorption isotherms at 25 °C of UiO-66 (in violet), UiO-66(Zr)-NH₂ (in red) and MIL-125-NH₂ (in blue); (Adsorption: filled symbols; desorption: empty symbols) [42].

Microporous CAU-10(Al) and MIL-160(Al)

CAU-10(Al) and MIL-160(Al) microporous MOFs are made by the same inorganic unit, AlO₆-polyhedra, and different organic linkers, isophthalic acid and 2,5-furandicarboxylic acid, respectively. This assemblage results in square-shaped, sinusoidal channels, which exhibit a maximum free diameter of 0.5 nm.

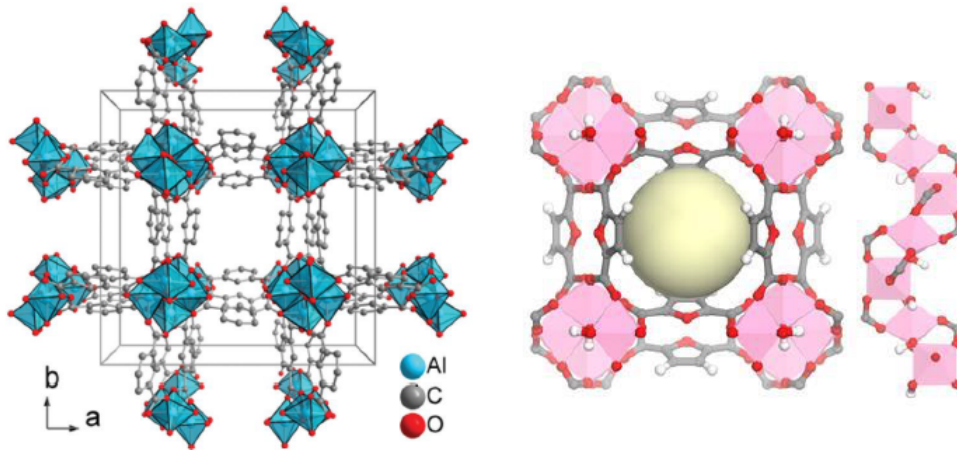


Figure 3.20. (Left) CAU-10(Al): Aluminum atoms are shown in blue, oxygen in red and carbon in grey; (right) MIL-160(Al): Aluminum atoms are shown in rose, oxygen in red and carbon in grey [45].

MIL-160 shows adsorption isotherms with a shape similar to type-I, as shown in Fig. 3.21, since it has a more hydrophilic behavior compared to CAU-10, which isotherm presents a type-V shape. Also the water uptake is a little bit enhanced for MIL-160. Indeed:

- the relative pressure at which the steep increase occurs is 0.08 for MIL-160, otherwise it is shifted at 0.15 for CAU-10;
- MIL-160 maximum water uptake is slightly higher than CAU-10, i.e. 0.37 g/g vs. 0.33 g/g, even if at relative pressure 0.3 this difference increases (0.35 g/g vs. 0.30 g/g).

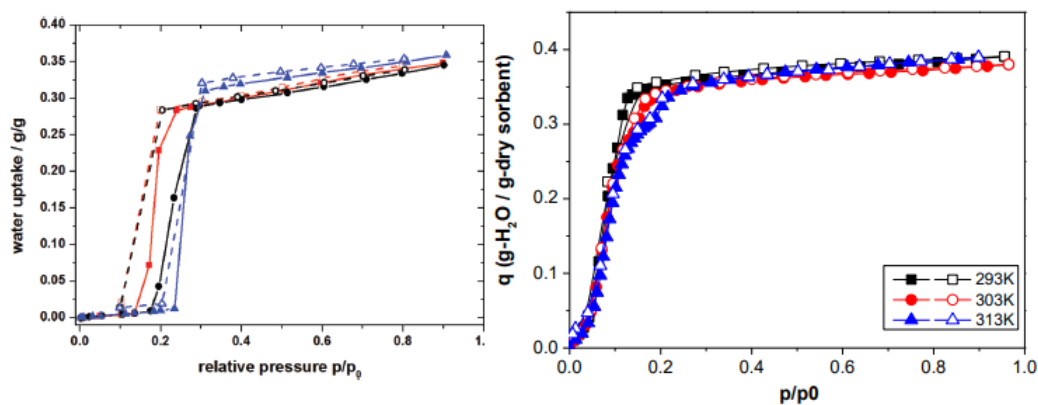


Figure 3.21. Water adsorption and desorption isotherms: (left) CAU-10 at 25 °C (red), 40 °C (black) and 60 °C (blue) [42]; (right) MIL-160 (Adsorption: filled symbols; desorption: empty symbols) [48].

Energy storage capacity has been taken from Leenders [32], who carried out experimental STA tests, i.e. simultaneous thermogravimetric analysis and differential scanning calorimetry. Thus, the integration of heat flow curve gives already the energy storage capacity relative to the boundary conditions chosen.

The result is 139 Wh/kg for CAU-10 and 219 Wh/kg for MIL-160.

Microporous CPO-27(Ni)

CPO-27 microporous MOF is made by Nickel nodes as inorganic unit, and 2,5 Dihydroxyterephthalic acid as organic linker, forming a crystal structure that resembles a honeycomb. The channels have an accessible diameter of approximately 1.2 nm.

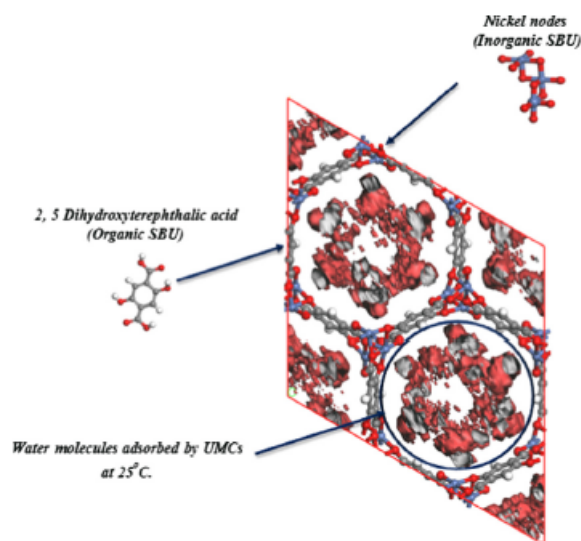


Figure 3.22. Crystal structure of CPO-27(Ni) with the adsorbed water molecules (H, O, C, Ni are in white, red, grey and violet respectively) [23].

CPO-27 shows a type-I adsorption isotherm, as shown in Fig. 3.23, reaching 81% of its capacity at a very low relative pressure and then a long saturation plateau as usually found for zeolites, synonym of very hydrophilic behaviour. Indeed:

- the relative pressure at which the steep increase occurs is 0.02;
- the maximum water uptake is 0.47 g/g.

Energy storage capacity has been taken from Elsayed et al. [23], who carried out numerical simulations with closed system boundary conditions. For an evaporation temperature of 20 °C, a condensation temperature of 25 °C, an adsorption temperature of 25 °C and a regeneration temperature of 100 °C, the result was 170 Wh/kg.

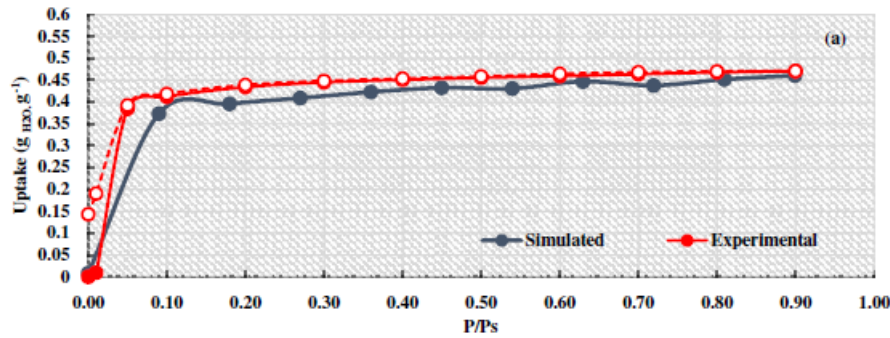


Figure 3.23. Water adsorption and desorption isotherms of CPO-27(Ni) at 25 °C [47].

MOF-based composites

Interesting adsorption properties of MOF-based composites, i.e. inorganic salts confined in a porous host matrix, have been experimentally proved by Permyakova [19]. CSPM (composites “salts in porous matrix”) have the aim of both avoiding deliquescence and agglomeration phenomena, which are typical of chemical reactions and badly affect cycling stability, and combining the best properties of physical and chemical adsorbents. If, on one hand, inorganic salts show high energy densities, i.e. high enthalpy of reaction and water uptakes due to stronger sorbate-sorbent interactions, on the other hand this leads to higher regeneration temperatures and slow kinetics. On the contrary, physical adsorbents, such as MOFs, due to weaker interactions involved, exhibit lower desorption temperatures and faster kinetics. The expected result, thus, is a material having a higher energy density, compared to the pristine physisorbent, and with a lower desorption temperature, compared to the pristine chemisorbent.

As shown by Permyakova work, composites performance could be significantly tuned by varying both the salt content and the pore size of the host matrix, i.e. the hydrophilic–hydrophobic balance.

Tables 3.3 and 3.4 list the composites tested: MIL-100(Fe) + (46%)CaCl₂, MIL-101(Cr) + (62%)CaCl₂, MIL-125(Ti)-NH₂ + (45%)CaCl₂ and UiO-66(Zr)-NH₂ + (43%)CaCl₂. Closed system boundary conditions were chosen: T_{des} = 80 °C, typical of a solar collector), T_{ads} = 30 °C, minimum adsorption temperature for space heating during the winter period while evaporation and condensation temperatures of 10 °C corresponding to a pressure of 12.5 mbar. Calcium chloride was selected as inorganic salt, since it is largely available, cheap and has a hydration rate (i.e. 5 moles of water per mole of CaCl₂) that falls under the operating conditions chosen.

What has been pointed out is that the best performances are achieved by MIL-100(Fe) and MIL-101(Cr), as host matrices, showing an energy storage capacity of 335 Wh/kg and 285 Wh/kg, respectively. This result allows to consider that are preferable:

- more hydrophobic MOFs, since this adsorption behaviour enhances desorption, allowing lower regeneration temperatures;
- mesoporous MOFs, since the higher the pore volume, the better is the compromise found between a high salt content, which enhances water uptake, and a high MOF residual pore volume, which avoids salt dehydration to be hampered by the very slow diffusion of water.

Finally, the use of amphiphilic MOFs (both hydrophobic and hydrophilic, such as mesoporous MIL-100 and MIL-101), bearing intermediate salt loadings, leads to a synergetic effect between water chemisorption of the salt and the physisorption of the MOF, resulting in better performances compared with those of the pure MOFs or salt.

Discussion

In view of the mentioned selection criteria, needed to take into account both the adsorption behaviour and the application requirements and perform the correct choice, the steps that have been followed are here described.

Firstly, the highest energy storage capacity, as shown in Table 3.4, has been revealed by:

1. MIL-101(Cr) + (62%)CaCl₂ with 485 Wh/kg, among MOF-based composites;
2. MIL-125(Ti)-NH₂ with 322 Wh/kg, among pristine MOFs.

Knowing that this is not enough to make a choice, since it is needed to consider the boundary conditions related to energy storage capacity values, we move to the next step: have a look at the relative vapour pressure p/p_0 at which the selected MOFs were tested.

Looking at Table 3.4, it is possible to see that all the water stable selected MOFs were tested under closed system TES boundary conditions: indeed, except for (Ni)CPO-27, adsorption temperature and pressure bring to a relative pressure p/p_0 equal to 0.3. It was decided, then, to choose one pristine MOF and one MOF-based composite and test them under open system operating conditions, since it was not found any paper that has already done it. The ones with the highest energy storage capacity were chosen:

- MIL-101(Cr) + (62%)CaCl₂ with 485 Wh/kg, as an example of MOF-based composite;
- MIL-125(Ti)-NH₂ with 322 Wh/kg, as an example of pristine MOF.

MIL-101 composite should significantly overcome the reported value of energy density, since Permyakova analysis, as shown in Fig. 3.24, pointed out that pristine MIL-101 exhibits the major part of water uptake in the relative pressure range $0.3 \div 0.5$. Thus, it was found interesting to test it under open reactor operating conditions ($p/p_0 = 0.5$), because a steep increase in water uptake should be observed and consequently a higher energy storage capacity.

In MIL-125-NH₂, according to Fig. 3.24, the major part of water uptake occurs in the p/p_0 range $0.1 \div 0.3$. It means that an irrelevant increment in water uptake and energy storage capacity with respect to reported values is expected, testing it at relative pressure of 0.5.

MIL-101(Cr) synthesis, unfortunately, was not successful, even after following two different procedures, by Khutia et al. [41] and by Permyakova [45]. Thus, it was decided to test:

- pristine MIL-125-NH₂;
- two composites, MIL-125-NH₂ + (45%)CaCl₂, already tested by Permyakova [45], and MIL-125-NH₂ + (45%)SrBr₂.

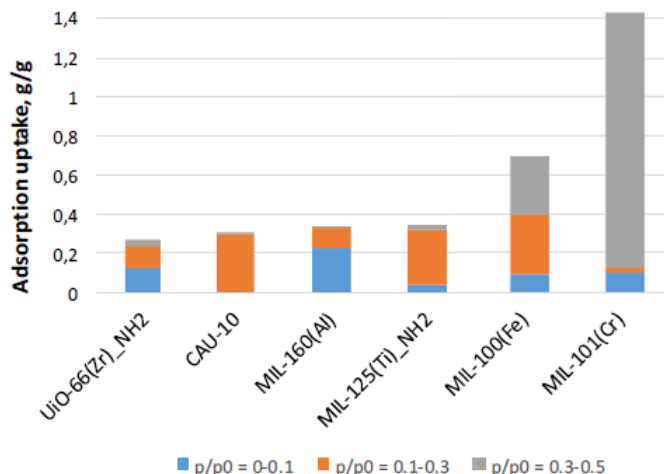


Figure 3.24. Water uptake capacity of water stable and recyclable MOFs in different pressure ranges: 0-0.1; 0.1-0.3; 0.3-0.5. The large portion of water uptake capacity indicates that the pore filling or condensation occurs in this pressure range. [45].

MIL-125-NH₂ + SrBr₂ composite has not already been tested, according to literature data. It was found interesting to synthesize it, since SrBr₂ is a very promising candidate among inorganic salts, owing to its very high energy storage density. Indeed, ideal energy density of 630 kWh/m³ or 264 Wh/kg (referring to the bulk density of 2390 kg/m³ and molar mass of non-porous hydrated salt 0.35 kg/mol) [49] but also looking at small scale of prototype reactor, energy densities relative to the reactive bed volume were found to be higher than 400 kWh/m³.

Resume and objectives of the work

After the analysis of the state of the art of MOFs, in the context of TES adsorbent materials, it has been found that this new category is very promising in terms of hydrothermal stability and energy storage capacity, even at low desorption temperature. Moreover, it has been underlined the importance of taking into account the boundary conditions at which materials have been tested. Since, in literature, experimental and numerical results of MOFs tested under closed system operating temperature and pressures were reported, it was decided that the aim of this thesis project would have been to investigate on selected MOFs performances at open system testing conditions.

The path through available data of a set of water stable MOFs brought us to the idea of testing MIL-101(Cr) + (62%)CaCl₂ and MIL-125-NH₂. However, practical obstacles did not let MIL-101 synthesis be successful. Thus, after a rearrangement of plans, two composites, MIL-125-NH₂ + (45%)CaCl₂ and MIL-125-NH₂ + SrBr₂ and pristine MIL-125-NH₂ have been tested.

Firstly, XPRD (X-ray powder diffraction) was performed on the samples in order to characterize their exact chemical composition, comparing the XPRD patterns obtained with the known patterns of each material.

Secondly, TG-DSC tests, i.e. simultaneous thermogravimetric and differential scanning

calorimetric analyses, were carried out on each sample, by using two different set-up:

- **PATTERN 1** to test hydrothermal stability, performing 6 adsorption/desorption cycles under open system operating conditions, thus 20 °C adsorption temperature and 11.6 mbar adsorption pressure, which correspond to 50% relative humidity and 80 °C dry air desorption temperature; from this pattern, heat of adsorption and cycling loading lift were extracted in order to obtain energy storage capacity of the material;
- **PATTERN 2** to test kinetics of adsorption, in particular, studying the influence of water vapour pressure (thus, keeping constant adsorption temperature 20 °C), by making it varying from 6.9 mbar (30% RH) to 11.6 mbar (50% RH) and finally to 18.5 mbar (80% RH).

Finally, nitrogen adsorption isotherms have been carried out, in collaboration with the Laboratoire de Physique Subatomique et des Technologies Associées SUBATECH of Nantes. Pore size, pore volume and specific surface area were calculated from those experimental results.

Chapter 4

Experimental methods

In this chapter, the methodologies applied to synthesize the samples of material and to perform each kind of characterization test have been explained.

4.1 Materials development

4.1.1 Chemical constituents

Tables 4.1 and 4.2 itemize the chemical compounds, their quantities and suppliers, used in the synthesis procedure of each sample. These chemicals were used without any further purification.

Ti-MIL-125-NH₂

LABEL	DESCRIPTION	QUANTITY*	SUPPLIER
NH ₂ -BDC	2-Aminoterephthalic acid, 99%	5.430 g	Alfa Aesar
DMF	N,N-dimethylformamide	17.5 ml	Alfa Aesar
MeOH	Methanol	17.5 ml	Alfa Aesar
Ti(BuO) ₄	Titanium butoxide	2.55 ml	Alfa Aesar

Table 4.1. Ti-MIL-125-NH₂ chemical constituents [39].*quantities multiplied by five wrt ref.

Composite: Ti-MIL-125-NH₂ + (45%)CaCl₂

LABEL	DESCRIPTION	QUANTITY	SUPPLIER
(1)Ti-MIL-125-NH ₂	Titanium based MOF	80 mg	this work
30% CaCl ₂ sol.	Salt solution	0.8 ml	Alfa Aesar

Table 4.2. Ti-MIL-125-NH₂+(45%)CaCl₂ composite chemical constituents [19].

Composite: Ti-MIL-125-NH₂ + (45%)SrBr₂

LABEL	DESCRIPTION	QUANTITY	SUPPLIER
(2)Ti-MIL-125-NH ₂	Titanium based MOF	80 mg	this work
30% SrBr ₂ sol.	Salt solution	0.8 ml	Alfa Aesar

Table 4.3. Ti-MIL-125-NH₂+(45%)SrBr₂ composite chemical constituents.**4.1.2 Synthesis and activation****Ti-MIL-125-NH₂**

Ti-MIL-125-NH₂ was synthesized and activated following the procedure below [39]. NH₂-BDC was completely dissolved in a solution of anhydrous DMF and MeOH by sonication. Ti(BuO)₄ was added to the solution and it was sonicated for 5 min. The solution was then transferred to a Teflon-lined bomb reactor and kept in an oven at 150 °C for 16 h. After being cooled to room temperature, the yellow product was collected by filtration. The product was washed with DMF to remove unreacted organic ligands, and then DMF was replaced with MeOH by washing twice.

Since the reactor capacity was quite small, in order to obtain a bigger quantity of material, synthesis procedure was repeated twice, resulting in two different samples of material.

Composite: Ti-MIL-125-NH₂ + CaCl₂

Ti-MIL-125-NH₂+CaCl₂ composite was synthesized and activated following the procedure below [19].

CaCl₂ solution was prepared with 30% concentration of CaCl₂. Meanwhile, Ti-MIL-125-NH₂ sample 1 was dried for 3 hours in an oven at 100 °C, to dehydrate it. Then one encapsulation step using CaCl₂ solution was performed, with soaking time of 2 hours. The sample was collected following the removal of excessive CaCl₂ solution by evaporation and then it was completely dried at 100 °C in an oven for overnight.

Figure 4.1. MIL-125-NH₂ sample 1 (left), anhydrous CaCl₂ (middle), MIL-125-NH₂+(45%)CaCl₂ composite (right).

Composite: Ti-MIL-125-NH₂ + SrBr₂

Ti-MIL-125-NH₂+SrBr₂ composite was synthesized and activated following the procedure below.

SrBr₂ solution was prepared with 30% concentration of SrBr₂. Meanwhile, Ti-MIL-125-NH₂ sample 2 was dried for 3 hours in an oven at 100 °C, to dehydrate it. Then one encapsulation step using SrBr₂ solution was performed, with soaking time of 2 hours. The sample was collected following the removal of excessive SrBr₂ solution by evaporation and then it was completely dried at 100 °C in an oven for overnight.



Figure 4.2. MIL-125-NH₂ sample 2 (left), anhydrous SrBr₂ (middle), MIL-125-NH₂+(45%)SrBr₂ composite (right).

4.2 Characterization at microscopic scale

4.2.1 XRPD

Device description and working principle

XRPD, *X-ray powder diffraction*, is a non-destructive analytical technique applied on the analysis of crystalline solids lattices.

X-rays are electromagnetic radiations with a wavelength comparable (the same order of magnitude) to atomic spacings into the crystal lattice, which thus acts as optimal diffraction grating. That is the reason why X-rays are used to determine crystal structure, chemical composition, and physical properties of crystalline solids.

X-ray powder diffraction is based on observing the scattered intensity of an X-ray beam hitting a sample as a function of incident and scattered angle. The instrument used is a powder diffractometer, shown in Fig. 4.3, whose working principle is based on the Bragg's law:

$$2d \sin \theta = n\lambda \quad (4.1)$$

According to Bragg, diffraction occurs when both radiation is scattered in a specular fashion, i.e. with the same angle of incidence θ , by the lattice planes separated by the interplanar distance d (see Fig. 4.4) and this happens by means of constructive interference.

Interference is constructive when the scattered waves remain in phase, since the difference between the path lengths of the two waves ($2d \sin \theta$) is equal to an integer (n) multiple of

the wavelength (λ).

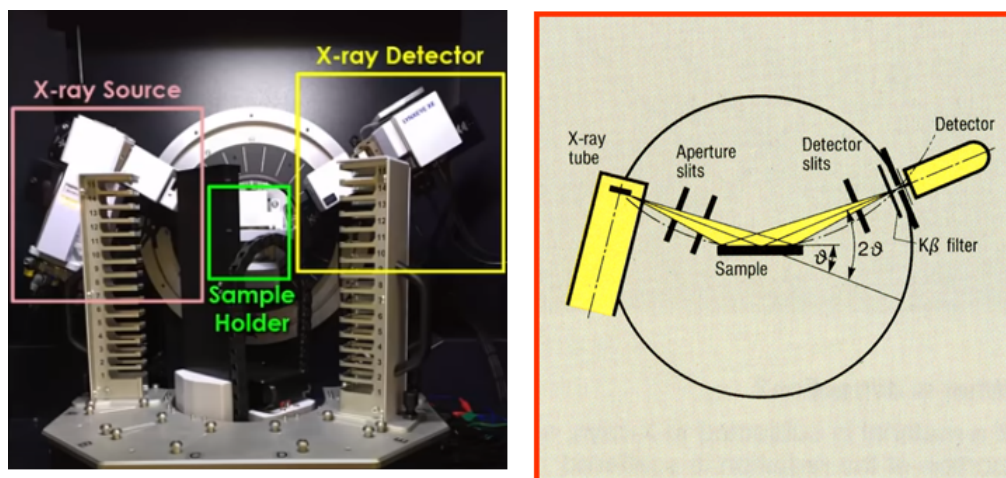


Figure 4.3. Powder diffractometer.

The diffraction pattern obtained shows the intensity of scattered waves as a function of the scattering angle. At the points where the scattering angles satisfy Bragg condition, since the intensity of diffracted waves is overlapped, diffraction peaks can be observed. The powder diffractometer is composed by a X-ray source and a X-ray detector, which are both set to form an angle θ with the sample holder. The diffraction pattern obtained, with all its intensity peaks, is the footprint of the crystalline solid. Comparing it with data bases, it is possible to derive the chemical composition and the crystal structure of the solid.

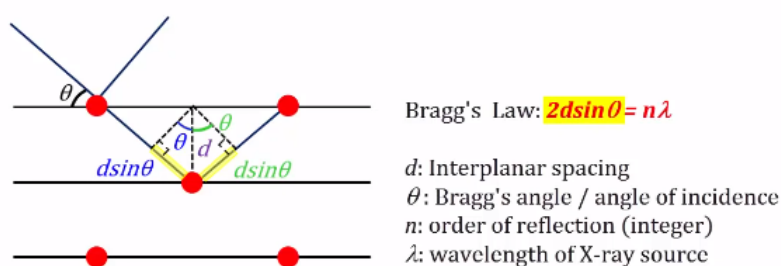


Figure 4.4. Bragg's law illustration.

Set-up of the tests

Powder X-ray diffraction patterns of MIL-125-NH₂, MIL-125-NH₂ + (45%)CaCl₂ and MIL-125-NH₂ + SrBr₂ samples were obtained on a Bruker D8 Advance diffractometer

using monochromatic Cu-K α radiation ($\lambda = 1.54 \text{ \AA}$). The pattern was recorded within the $5 \div 40^\circ 2\theta$ range, with a step of 0.02° , with a scan time of 3 s. The XRD measurements were done at 25°C . The experimental diffraction patterns were compared with known patterns of CaCl $_2$ and SrBr $_2$ based chemical compounds.

4.2.2 Adsorption isotherms

In this thesis project, nitrogen adsorption isotherms at 77 K have been performed in collaboration with the Laboratoire de Physique Subatomique et des Technologies Associées SUBATECH of Nantes. The pore volume, pore size and specific surface area have been calculated from the experimental results, as described in the following paragraphs.

Specific surface area

The Brunauer–Emmett–Teller (BET) method has been used to calculate the specific surface area S_{BET} .

It is one of the most widely used procedure for evaluating the surface area of porous materials. It is based of the BET theory, which is an adaptation of Langmuir monolayer adsorption model to the multilayer one, assuming that:

1. gas molecules only interact with adjacent layers;
2. the number of layers, as the pressure approaches the saturation pressure, tends to infinity and the adsorbed phase becomes a liquid.

The BET isotherm equation is:

$$\frac{1}{v \cdot [(p/p_0) - 1]} = \frac{1}{v_m c_{\text{BET}}} + \frac{c_{\text{BET}} - 1}{v_m c_{\text{BET}}} \cdot (p/p_0) \quad (4.2)$$

where v is the adsorbed amount [m^3], v_m is the monolayer adsorbed quantity [m^3], p and p_0 are the equilibrium and the saturation pressure [Pa] of adsorbate at the temperature of adsorption and c_{BET} is the BET constant.

The BET constant is expressed as:

$$c_{\text{BET}} = \exp\left(\frac{E_1 - E_L}{RT}\right) \quad (4.3)$$

where E_1 [J/mol] is the heat of adsorption for the first layer, and E_L [J/mol] is that for the second and higher layers and is equal to the heat of liquefaction.

The BET plot is obtained as a straight line with $\frac{1}{v \cdot [(p/p_0) - 1]}$ on the y-axis and p/p_0 on the x-axis according to experimental results.

The linearity of the BET plot may be limited to a small range of partial pressure, where the slope and intercept are used to determine v_m and then the BET specific surface area, S_{BET} :

$$S_{\text{BET}} = \frac{v_m \cdot N \cdot s}{V \cdot m} \quad \left[\frac{\text{m}^2}{\text{g}}\right] \quad (4.4)$$

where, N Avogadro's number [mol^{-1}], s the adsorption cross section of the adsorbing species [m^2], V molar volume of nitrogen [m^3/mol] and m the adsorbent mass [g].

Pore volume and pore size

The Horváth-Kawazoe method corrected with the cylinder pore geometry (Saito-Foley) has been used to calculate pore volume and pore width.

Horváth-Kawazoe (HK) model is a widely used method for determining pore-size distribution in microporous materials from a single adsorption isotherm. This technique utilizes adsorption isotherm data at a temperature below or equal to the critical temperature of the adsorbate, which is nitrogen at 77 K.

By assuming micropore filling and equating the free energy change upon adsorption to the average interaction energy of the adsorbing molecules, the “step” in the isotherm data is translated into a PSD (pore size distribution). The mathematical expression relating relative pressure of the adsorbing gas to the pore size of the adsorbent arises from the combination of the following two equations:

$$RT \ln\left(\frac{p}{p_0}\right) + RT\left[1 + \frac{1}{\theta} \ln(1 - \theta)\right] = N_{Av} \cdot \epsilon_{ave} \quad (4.5)$$

$$\epsilon(r) = \frac{5}{2} \pi \epsilon^* \left[\frac{21}{32} \left(\frac{d_0}{L}\right)^{10} \sum_{k=0}^{\infty} \alpha_k \left(\frac{r}{L}\right)^{2k} - \left(\frac{d_0}{L}\right)^4 \sum_{k=0}^{\infty} \beta_k \left(\frac{r}{L}\right)^{2k} \right] \quad (4.6)$$

The model is based on the assumption that adsorption will proceed from the extreme periphery of the pore towards the center, through consecutive cylindrical monolayers of adsorbate molecules, as shown in Fig. 4.5.

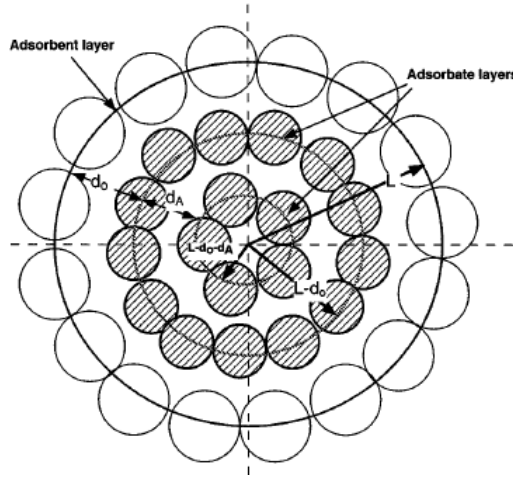


Figure 4.5. Cross-sectional view of the configuration of adsorbate molecules in a cylindrical pore of radius L . [52].

In equation 4.5 the free energy change upon adsorption, $RT \ln\left(\frac{p}{p_0}\right)$, is equated to the molar average interaction energy $N_{Av} \cdot \epsilon_{ave}$. Equation 4.6 relates the interaction energy of a gas molecule in a cylindrical pore to the radius of the pore, L .

An algorithm, solving equations 4.5 and 4.6 in an iterative way, calculates the maximum pore volume [cm^3/g] and the median pore width [nm].

4.2.3 TG-DSC analysis

Devices description

Thermal analysis is a group of techniques in which a physical property of a substance is measured as a function of temperature or time while the substance is subjected to a temperature-controlled programme.

STA, *Simultaneous Thermal Analysis*, is a thermoanalytical method resulting from the combination of TGA, *Thermogravimetric Analysis*, and DSC, *Differential Scanning Calorimetry* techniques.

TGA is a technique in which the mass of a substance is measured as a function of temperature or time, while the substance is subjected to a temperature-controlled program in a specified atmosphere.

DSC is a technique in which the heat flow difference between a substance and a reference material is measured as a function of temperature or time, while the substance and the reference material are subjected to a controlled-temperature program.

Thus, STA measures both, heat flow and weight change of a sample as a function of temperature or time under controlled atmosphere. Simultaneous measurement of these two material properties simplifies interpretation of the results, since it allows differentiation between endothermic and exothermic events which have no associated weight change (e.g. melting and crystallization) and those which involve a weight change (e.g., adsorption, desorption). Also more important, it allows to refer all the peak areas (i.e. enthalpy of transformation J/g) to the sample mass at any temperature during the measurement rather than to the initial sample mass, thus giving back the correct enthalpy as consecutive mass losses occur.

Moreover it allows to have surely the same measurement conditions for both TGA and DSC analyses in a shorter time.

In this thermal characterization, since adsorption/desorption processes take place, SETARAM SENSYS evo TG-DSC analyzer has been coupled with SETARAM WETSYS controlled humidity generator, shown in Fig. 4.6 and 4.7.

SENSYS evo TG-DSC is composed by:

- a symmetrical microbalance, an extremely sensitive instrument, able to measure actual variations in weight with a precision of about 0.001 mg, which gives the weight change of the sample (Δm [%]) during all the measurements;
- the sample and the reference quartz crucibles, both totally surrounded by Calvet 3D sensors, composed of 120 thermocouples mounted in a cylinder and able to measure with a precision of about 0.01 K, allowing to detect up to 94 % of all heat exchanged between the sample/reference and the calorimetric block;
- the calorimetric block, which contains the furnace that provides the heat flux and that is further water cooled to eliminate any environmental variations.

The sample and the reference are kept at the same temperature while the heat flow changes according to their specific heat. The thermocouples measure the temperature difference between the sample and the reference, giving as output a differential signal. Exothermic and endothermic effects can be seen as peaks: the area of those peaks gives the amount of enthalpy and the direction of the peaks indicates the way of heat flux.

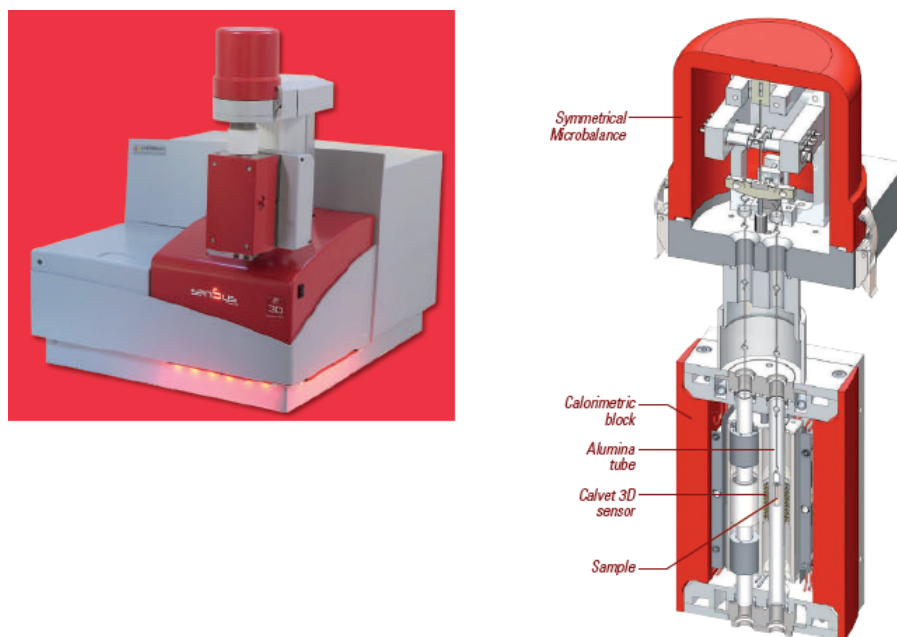


Figure 4.6. SETARAM SETSYS evo TG-DSC analyzer (left) and its internal composition (right).

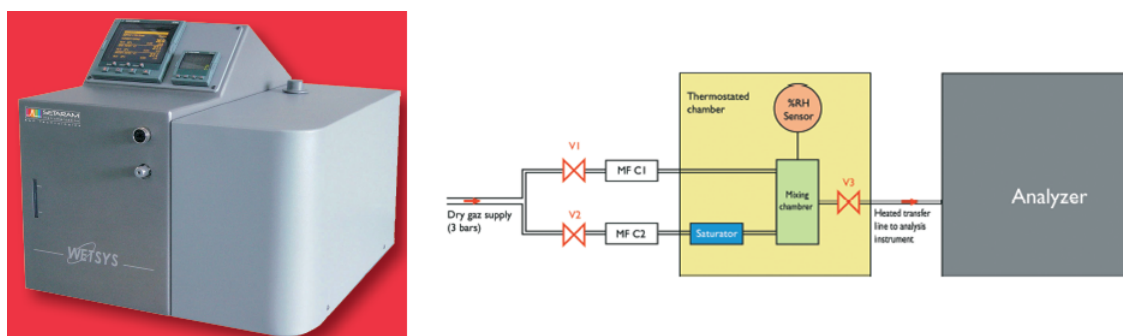


Figure 4.7. SETARAM WETSYS controlled humidity generator (left) and its schematic working principle (right).

WETSYS controlled humidity generator is a stand alone system designed to generate atmospheres with a controlled humidity level. It is based on the simple principle of mixing dry and humid gases (e.g., air, He, Ar, N₂, CO₂). In our case, N₂ gas has been used. The gas circuit, shown in Fig. 4.7, (dry gas at the inlet) is divided into two parts, both regulated by an electrovalve and a mass flow controller: one that carries dry gas and another that carries the saturated gas, making it go through a saturator. These two circuits end in a thermostated mixing chamber, linked to a humidity probe, able to measure relative humidity with a precision of about 0.03 %. Then a heated, temperature regulated transfer line brings the humid gas to the analysis instrument (i.e. SENSYS evo TG-DSC), by avoiding condensation phenomena on cold points between the WETSYS

and the connected instrument.

Finally, a user-friendly interface allows to program varied and complex humidity profiles, by setting gas temperature, water temperature (so relative humidity) and timing.

Set-up of the tests

The aim of thermal analysis was to determine for each material:

- the cycling loading lift;
- the heat of adsorption;
- the energy storage capacity.

That was possible carrying out TGA-DSC analysis, under open thermal energy system operating conditions: the temperature and the partial vapour pressure patterns are shown schematically in Fig. 4.8 and Table 4.4.

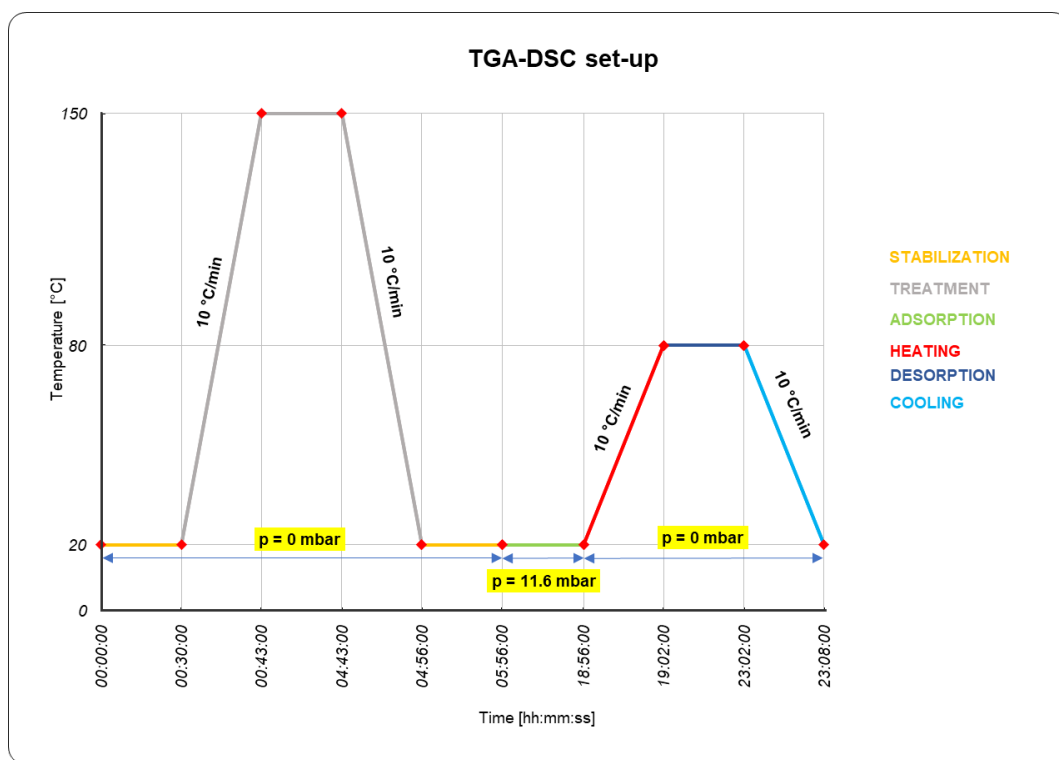


Figure 4.8. Schematic temperature pattern (pressure specification) - TGA/DSC tests.

The steps implemented to perform each test have been the following.

CALIBRATION OF EMPTY CRUCIBLES It was done in order to avoid possible oscillations caused by electrostatic effects on quartz crucibles that, even if slow, may cause noise in measurement of the sample mass, due to high sensitivity of the micro balance; then, the initial sample mass was recorded.

FIRST STABILIZATION A first thirty-minutes stabilization step (20 °C, 0 mbar) was carried out to reach temperature and pressure equilibrium in the calorimetric block containing the sample.

TREATMENT Then, the so called *activation* step was performed, which consisted in the dehydration of the sorbent by heating it up to 150 °C (rate 10 °C/min) and keeping constant that temperature for four hours, then cooling it down (at the same rate) to 20 °C; in this way the sample was ready for adsorption since it was completely dried; first stabilization and treatment were implemented only at the beginning of each test and not before each adsorption/desorption cycle.

SECOND STABILIZATION Since transient steps, such as heating and cooling, do not seem to be instantaneous (little span between the time set to cool down and the effective cooling of the material), an hour of temperature stabilization (constant at 20 °C) was carried out to ensure that adsorption starts at the desired operating conditions; it was found that one hour was sufficient to reach thermal equilibrium.

ADSORPTION Therefore, adsorption was performed at open system boundary conditions, i.e. temperature of 20 °C and partial vapour pressure of 11.6 mbar, which correspond to 50 % of relative humidity; it lasted until saturation was reached, in our case after thirteen hours.

DESORPTION After heating the sample (at the same rate) up to 80 °C, since a low temperature TES is desirable, desorption was completed after four hours with dry N₂ flow and then the sorbent was cooled down again to 20 °C to be ready for the next adsorption step (in case of cyclability analysis).

	TREND	T [°C]	p [mbar]	RATE [°C/min]	DURATION [hh:mm:ss]
STABILIZATION	constant	20	0	-	00:30:00
TREATMENT	heating	-	0	10	00:13:00
	cooling	-	0	10	00:13:00
STABILIZATION	constant	20	0	-	01:00:00
ADSORPTION	constant	20	11.6	-	13:00:00
DESORPTION	heating	-	0	10	00:06:00
	constant	80	0	-	04:00:00
	cooling	-	0	10	00:06:00

Table 4.4. TGA-DSC set-up for thermal analysis.

Output and data processing

The output files obtained by the software are graphs and relative Excel data sheets, containing the trend of heat flow [mW], mass [mg] and temperature [°C] of the sample over time [h].

It is important to underline that TGA-DSC tests must be carried out two times: once with the sample and a second time with empty crucibles. Indeed, part of the heat is needed to heat up the quartz crucibles as well as noise in mass and heat flow measurement can be caused by perturbations of the surrounding environment. The empty crucible test allows to quantify them and subtract them from the first results, thus obtaining the correct mass and heat flow values.

The water uptake has been calculated, according to its definition mentioned above, dividing the mass variation, detected by TG analysis, by the anhydrous sample mass, detected after dehydration.

The heat of adsorption has been found integrating the heat flow with respect to time and dividing this value by the adsorbed water mass.

Then, the energy storage capacity, as stated in equation 3.13, is determined multiplying the heat of adsorption by the difference between maximum (adsorption) and minimum (desorption) water uptake.

4.2.4 Hydrothermal stability

Due to the cyclic operational mode of sorption heat transformation applications, sorption materials are subjected to numerous ad/desorption cycles. It is clear that under these conditions, stability is a necessity and crucial aspect and, therefore, has to be investigated separately.

As mentioned in subsection 3.1.3, MIL-125-NH₂ exhibits very high cyclability: less than 1% decrease in exchanged water mass, after 40 adsorption/desorption cycles between 40 and 140 °C and 5.2 kPa partial vapour pressure [42].

Not yet tested hydrothermal stability of the two composites, CaCl₂ and SrBr₂ based.

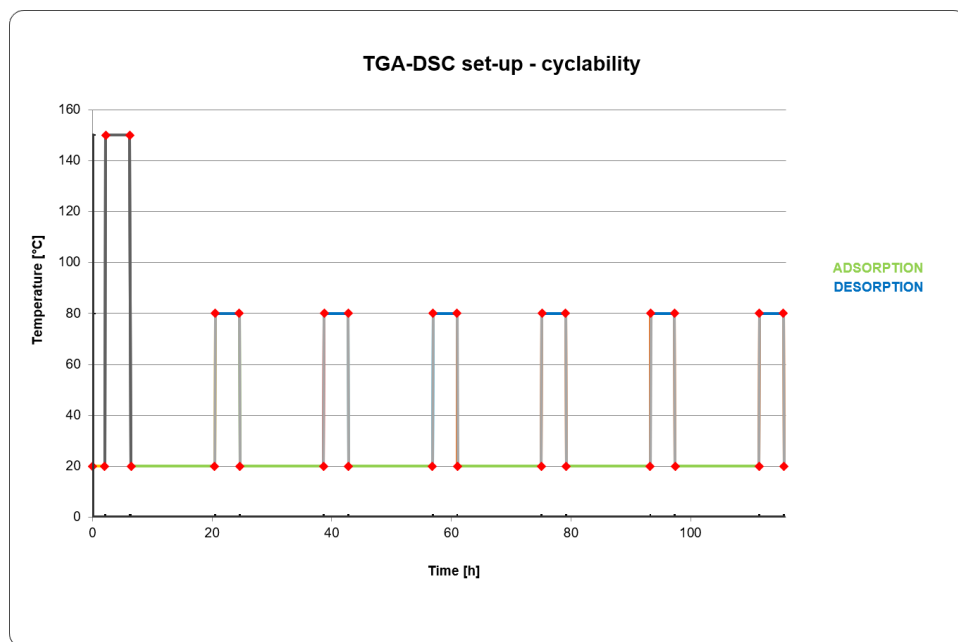


Figure 4.9. Schematic temperature pattern - TGA/DSC cyclability tests.

In this thesis project, cyclability tests were performed for each sample, setting six consecutive adsorption/desorption cycles, after a starting treatment with a view to ensuring complete dehydration of the material, as shown in Fig. 4.9. The boundary conditions of adsorption and desorption tests are the same described in Table 4.4, i.e. $T_{\text{ads}} 20\text{ °C}$, $T_{\text{des}} 80\text{ °C}$, $p_{\text{ads}} 11.6\text{ mbar}$ and $p_{\text{des}} 0\text{ mbar}$.

Once the results were obtained, the percentage of decrease in exchanged water mass between the first and the last cycle have been calculated and also its influence on energy storage capacity.

The results are shown in subsection 5.3.2.

4.2.5 Kinetics

The adsorption kinetics should be considered during comparison between different adsorption pairs. This analysis determines the rate at which the adsorbent material adsorbs/desorbs the refrigerant and it depends on different parameters, such as the affinity between adsorbate and adsorbent, the porosity of the material, the heat transfer properties of the adsorbent, the operating conditions (pressure, temperature) and the mass transfer properties (diffusivity of the adsorbate in the porous material).

The mass transfer resistances are generally categorized into [51]:

1. the mass transfer within the adsorbent granules (intraparticle);
2. the mass transfer through the voids between the granules (interparticles).

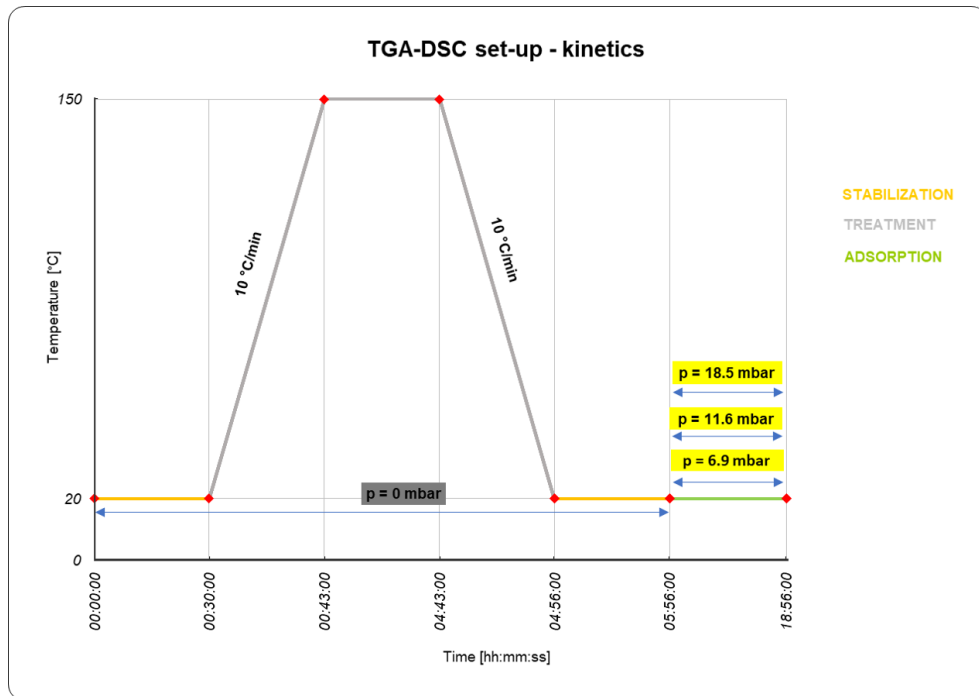


Figure 4.10. Schematic temperature pattern (pressure specification) - TGA/DSC kinetics tests.

The particle size and the shape of the adsorbent particles would significantly affect the diffusion rate of the adsorbate through the adsorbent. For very small particle size of the adsorbent and assuming that water vapour can reach all particles at the same time, the interparticle mass transfer can be neglected and the adsorption/desorption rate by surface diffusion can be modelled using the Linear Driving Force kinetic model (LDF).

Kinetics of adsorption were tested by performing just adsorption each material, keeping constant the temperature ($T_{\text{ads}} = 20^{\circ}\text{C}$), but changing three different partial vapour pressures: 6.9 mbar (30% RH), 11.6 (50% RH) and 18.5 mbar (80% RH), as schematically shown in Fig. 4.10. It was taken a new sample of material at each of the three different pressure conditions, in order to do not taking into account the effect of cyclability but just the influence of pressure on the water uptake.

It should be expected a faster characteristic time to reach the maximum water uptake the more the partial vapour pressure, thus the relative humidity, is increased. Then, it was interesting to compare adsorption kinetics of the three different samples under the same temperature and pressure conditions.

The results are shown in subsection 5.3.3.

Chapter 5

Results and discussion

In this chapter, the results obtained from the tests are shown and commented.

5.1 X-ray diffraction results and discussion

As already mentioned, X-ray powder diffraction is a widely used technique applied to determine the chemical composition of crystalline solids.

The diffraction patterns were obtained for all the synthesized samples and are shown in Annex A. Here, each pristine MOF and its relative composite patterns have been compared with the known patterns of CaCl_2 and SrBr_2 based compounds, in order to find out the actual composition obtained in composites.

5.1.1 (1)MIL-125-NH₂ and CaCl₂-based composite

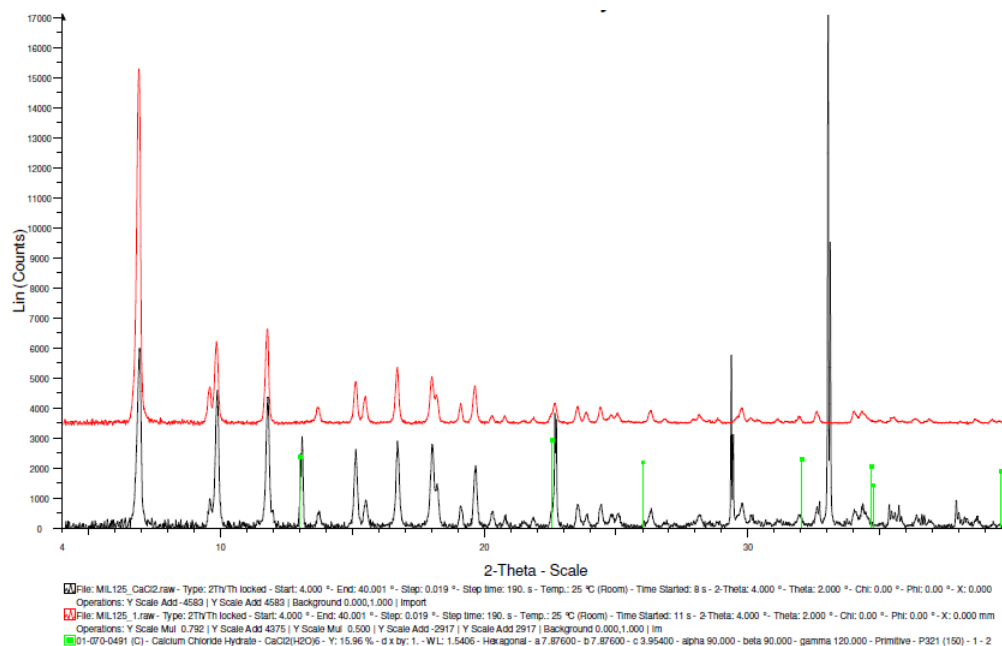


Figure 5.1. XPRD patterns: comparison between MIL-125-NH₂ + (45%)CaCl₂ (black) and MIL-125-NH₂ sample 1 (red); CaCl₂ in green.

Sample 1 MIL-125-NH₂ diffraction pattern (in red) has been compared with MIL-125-NH₂+CaCl₂ composite one (in black). As shown in Fig. 5.1, after scanning all the patterns of CaCl₂-based chemical compounds, the presence of JCPDS 01-070-0491 calcium chloride hexahydrate (CaCl₂(H₂O)₆) has been detected and highlighted (in green) to justify the different peaks obtained in composite with respect to pristine MOF.

5.1.2 (2)MIL-125-NH₂ and SrBr₂-based composite

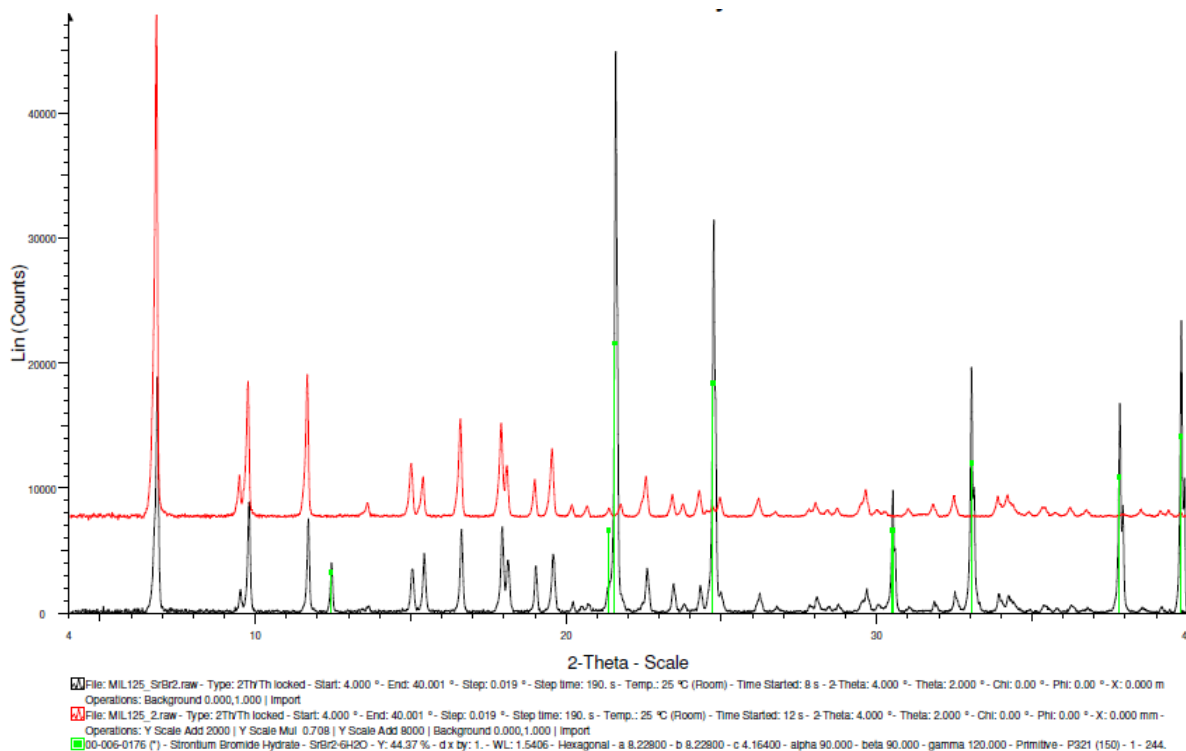


Figure 5.2. XPRD patterns: comparison between MIL-125-NH₂ + (45%)SrBr₂ (black) and MIL-125-NH₂ sample 2 (red); SrBr₂ in green.

Sample 2 MIL-125-NH₂ diffraction pattern (in red) has been compared with MIL-125-NH₂+SrBr₂ composite one (in black). As shown in Fig. 5.2, after scanning all the patterns of SrBr₂-based chemical compounds, the presence of JCPDS 00-006-0176 strontium bromide hexahydrate (SrBr₂(H₂O)₆) has been detected and highlighted (in green) to justify the different peaks obtained in composite with respect to pristine MOF.

5.2 Adsorption isotherms results and discussion

Table 5.1 shows pore volume, pore width and BET specific surface area calculated from experimental nitrogen adsorption isotherms at 77 K, whose graphs are shown below for each sample of material.

LABEL	PORE SIZE [nm]	PORE VOLUME^a [cm ³ /g]	BET SURFACE AREA [m ² /g]
(1)MIL-125(Ti)-NH ₂	1.0243	0.425370	1088.6636 ± 1.9613
(2)MIL-125(Ti)-NH ₂	1.0067	0.505797	1303.1472 ± 2.1256
(1)MIL-125(Ti)-NH ₂ +CaCl ₂	1.4794	0.073801 ^b	196.5245 ± 0.1897
(2)MIL-125(Ti)-NH ₂ +SrBr ₂	1.3944	0.184179	477.4805 ± 0.5757

Table 5.1. Porosimetry values by nitrogen adsorption isotherms at 77 K (^a at a relative pressure 0.175; ^b at a relative pressure 0.150).

Firstly, it can be seen that pore sizes are below the critical diameter 2 nm, thus they are microporous materials, as expected.

Sample 1 of MIL-125-NH₂ shows lower BET surface area of 1089 m²/g, compared with the second sample, 1303 m²/g, and both are lower than the one obtained by Permyakova, 1450 m²/g, even if the same synthesis procedure has been followed for all of them.

Composites show lower specific surface area since the dispersion of salts into the microporous matrix of MOFs reduces the available active surface.

It can be compared BET surface area of MIL-125-NH₂+CaCl₂ composite with the one obtained by Permyakova: also in this case, we obtained lower value, 197 m²/g, compared with 356 m²/g, even if the same synthesis procedure has been followed.

Finally, according to what has been already discussed in subsection 3.2.2 about MOF-based composites, these low residual pore volume and BET surface area found in composites confirm that microporous MOFs as host matrices do not represent the best choice. Indeed, even if a moderate salt content (45% wt.) has been dispersed, it was sufficient to cause a relevant active surface reduction. It can be expected, thus, that this will badly affect desorption kinetics.

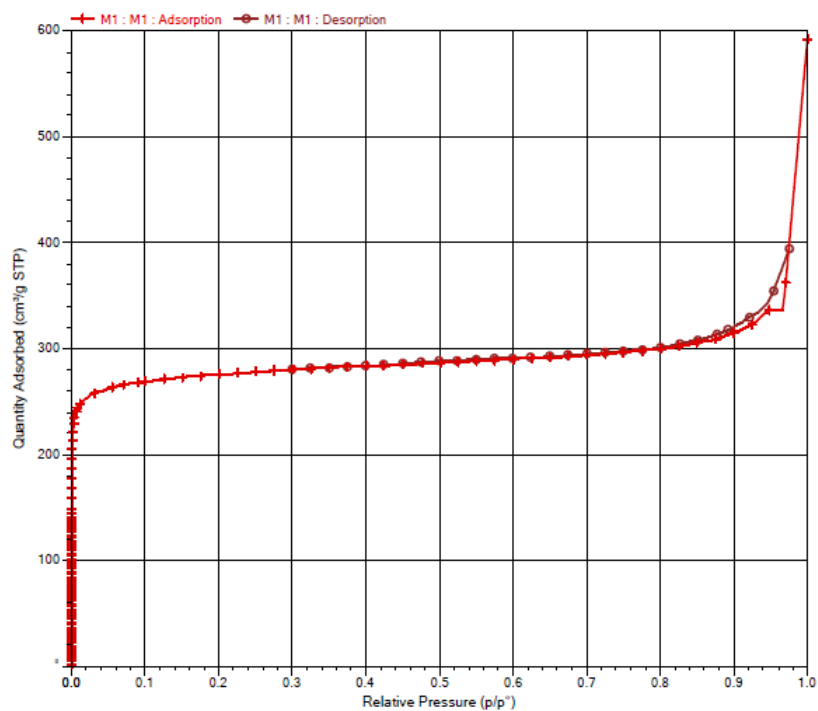


Figure 5.3. Nitrogen adsorption-desorption isotherms of (1)MIL-125-NH₂ at 77 K.

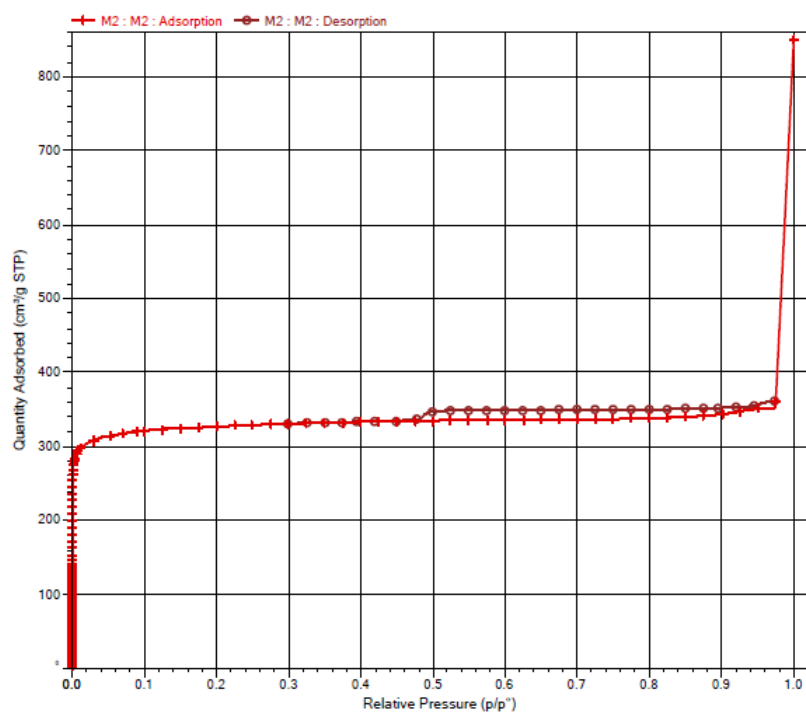


Figure 5.4. Nitrogen adsorption-desorption isotherms of (2)MIL-125-NH₂ at 77 K.

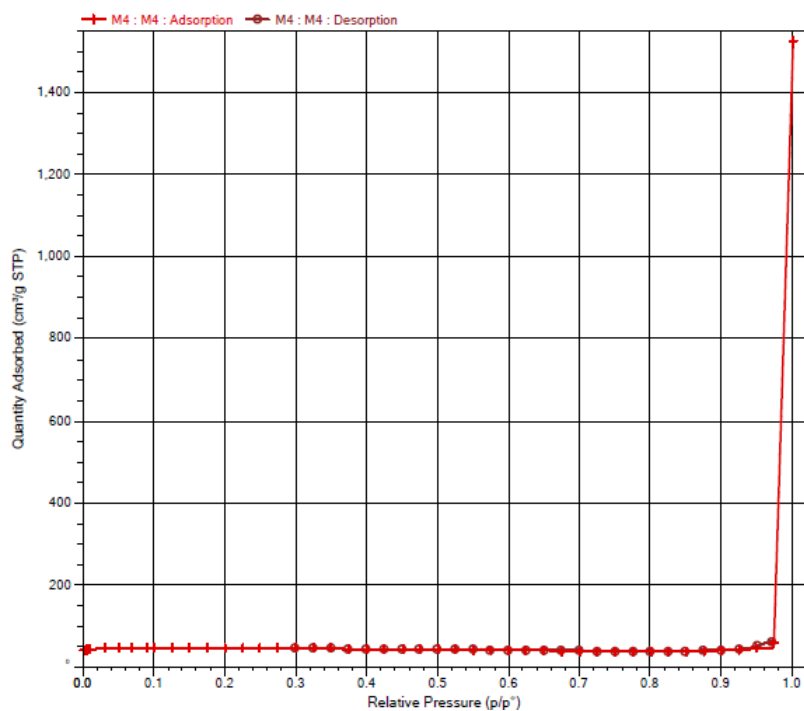


Figure 5.5. Nitrogen adsorption-desorption isotherms of MIL-125-NH₂ + CaCl₂ at 77 K.

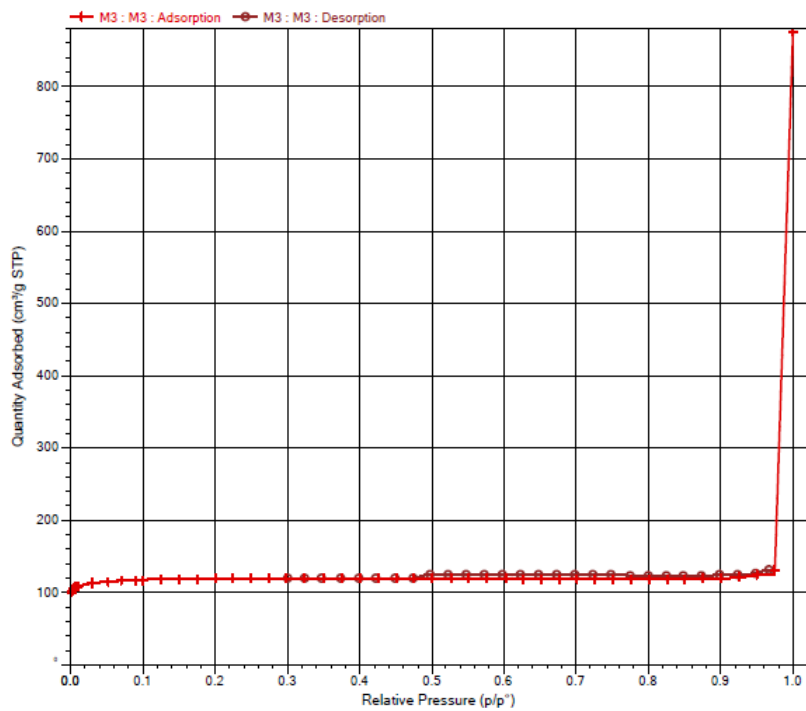


Figure 5.6. Nitrogen adsorption-desorption isotherms of MIL-125-NH₂ + SrBr₂ at 77 K.

5.3 TGA/DSC results and discussion

The results obtained for each sample are the following:

- maximum (saturation) water uptake and cycling loading lift at first adsorption/desorption cycle;
- energy storage capacity, as a result of the integration of heat flux signal over the time, divided by the anhydrous mass of the sample;
- six consecutive adsorption/desorption cycles, performed to obtain the percentage of decrease in water uptake and in energy storage capacity;
- the influence of three different partial vapour pressures (at constant temperature) on the adsorption kinetics of each sample and then, fixing the pressure, a comparison of the adsorption behaviour of the different materials tested.

5.3.1 Water uptake and energy storage capacity

Table 5.2 shows the results of measured maximum water uptake, cycling loading lift and energy storage capacity, after first cycle, for each sample.

REF.	LABEL	T _{ads} [°C]	P _{ads} [mbar]	T _{des} [°C]	P _{des} [mbar]	P/P ₀ [-]	CYCL. LOAD. LIFT ^a x _{cycl} [g/g]	MAX WATER UPTAKE ^a x _{max} [g/g]	HEAT OF ADSORPTION ^a ΔH _{ads} [J/g]	ENERGY STOR. CAPACITY ^a ρ _{Q-m} [Wh/kg]
this work	(1)MIL-125-NH ₂	20	11.6	80	0.14	0.5	0.21	0.21	2784	163
this work	(1)MIL-125-NH ₂ +(45%)CaCl ₂	20	11.6	80	0.14	0.5	0.53	0.56	2309	342
this work	(2)MIL-125-NH ₂ +(45%)SrBr ₂	20	11.6	80	0.14	0.5	0.38	0.40	2980	313

Table 5.2. TG-DSC results - water uptake and energy storage capacity (^a at first cycle).

(1)MIL-125-NH₂

Sample 1 of MIL-125-NH₂ exhibits a saturation water uptake of 0.21 g/g, equal to the cycling loading lift, as can be seen from Fig. 5.7, which is promising for good cyclability properties. It is lower compared to what found by Permyakova [19], (0.39 g/g and 0.37 g/g, maximum water uptake and cycling loading lift, respectively). That could be explained looking at specific surface area values: indeed, our sample shows lower BET surface, 1089 m²/g, compared to 1450 m²/g of Permyakova's sample, thus badly affecting the working capacity of material.

Fig. 5.8 shows the integral of the heat flow signal, which is the heat of adsorption divided by the mass of water adsorbed, i.e. the one detected when adsorption process reaches saturation. Then, multiplying the heat of adsorption by the cycling loading lift, thus applying the energy storage capacity definition, i.e. equation 3.13, it has been found:

$$\begin{aligned}
 \rho_{Q-m} &= \Delta H_{ads} \cdot x_{cycl} \\
 &= 2784 \cdot 0.21 \cdot \frac{10^3}{3600} \\
 &= 163 \left[\frac{Wh}{kg} \right]
 \end{aligned} \tag{5.1}$$

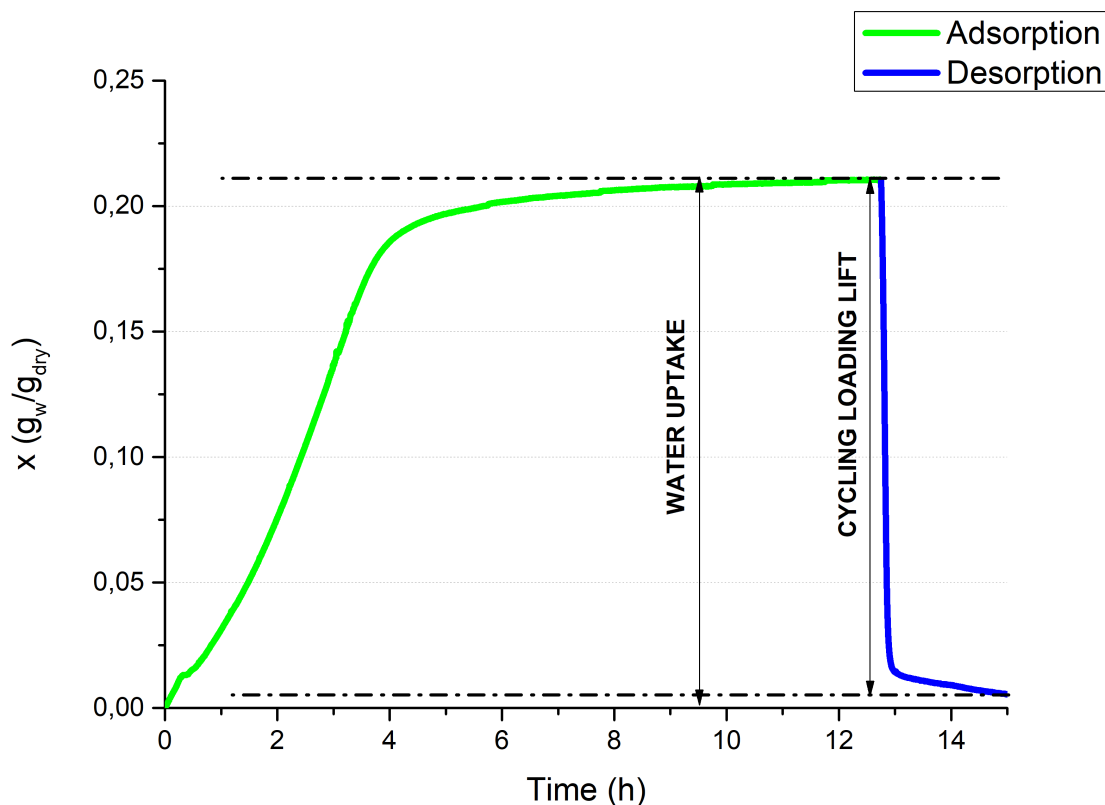


Figure 5.7. (1)MIL-125-NH₂ first adsorption/desorption cycle: $T_{\text{ads}}=20\text{ }^{\circ}\text{C}$, $p/p_0=0.5$, $T_{\text{des}}=80\text{ }^{\circ}\text{C}$, $p/p_0=0.0003$.

Energy storage capacity of MIL-125-NH₂ reaches the value of 586 J/g or 163 Wh/kg, which, as could be expected, results half than 322 Wh/kg found by Permyakova (see Table 2.4), since for almost half is also the maximum water uptake of our sample.

It can be concluded, then, that the specific surface area, that can be different even following the same synthesis procedure, can highly affect MOFs performances. By the way, even if our sample would have shown the same BET surface of the Permyakova's one, the testing conditions chosen (typical open reactor conditions, i.e. adsorption temperature and relative humidity of 20 °C and 50%, respectively, and desorption temperature and relative humidity of 80 °C and 0.03%, respectively) would have not led to relevant increase in water uptake and energy storage density, since the highest amount of water exchange occurs at the relative pressure range 0.1 ÷ 0.3.

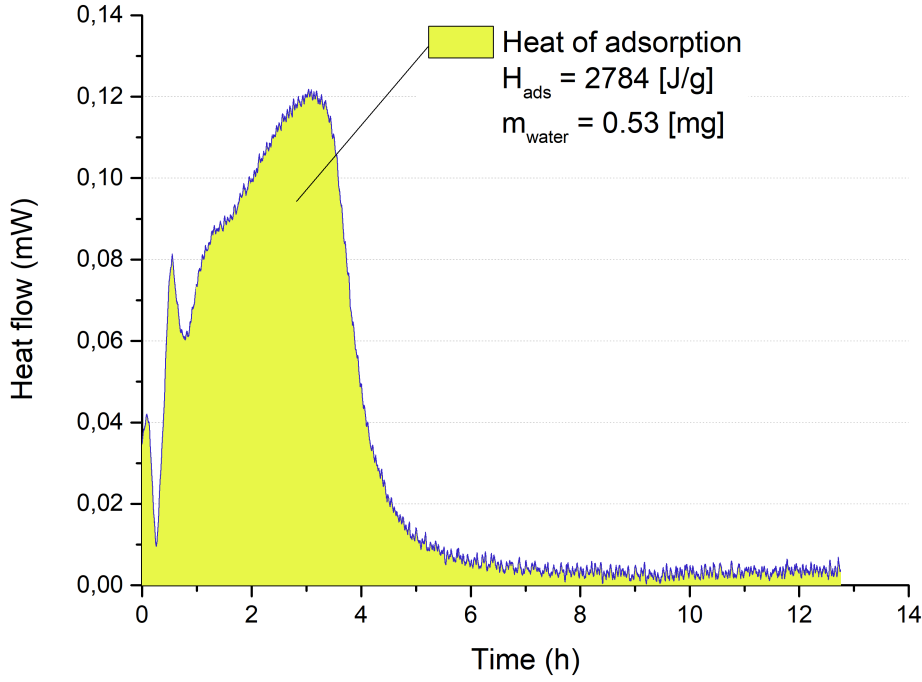


Figure 5.8. (1)MIL-125-NH₂ heat of adsorption at first cycle.

MIL-125-NH₂ + CaCl₂

As shown in Fig. 5.9, composite MIL-125-NH₂ + CaCl₂ exhibits a saturation water uptake of 0.56 g/g and a cycling loading lift of 0.53 g/g. A significant improvement in water uptake is evidenced upon salt dispersion: 0.56 g/g *versus* 0.21 g/g for the pure MOF. This was expected, since the presence of inorganic salt enhances the hydrophilic behavior of our adsorbent material.

Fig. 5.10 shows the integral of the heat flow signal, which is the heat of adsorption divided by the mass of water adsorbed, i.e. the one detected when adsorption process reaches saturation. Then, multiplying the heat of adsorption by the cycling loading lift, thus applying the energy storage capacity definition, i.e. equation 3.13, it has been found:

$$\begin{aligned}
 \rho_{Q-m} &= \Delta H_{\text{ads}} \cdot x_{\text{cycl}} \\
 &= 2309 \cdot 0.53 \cdot \frac{10^3}{3600} \\
 &= 342 \left[\frac{\text{Wh}}{\text{kg}} \right]
 \end{aligned} \tag{5.2}$$

Energy storage capacity of MIL-125-NH₂+CaCl₂ reaches the value of 1231 J/g or 342 Wh/kg, which almost doubles the value of pristine MIL-125-NH₂. The contribution of the salt higher heat of adsorption released, due to the chemical reaction involved, coupled with faster kinetics of physisorption, leads to outstanding energy storage capacity at low desorption temperature of 80 °C.

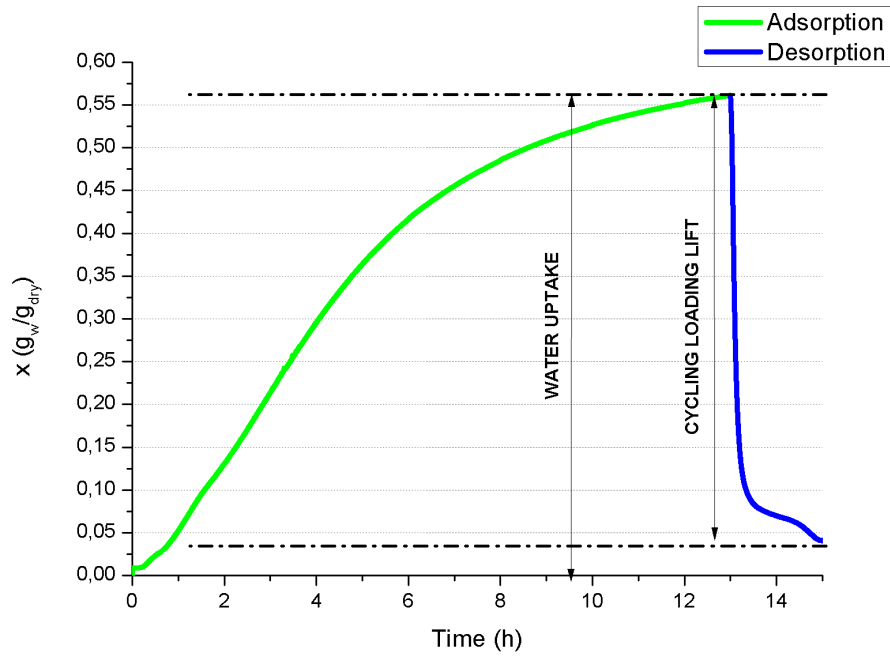


Figure 5.9. MIL-125-NH₂ + CaCl₂ first adsorption/desorption cycle: $T_{\text{ads}}=20$ °C, $p/p_0=0.5$, $T_{\text{des}}=80$ °C, $p/p_0=0.0003$.

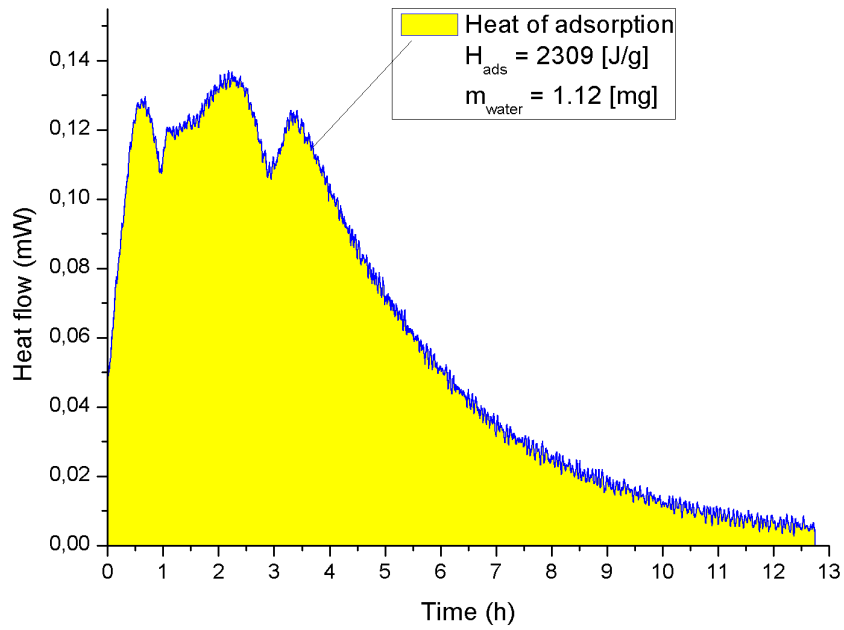


Figure 5.10. MIL-125-NH₂ + CaCl₂ heat of adsorption at first cycle.

Moreover, unexpectedly, higher water uptake and energy storage capacity, 0.56 g/g and 342 Wh/kg, than the ones found in literature, by Permyakova, 0.46 g/g and 243 Wh/kg, even if a lower BET surface has been measured for our sample. It should be verified the exact percentage of salt dispersed in the MOF matrix, which could be higher than 45%, thus justifying these enhanced values.

MIL-125-NH₂ + SrBr₂

Composite MIL-125-NH₂+SrBr₂ exhibits a saturation water uptake of 0.40 g/g and a cycling loading lift of 0.38 g/g, as can be seen in Fig. 5.11. A significant improvement in water uptake is evidenced upon salt dispersion: 0.40 g/g *versus* 0.21 g/g for the pure MOF. As already mentioned, this was expected, since the presence of inorganic salt enhances the hydrophilic behavior of the adsorbent material.

Fig. 5.12 shows the integral of the heat flow signal, which is the heat of adsorption divided by the mass of water adsorbed, i.e. the one detected when adsorption process reaches saturation. Then, multiplying the heat of adsorption by the cycling loading lift, thus applying the energy storage capacity definition, i.e. equation 3.13, it has been found:

$$\begin{aligned}
 \rho_{Q-m} &= \Delta H_{\text{ads}} \cdot x_{\text{cycl}} \\
 &= 2980 \cdot 0.38 \cdot \frac{10^3}{3600} \\
 &= 313 \left[\frac{\text{Wh}}{\text{kg}} \right]
 \end{aligned} \tag{5.3}$$

Energy storage capacity of MIL-125-NH₂+SrBr₂ reaches the value of 1127 J/g or 313 Wh/kg, which almost doubles the value of pristine MIL-125-NH₂. The contribution of the salt higher heat of adsorption released, due to the chemical reaction involved, coupled with faster kinetics of physisorption, leads to an enhancing effect on energy storage capacity at low desorption temperature of 80 °C.

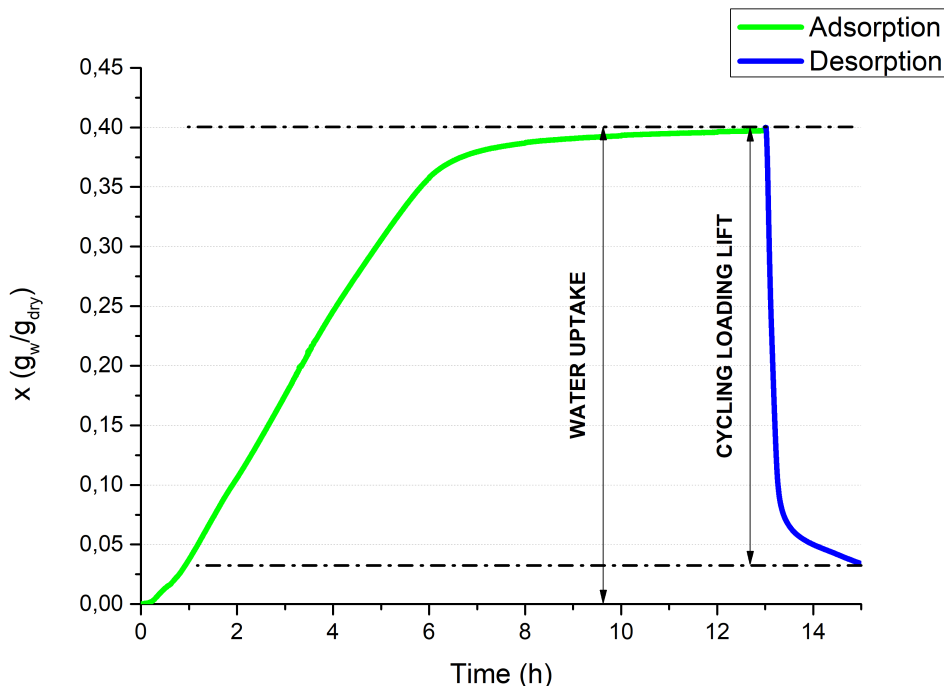


Figure 5.11. MIL-125-NH₂ + SrBr₂ first adsorption/desorption cycle: $T_{\text{ads}}=20\text{ }^{\circ}\text{C}$, $p/p_0=0.5$, $T_{\text{des}}=80\text{ }^{\circ}\text{C}$, $p/p_0=0.0003$.

5.3.2 Hydrothermal stability

Table 5.3 shows how maximum water uptake, cycling loading lift and energy storage capacity are affected after six consecutive adsorption/desorption cycles.

REF.	LABEL	CYCL. LOAD. LIFT ^a	MAX WATER UPTAKE ^a	HEAT OF ADSORPTION ^a	ENERGY STOR. CAPACITY ^a	DECREASE WAT. UP. ^a
		x_{cycl} [g/g]	x_{max} [g/g]	ΔH_{ads} [J/g]	ρ_{Q-m} [Wh/kg]	[%]
this work	(1)MIL-125-NH ₂	0.20	0.20	2577	144	5
this work	(1)MIL-125-NH ₂ +(45%)CaCl ₂	0.53	0.56	2095	310	0.03
this work	(2)MIL-125-NH ₂ +(45%)SrBr ₂	0.38	0.39	2757	287	1

Table 5.3. TG-DSC results - hydrothermal stability (^a after six cycles).

(1)MIL-125-NH₂

Expectations of very high hydrothermal stability of MIL-125-NH₂, already proved in literature, have been satisfied after six consecutive cycles, upon typical open systems operating conditions. Indeed, the calculated percentage of decrease in water uptake between the first and the sixth cycle is about 5 %, as can be appreciate also from Fig. 5.13.

The rationality in considering this percentage a good value lies in the slight decrement observed in energy storage capacity, upon cycling, from 163 to 144 Wh/kg, as shown in Fig. 5.14.

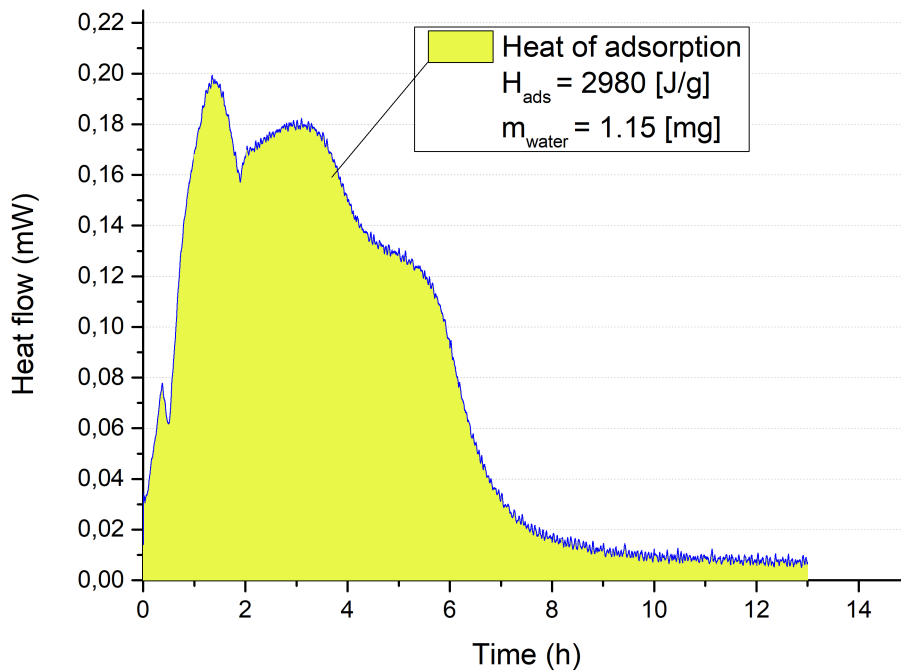


Figure 5.12. MIL-125-NH₂ + SrBr₂ heat of adsorption at first cycle.

MIL-125-NH₂ + CaCl₂

Composite MIL-125-NH₂ + CaCl₂ shows very high hydrothermal stability, keeping the same cycling loading lift, 0.53 g/g, after six consecutive adsorption/desorption cycles. Moreover, the calculated percentage of decrease in water uptake between the first and the sixth cycle is about 0.03 %, as can be appreciate also from Fig. 5.15.

The rationality in considering this percentage a good value lies in the slight decrement observed in energy storage capacity, upon cycling, from 342 to 310 Wh/kg, as shown in Fig. 5.16.

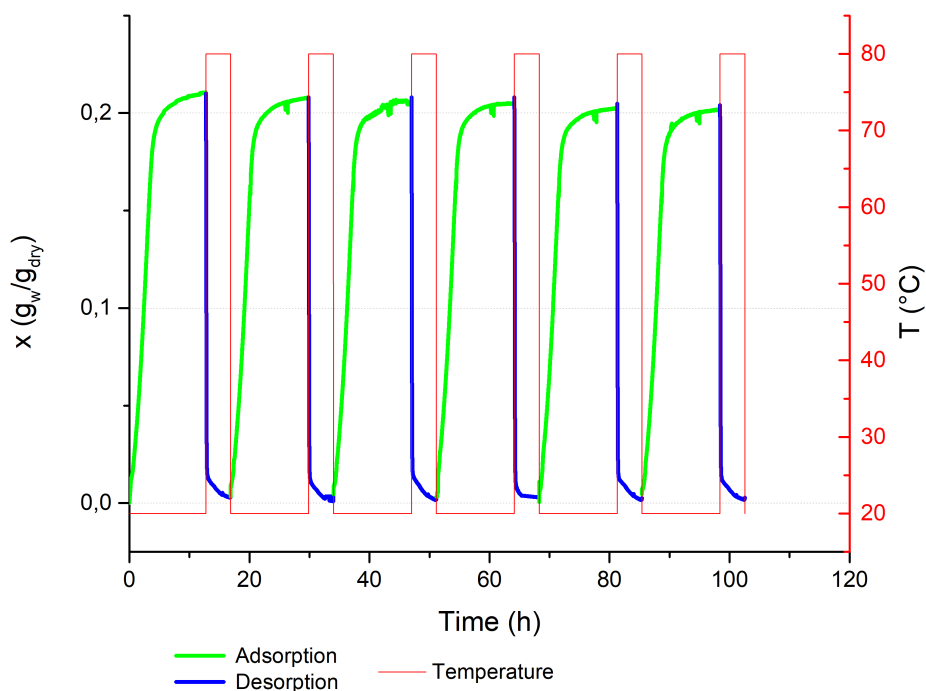


Figure 5.13. (1)MIL-125-NH₂ cyclability test upon six adsorption/desorption cycles with T_{ads} 20 °C, $p/p_0=0.5$, T_{des} 80 °C, $p/p_0=0.0003$.

MIL-125-NH₂ + SrBr₂

Composite MIL-125-NH₂ + SrBr₂ shows very high hydrothermal stability, keeping the same cycling loading lift, 0.38 g/g, after six consecutive adsorption/desorption cycles. Moreover, the calculated percentage of decrease in water uptake between the first and the sixth cycle is about 1 %, as can be appreciate also from Fig. 5.17.

The rationality in considering this percentage a good value lies in the slight decrement observed in energy storage capacity, upon cycling, from 313 to 287 Wh/kg, as shown in Fig. 5.18.

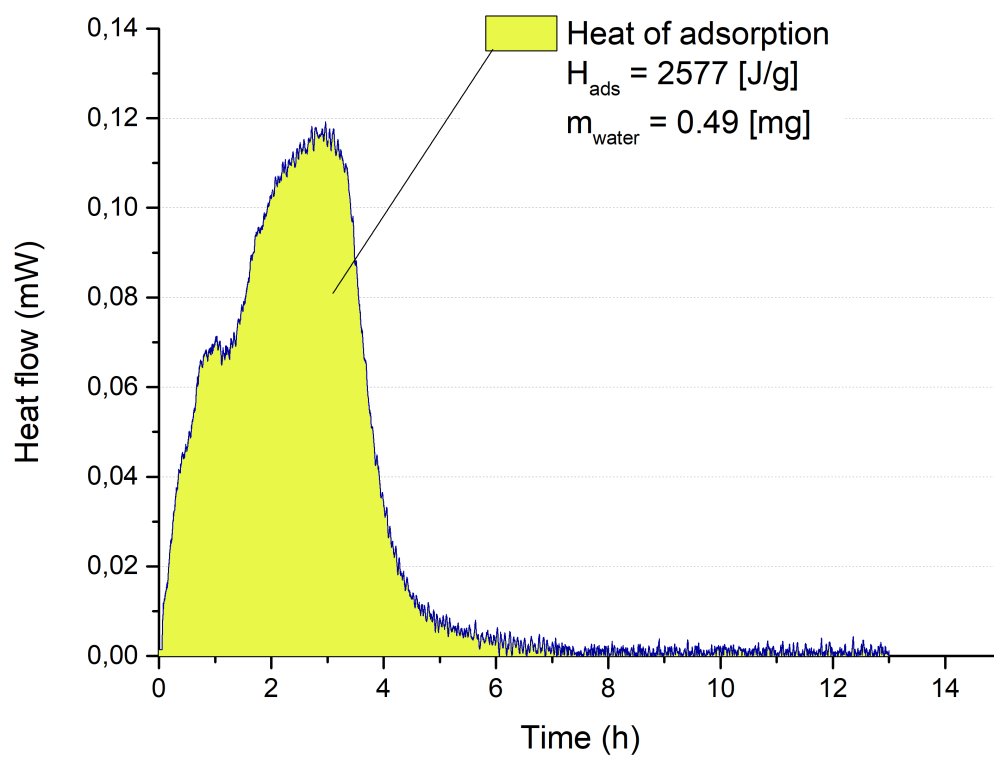


Figure 5.14. (1)MIL-125-NH₂ heat of adsorption after six consecutive adsorption/desorption cycles.

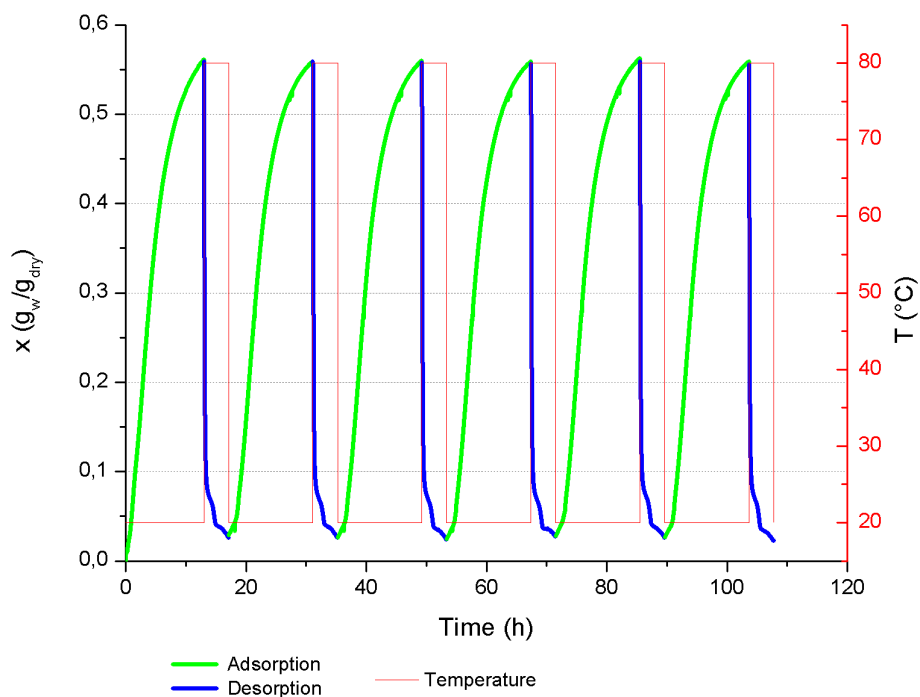


Figure 5.15. MIL-125-NH₂+CaCl₂ cyclability test upon six adsorption/desorption cycles with T_{ads} 20 °C, $p/p_0=0.5$, T_{des} 80 °C, $p/p_0=0.0003$.

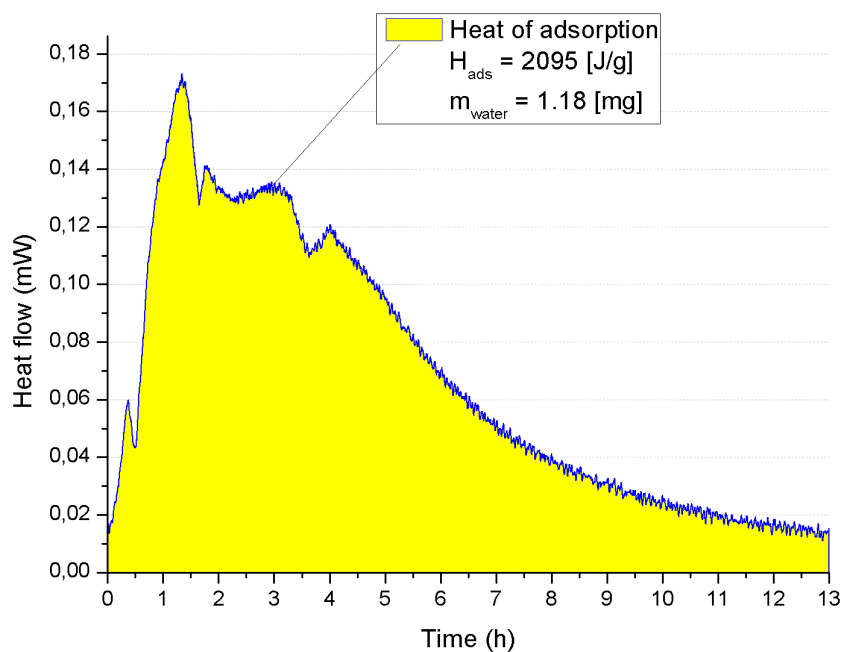


Figure 5.16. MIL-125-NH₂+CaCl₂ heat of adsorption after six consecutive adsorption/desorption cycles.

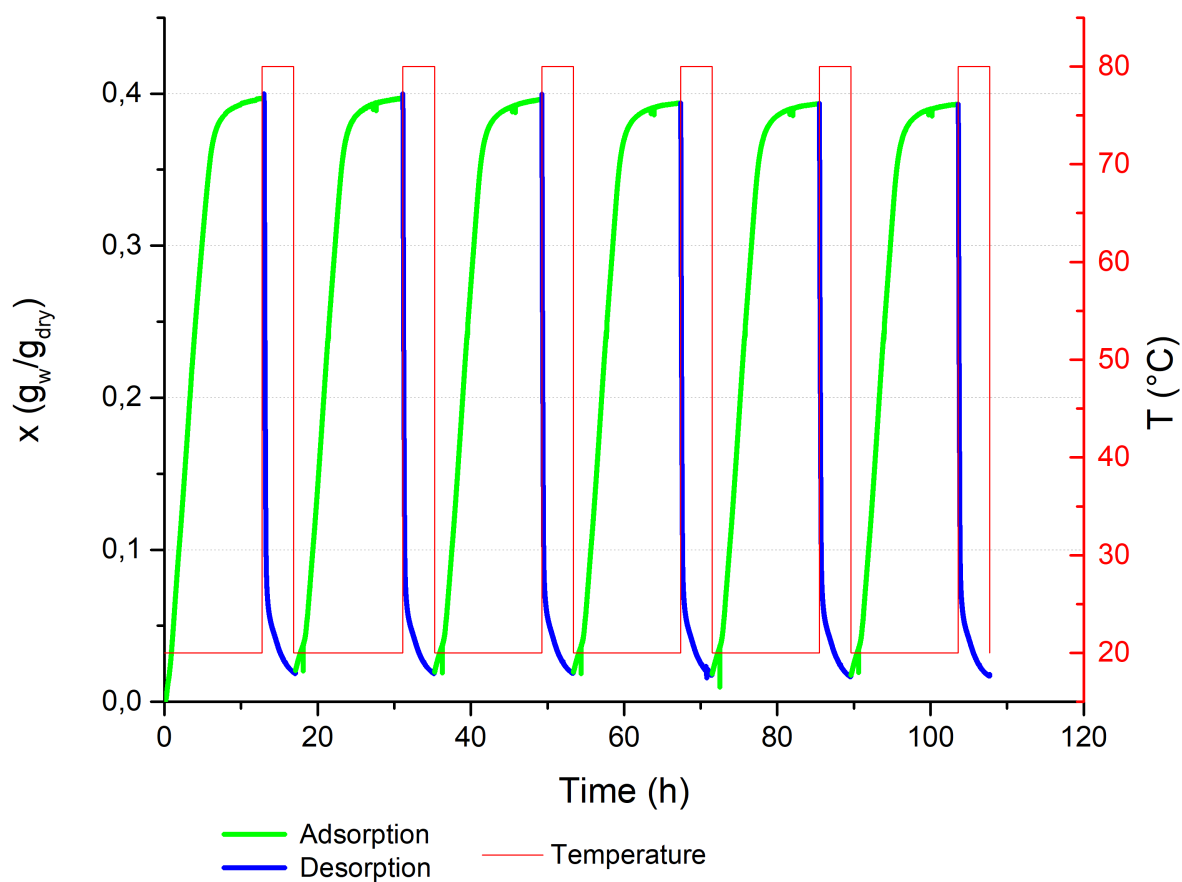


Figure 5.17. MIL-125-NH₂+SrBr₂ cyclability test upon six adsorption/desorption cycles with $T_{\text{ads}} 20\text{ }^{\circ}\text{C}$, $p/p_0=0.5$, $T_{\text{des}} 80\text{ }^{\circ}\text{C}$, $p/p_0=0.0003$.

5.3.3 Adsorption kinetics

(1)MIL-125-NH₂

The comparison of (1)MIL-125-NH₂ adsorption behaviour at three different pressure levels, shown in Fig. 5.19, let us make some comments.

Firstly, it can be seen how the adsorption kinetic becomes faster the farther relative humidity increases from 30% (6.9 mbar), to 50% (11.6 mbar) and finally to 80% (18.5 mbar). After 4 hours, the water uptake during adsorption at 18.5 mbar (0.19 g/g) almost doubles the one detected at 6.9 mbar (0.10 g/g).

Secondly, as expected, it is noticeable that the highest amount of water uptake occurs at partial vapour pressure 6.9 mbar, which corresponds to relative pressure 0.3. Indeed, increasing the pressure, a slight increase in water uptake can be seen for 11.6 mbar and 18.5 mbar curves with respect to 6.9 mbar one.

The phenomenon of water condensation in micropores can be appreciated during adsorption at 18.5 mbar, after almost 5 hours from the start. In Fig. 5.20, the presence of this phenomenon is confirmed by the anomalous heat flow peak corresponding to the saturation plateau of water uptake reached.

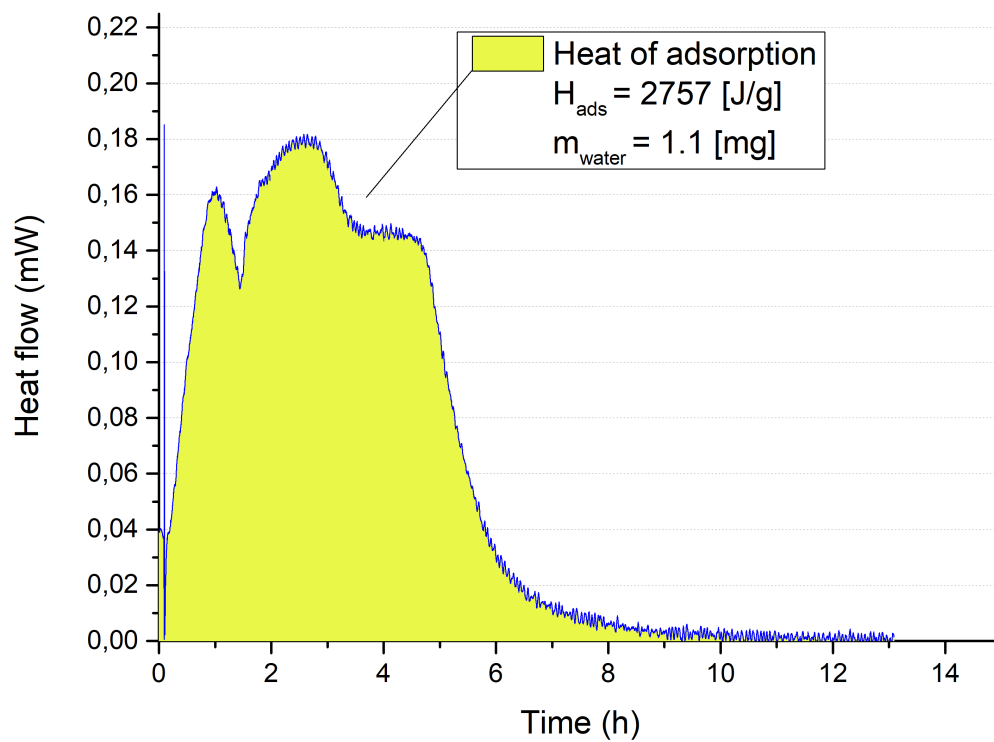


Figure 5.18. MIL-125-NH₂+SrBr₂ heat of adsorption after six consecutive adsorption/desorption cycles.

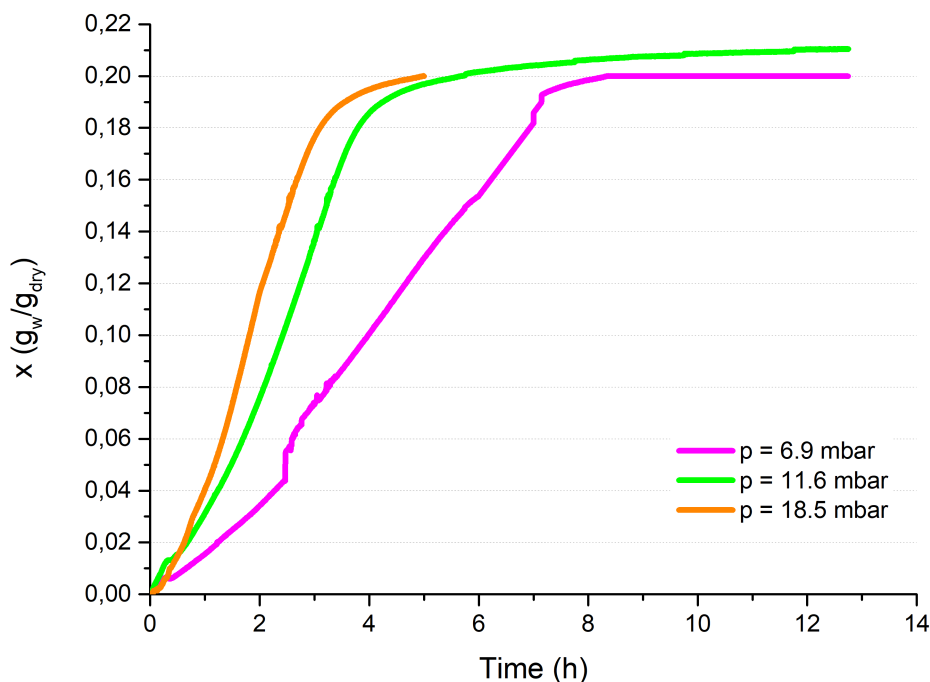


Figure 5.19. (1)MIL-125-NH₂ adsorption kinetics at three different pressure levels ($T_{\text{ads}} = 20\text{ }^{\circ}\text{C}$).

MIL-125-NH₂ + CaCl₂

The comparison of (2)MIL-125-NH₂ + CaCl₂ adsorption behaviour at three different pressure levels is shown in Fig. 5.21.

Firstly, it can be seen how the adsorption kinetic becomes faster the farther relative humidity increases from 30% (6.9 mbar), to 50% (11.6 mbar) and finally to 80% (18.5 mbar). After 4 hours, the water uptake during adsorption at 18.5 mbar (0.40 g/g) more than doubles the one detected at 6.9 mbar (0.17 g/g).

Moreover, it can be seen, also in composites, the presence of water condensation in micropores, after almost six hours. In Fig. 5.22, the presence of this phenomenon is confirmed by the anomalous heat flow peak corresponding to the saturation plateau of water uptake reached.

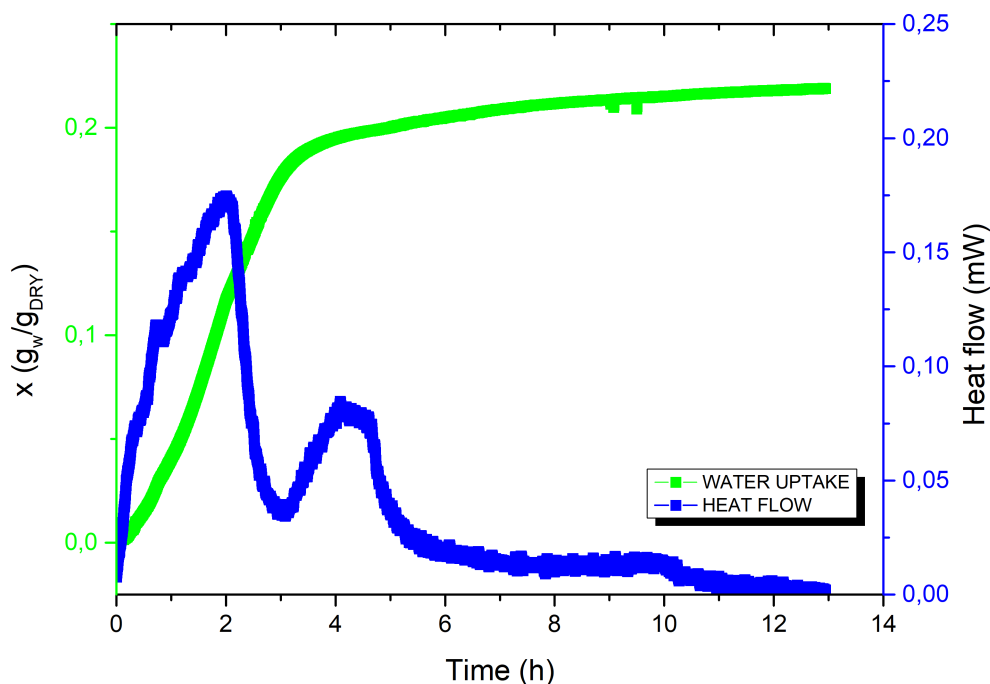


Figure 5.20. (1)MIL-125-NH₂ adsorption at $T_{\text{ads}} = 20\text{ }^{\circ}\text{C}$, $p_{\text{ads}} = 18.5\text{ mbar}$: water condensation in micropores.

MIL-125-NH₂ + SrBr₂

The comparison of (2)MIL-125-NH₂ + SrBr₂ adsorption behaviour at three different pressure levels, shown in Fig. 5.23, let us make some comments.

Firstly, it can be seen how the adsorption kinetic becomes faster the farther relative humidity increases from 30% (6.9 mbar), to 50% (11.6 mbar) and finally to 80% (18.5 mbar). After 4 hours, the water uptake during adsorption at 18.5 mbar (0.35 g/g) more than doubles the one detected at 6.9 mbar (0.15 g/g).

Also in composites, it can be seen the presence of water condensation in micropores, after almost six hours. In Fig. 5.24, the presence of this phenomenon is confirmed by the anomalous heat flow peak corresponding to the saturation plateau of water uptake reached.

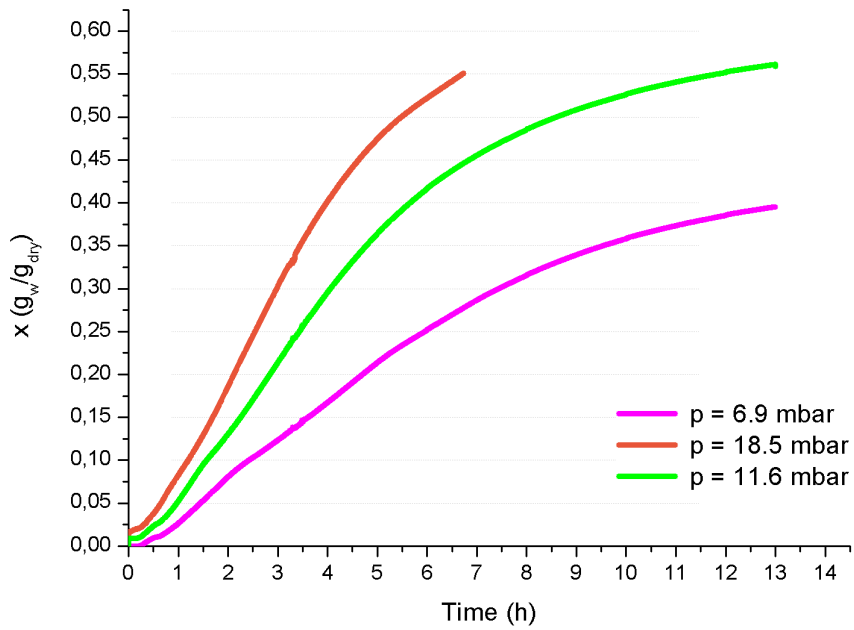


Figure 5.21. MIL-125-NH₂+CaCl₂ adsorption kinetics at three different pressure levels ($T_{\text{ads}} = 20\text{ }^{\circ}\text{C}$).

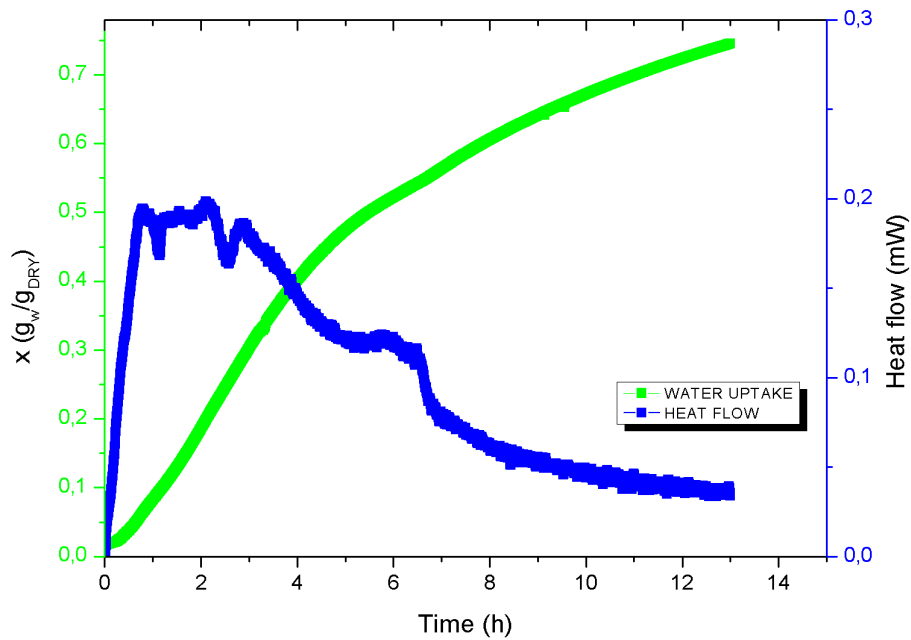


Figure 5.22. MIL-125-NH₂+CaCl₂ adsorption at $T_{\text{ads}} = 20\text{ }^{\circ}\text{C}$, $p_{\text{ads}} = 18.5\text{ mbar}$: water condensation in micropores.

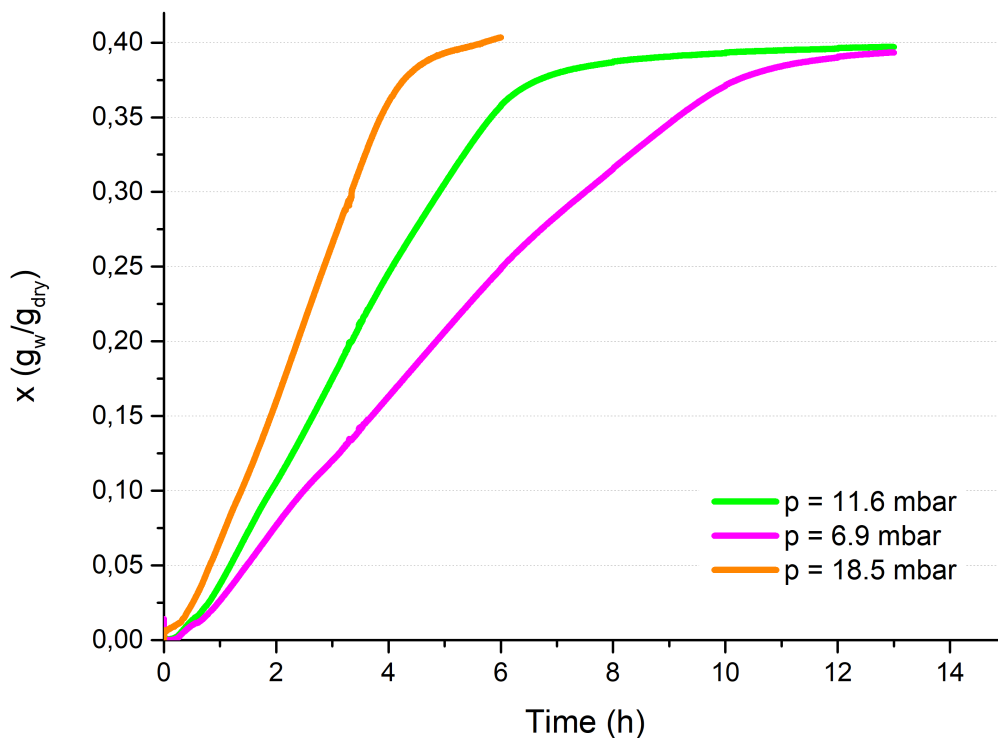


Figure 5.23. MIL-125-NH₂+SrBr₂ adsorption kinetics at three different pressure levels ($T_{\text{ads}} = 20$ °C).

Finally, as expected, due to the presence of inorganic salts, thus chemisorption phenomenon (stronger interactions) involved, the kinetics are slower than in pristine MOF. Indeed, as shown in Fig. 5.25, keeping constant the pressure at 11.6 mbar, after 4 hours, the CaCl₂-based and SrBr₂-based composites reach 53% and 62%, respectively, of their maximum water capacity, compared to the 90% of pristine MIL-125-NH₂. This confirms that the enhanced thermal performances met by composites are at the expense of adsorption kinetics. In particular, we can conclude that SrBr₂-based composite, even if its lower adsorption water uptake and energy storage capacity, outperforms CaCl₂-based one from the kinetics point of view, thanks to its higher residual pore volume.

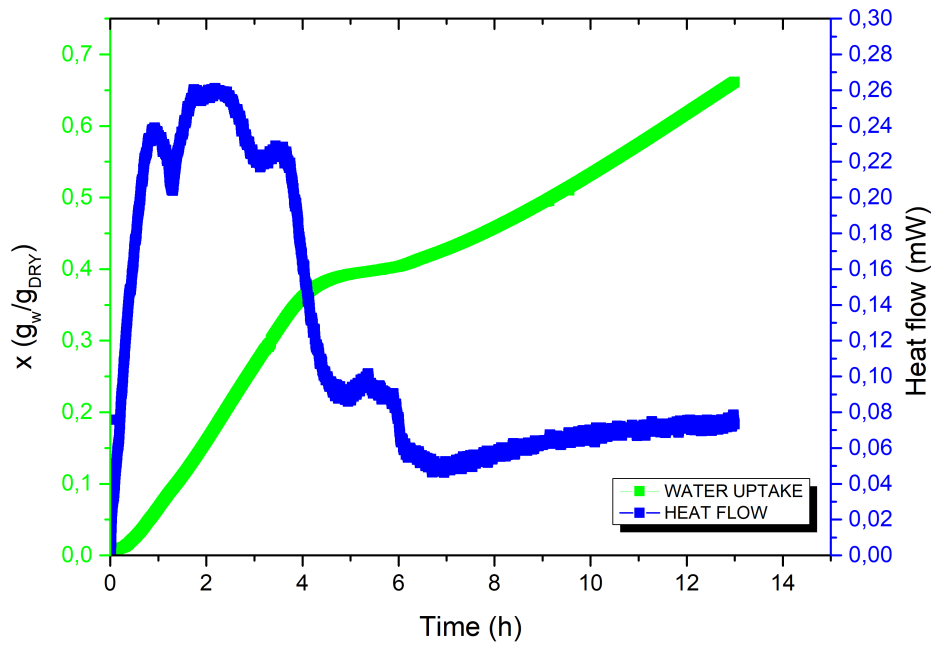


Figure 5.24. MIL-125-NH₂+SrBr₂ adsorption at $T_{\text{ads}} = 20\text{ }^{\circ}\text{C}$, $p_{\text{ads}} = 18.5\text{ mbar}$: water condensation in micropores.

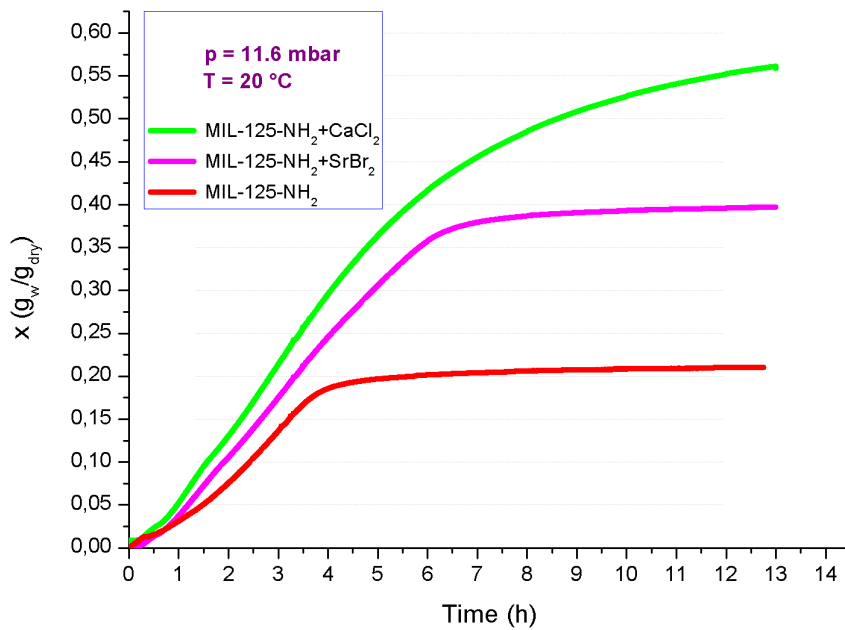


Figure 5.25. Adsorption kinetics comparison between all the samples: $T_{\text{ads}} = 20\text{ }^{\circ}\text{C}$, $p_{\text{ads}} = 11.6\text{ mbar}$.

Conclusions and future work

The growing importance of integrating thermal energy storage in heating and cooling systems of buildings, in order to decrease the energy needs and improve the efficiency of green intermittent energy sources, led to invest resources in developing more and more suitable storage media.

Focusing the attention on sorption heat storage, among a large number of porous materials, Metal-organic frameworks (MOFs) have been considered of particular interest, thanks to their tunable adsorption properties and quite high energy densities, despite of low regeneration temperatures.

Among a series of water stable MOFs, a first exploitation of three different ones, pristine MIL-125-NH₂, MIL-125-NH₂ + (45%)CaCl₂ and MIL-125-NH₂ + (45%)SrBr₂ composites, has been carried out in order to test their thermal performances for thermal energy storage.

After synthesis, it was performed X-ray powder diffraction to verify their actual chemical composition, nitrogen adsorption isotherms to assess pore volume, pore size and specific surface area. Then, TG-DSC tests, i.e. simultaneous thermogravimetric and differential scanning calorimetric tests, under typical open systems boundary conditions (T_{des} 80 °C, p_{des} almost 0 mbar, T_{ads} 20 °C, p_{ads} 11.6 mbar), to both calculate the energy storage capacity and perform hydrothermal stability and kinetics analyses.

Thus, we can draw conclusions about thermal performances, by comparing the results of the three tested samples, also with literature data, if available.

Pristine MIL-125-NH₂ results let us observe that:

1. lower BET surface, compared to literature data, leads to lower water uptake and energy storage capacity, 0.21 g/g and 163 Wh/kg, respectively, being also the lowest among the three samples;
2. about 5% of decrease in water uptake after six cycles proves high hydrothermal stability of the material, resulting in a slight decrement in energy storage capacity, from 163 to 144 Wh/kg;
3. as expected, for all the samples, adsorption kinetics become faster the farther relative humidity increases from 30%, to 50% and finally to 80%.

Composite MIL-125-NH₂ + CaCl₂ results let us observe that:

1. the expected lower BET surface and residual pore volume, due to salt dispersion in pure MOF matrix, are compensated by the beneficial effect exerted by salt presence, resulting in higher water uptake and energy storage capacity, 0.56 g/g and 342

Wh/kg, than pure MOF; they are the highest results among the three samples and also, unexpectedly, higher than literature data;

2. about 0.03% of decrease in water uptake after six cycles proves high hydrothermal stability of the material, resulting in a slight decrement in energy storage capacity, from 342 to 310 Wh/kg;
3. due to the presence of inorganic salt, kinetics are slower: thus, keeping constant the pressure at 11.6 mbar, after 4 hours, it reaches 53% of its maximum water capacity, compared to the 90% of pristine MIL-125-NH₂.

Composite MIL-125-NH₂ + SrBr₂ results let us observe that:

1. the expected lower BET surface and residual pore volume, due to salt dispersion in pure MOF matrix, are compensated by the beneficial effect exerted by salt presence, resulting in higher water uptake and energy storage capacity, 0.40 g/g and 313 Wh/kg, than pure MOF; even if the higher BET surface and residual pore volume of the SrBr₂-based composite, the CaCl₂-based one seems to overcome its performances;
2. about 1% of decrease in water uptake after six cycles proves high hydrothermal stability of the material, resulting in a slight decrement in energy storage capacity, from 313 to 287 Wh/kg;
3. due to the presence of inorganic salt, kinetics are slower: thus, keeping constant the pressure at 11.6 mbar, after 4 hours, it reaches 62% of its maximum water capacity, compared to the 90% of pristine MIL-125-NH₂.

Summarizing, what we can conclude after this preliminary experimental investigation on metal-organic frameworks for thermal energy storage is that:

- the specific surface area strongly affects the adsorption behaviour in terms of working capacity and energy storage capacity of pure MOFs; of course, industrializing their production, this drawback can be avoided;
- MOF-based CSPM (composites “salts in porous matrix”) represent very promising candidates as adsorbent materials for sorption heat storage, since they combine the lower desorption temperature and higher specific surface area of MOFs, which act as matrix for salt dispersion, thus preventing undesired deliquescence and agglomeration of salts, with the higher enthalpy of reaction and water uptake of chemisorption, due to stronger sorbate-sorbent interactions involved;
- composite MIL-125-NH₂ + (45% wt.)CaCl₂ exhibits outstanding performances, among the tested samples, showing the highest maximum water uptake and energy storage capacity under open system boundary conditions, even if at the expense of adsorption kinetics, which result the lowest measured in this work;
- both pure MOF and MOF-based composites show high hydrothermal stability, making them suitable for application in which cycling water vapour exposure is required, such as sorption heat storage.

In terms of future work, a macro-calorimetry investigation should be performed in a prototype reactor to evaluate the actual thermal performances, compared to micro-calorimetry results. In particular, at this scale, it would be possible:

- to optimize the packing density in order to maximize the energy storage density and minimize the volume occupied by the storage medium, being a concern especially in TES systems for residential building applications;
- to investigate the exact percentage of salt contained in the synthesized composites, in order to better justify their adsorption behaviour;
- to carry out a sensitivity analysis on air temperature lift, varying two main influence parameters, airflow rate and relative humidity, in order to establish which are the threshold values needed to guarantee the desired power released.

Annex A

X-ray powder diffraction

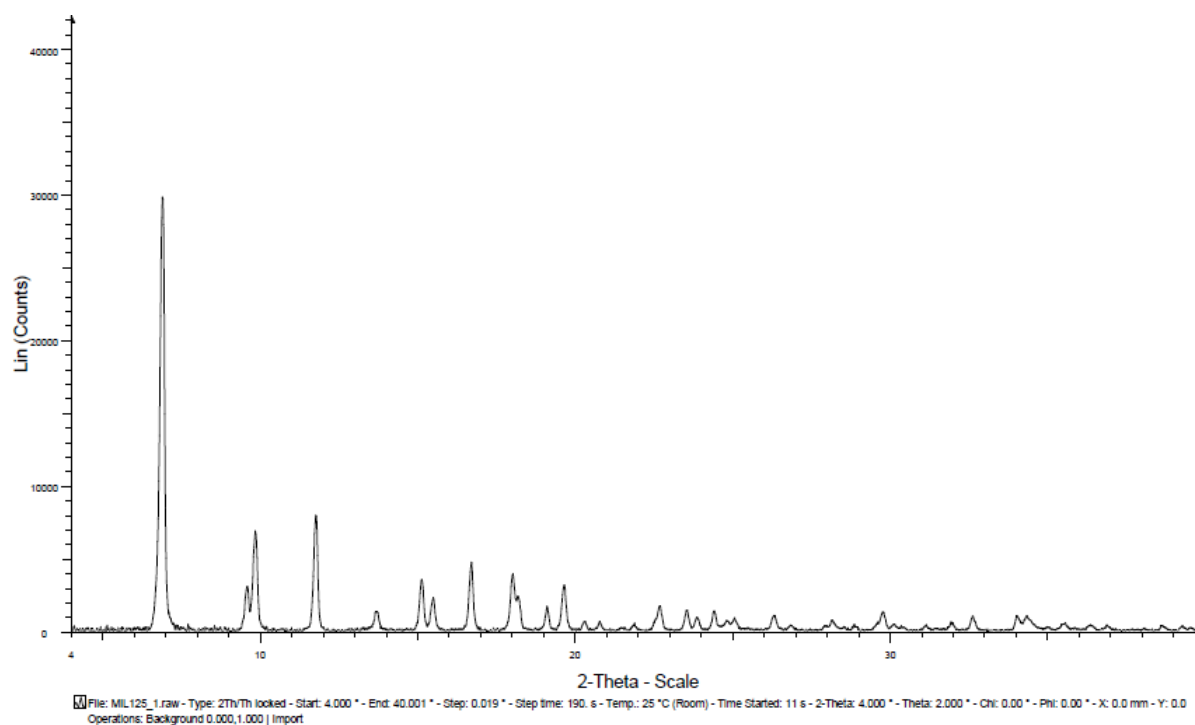
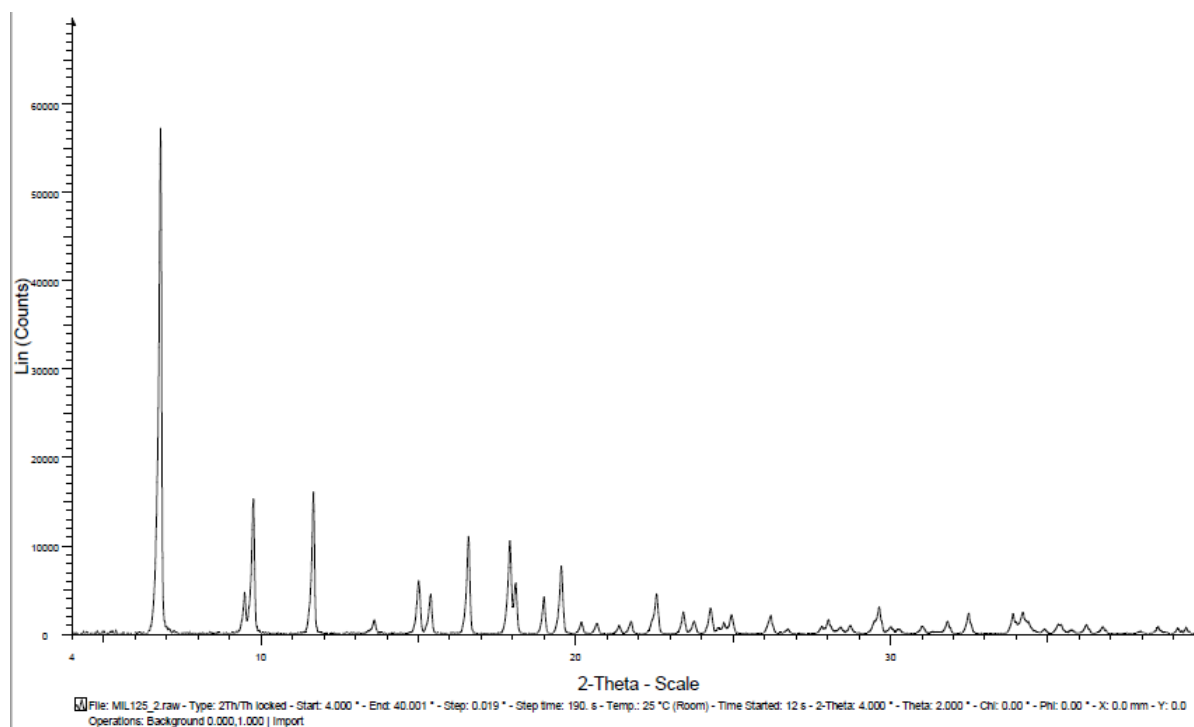
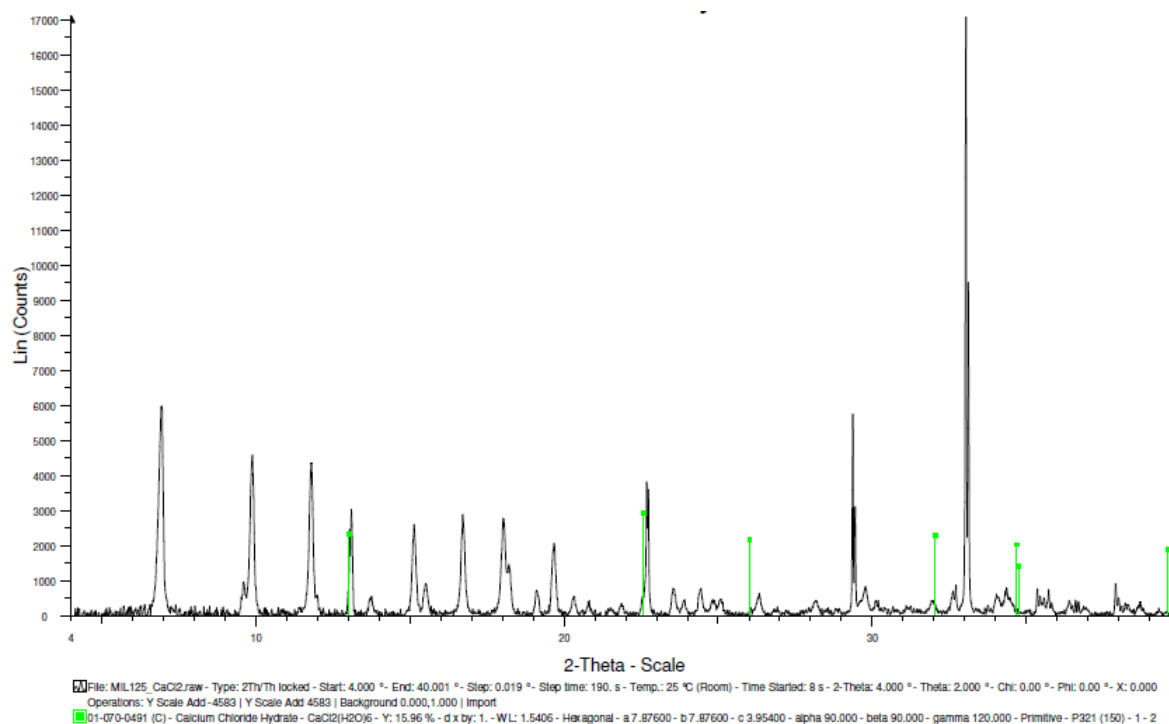


Figure 5.26. XPRD pattern of MIL-125-NH₂ sample 1.

Figure 5.27. XPRD pattern of MIL-125-NH₂ sample 2.Figure 5.28. XPRD pattern of MIL-125-NH₂ + (45%)CaCl₂ composite (CaCl₂ in green).

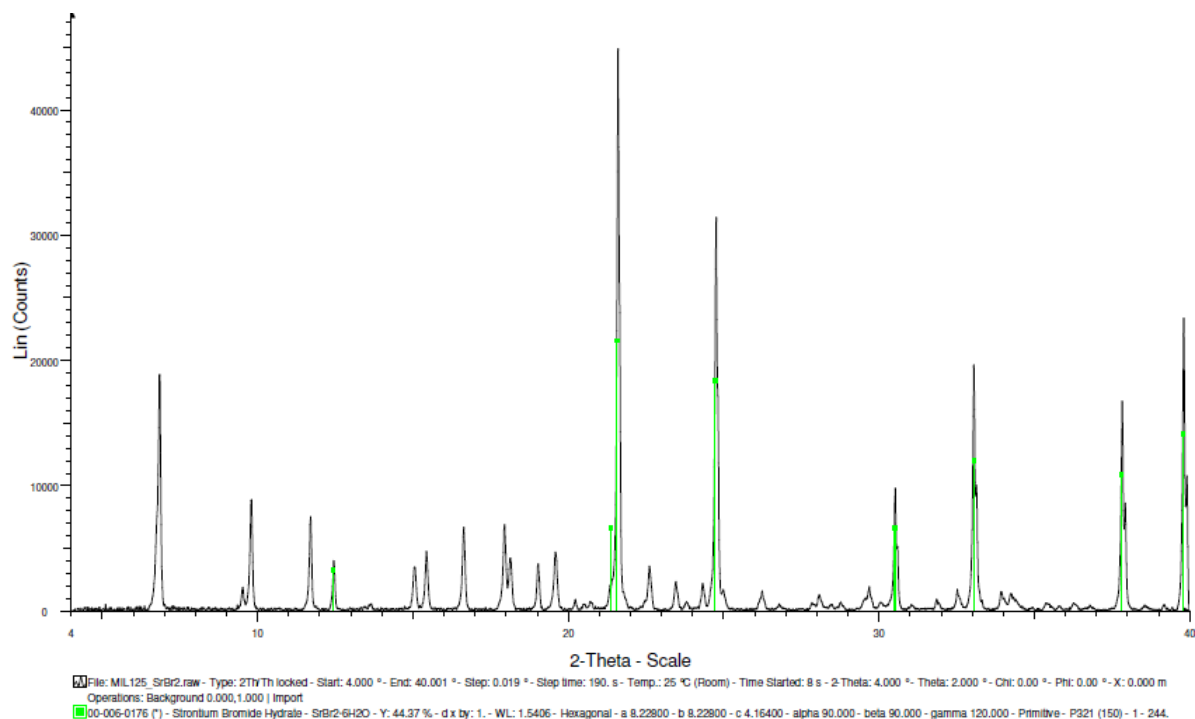


Figure 5.29. XPRD pattern of MIL-125-NH₂ + (45%)SrBr₂ composite (SrBr₂ in green).

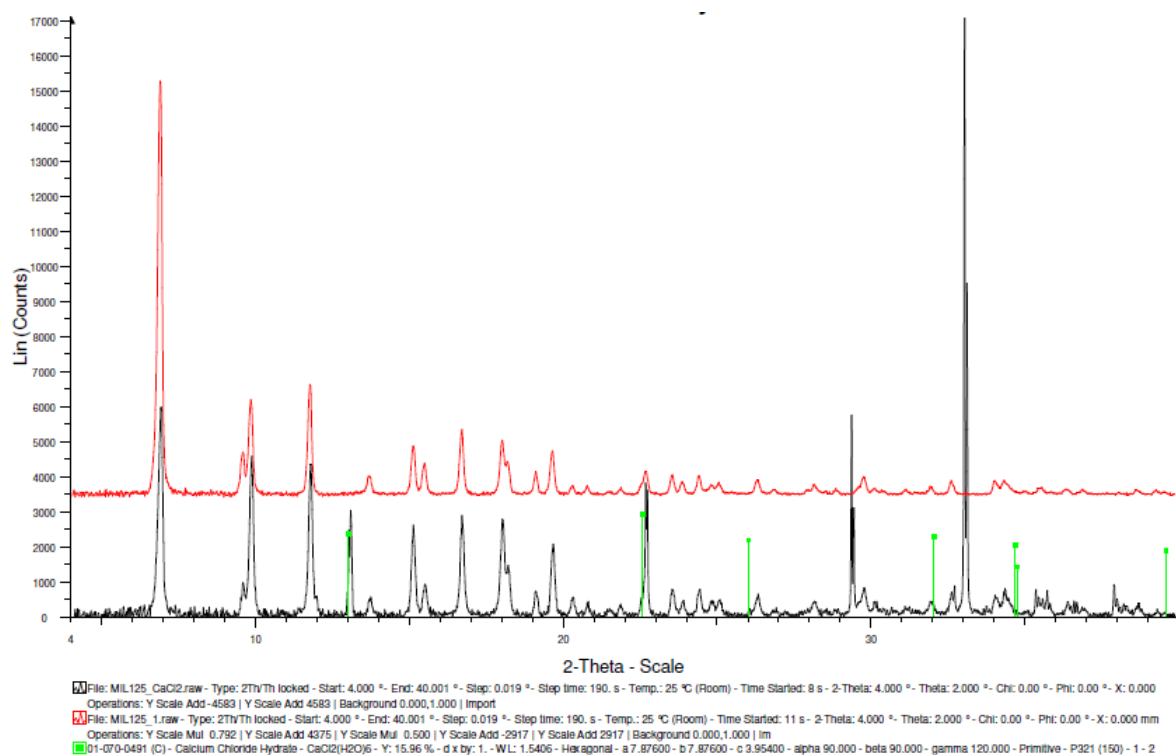


Figure 5.30. XPRD patterns: comparison between MIL-125-NH₂ + (45%)CaCl₂ (black) and MIL-125-NH₂ sample 1 (red); CaCl₂ in green.

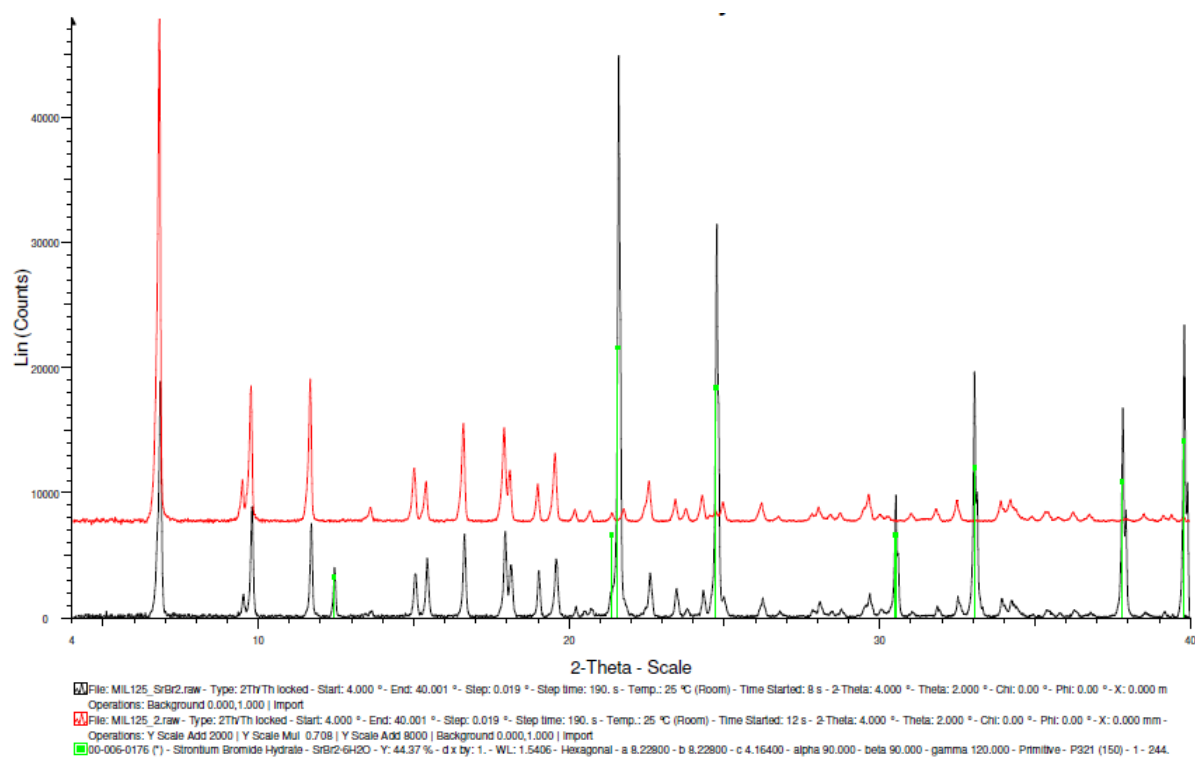


Figure 5.31. XPRD patterns: comparison between MIL-125-NH₂ + (45%)SrBr₂ (black) and MIL-125-NH₂ sample 2 (red); SrBr₂ in green.

Bibliography

- [1] European Association for Storage of Energy (EASE), *Thermal Storage Position Paper*, Brussels, July 2017
- [2] BP energy economics, *BP Energy Outlook*, 2018 edition
- [3] European commission, *Mapping and analyses of the current and future (2020 - 2030) heating/cooling fuel deployment (fossil/renewables)*, March 2016
- [4] European commission, *An EU Strategy on Heating and Cooling*, Brussels, 16/02/2016 COM(2016) 51 final
- [5] N. Yu, R.Z. Wang, L.W. Wang, *Sorption thermal storage for solar energy*, Institute of Refrigeration and Cryogenics, Shanghai Jiao Tong University, Shanghai 200240, China, 2013
- [6] IEA SHC (Solar Heating & Cooling programme), *Compact Thermal Energy Storage*, August 2015
- [7] Parfait Tatsidjodoung, Nolwenn Le Pierrès, Lingai Luo, *A review of potential materials for thermal energy storage in building applications*, LOCIE, CNRS UMR 5271- Université de Savoie, Polytech Annecy-Chambéry, Campus Scientifique, Savoie Technolac, 73376 Le Bourget-Du-Lac Cedex, France
- [8] Guruprasad Alva, Yaxue Lin, Guiyin Fang, *An overview of thermal energy storage systems*, School of Physics, Nanjing University, Nanjing 210093, China 2017
- [9] Per Alex Sørensen and Thomas Schmidt, *Design and Construction of Large Scale Heat Storages for District Heating in Denmark*, 14th International Conference on Energy Storage 25-28 April 2018, Adana, TURKEY
- [10] Ibrahim Dinçer, Marc A. Rosen, *Thermal energy storage systems and applications*, Wiley
- [11] K. Edem N'Tsoukpoe, Hui Liu, Nolwenn Le Pierrès, Lingai Luo, *A review on long-term sorption solar energy storage*, LOCIE, CNRS FRE3220-Université de Savoie, Polytech'Savoie, Campus Scientifique, Savoie Technolac, 73376 Le Bourget-Du-Lac Cedex, France
- [12] Salvatore Vasta, Vincenza Brancato, Davide La Rosa, Valeria Palomba, Giovanni Restuccia, Alessio Sapienza and Andrea Frazzica, *Adsorption Heat Storage: State-of-the-Art and Future Perspectives*, CNR—ITAE, Istituto di Tecnologie Avanzate per l'Energia "Nicola Giordano", Messina, 2018
- [13] Henninger SK, Jeremias F, Kummer H, Schossig P, Henning H- M., *Novel sorption materials for solar heating and cooling*, Energy Procedia 2012;30:279e88.
- [14] Van Essen VM, Zondag HA, Cot Gores J, Bleijendaal LPJ, Bakker M, Schuitema R, et al., *Characterization of MgSO₄ hydrate for thermochemical seasonal heat storage*, Journal of Solar Energy Engineering 2009;131:0410141e7.
- [15] Yuriy I., Aristov, *Challenging offers of material science for adsorption heat transformation: A review*, Boreskov Institute of Catalysis, Ac. Lavrentieva Av. 5, Novosibirsk

- 630090, Russia, 2011
- [16] Hongois S, Kuznik F, Stevens P, Roux J- J., *Development and characterisation of a new $MgSO_4$ -zeolite composite for long-term thermal energy storage*, Solar Energy Materials and Solar Cells 2011;95:1831e7.
- [17] Jänchen J, Ackermann D, Stach H, Brösicke W., *Studies of the water adsorption on zeolites and modified mesoporous materials for seasonal storage of solar heat*, Solar Energy 2004;76:339e44.
- [18] H. Wu, S. Wang and D. Zhu, Sol. Energy, 2007, 81, 864.
- [19] Anastasia Permyakova, Sujing Wang, Emilie Courbon, Farid Nouar, Nicolas Heymans, Pierre D'Ans, Nicolas Barrier, Pierre Billefont, Guy De Weireld, Nathalie Steunou, Marc Frère and Christian Serre, *Design of salt-metal organic framework composites for seasonal heat storage applications*, Journal of Materials Chemistry, 2017
- [20] N'Tsoukpoe KE, Le Pierrès N, Luo L., *Numerical dynamic simulation and analysis of a lithium bromide/water long-term solar heat storage system* Energy 2012;37:346e58.
- [21] Xu SM, Zhang L, Liang J, Du R., *Variable mass energy transformation and storage (VMETS) system using NH_3 - H_2O as working fluid, part 1: modeling and simulation under full storage strategy*, Energy Conversion and Management 2007;48:9e26.
- [22] Xu SM, Zhang L, Liang J, Du R., *Variable mass energy transformation and storage (VMETS) system using NH_3 - H_2O as working fluid. Part 2: modeling and simulation under partial storage strategy*, Energy Conversion and Management 2007;48:27e39.
- [23] Ahmed Elsayed, Eman Elsayed, Raya AL-Dadah, Saad Mahmoud, Amr Elshaer, Waseem Kaialy, *Thermal energy storage using metal-organic framework materials*, Applied Energy 186 (2017) 509–519
- [24] C. Bales, P. Gantenbein, A. Hauer, H.-M. Henning, D. Jaenig, H. Kerskes, T. N´uñez and K. Visscher, Rep. IEA Sol. Heat. Cool. Program., 2005, p. 32
- [25] Kerskes H, Mette B, Asenbeck S, Drück H, Müller-Steinhagen H., *Experimental and numerical investigations on thermochemical heat storage*, In: Proceedings of second International Conference on Solar Heating, Cooling and Buildings (EUROSUN); 2010.
- [26] Posern K, Kaps C. Calorimetric studies of thermochemical heat storage materials based on mixtures of $MgSO_4$ and $MgCl_2$, Thermochemica Acta 2010;502:73e6.
- [27] Rd Boer, Haije WG, Veldhuis JBJ, *Determination of structural, thermodynamic and phase properties in the Na_2S - H_2O system for application in a chemical heat pump*, Thermochemica Acta 2003;395:3e19.
- [28] Lahmidi H, Mauran S, Goetz V., *Definition, test and simulation of a thermochemical storage process adapted to solar thermal systems*, Solar Energy 2006;80:883e93.
- [29] Zondag H, Kikkert B, Smeding S, Rd Boer, Bakker M., *Prototype thermochemical heat storage with open reactor system*, Applied Energy 2013.
- [30] Fanny Trausel, Ard-Jan de Jong, Ruud Cuypers, *A review on the properties of salt hydrates for thermochemical storage*, SHC 2013, Freiburg, Germany.
- [31] N. Yu, R. Z. Wang, Z. S. Lu and L. W. Wang, Chem. Eng. Sci., 2014, 111, 73.
- [32] Marco Leenders, *Investigation of Metal Organic Frameworks for seasonal thermal energy storage - A comparison of a number of MOFs on energy storage density*, Master thesis, 2017
- [33] Stéphanie Hongois. Stockage de chaleur inter-saisonnier par voie thermochimique pour le chauffage solaire de la maison individuelle. Architecture, aménagement de l'espace. INSA de Lyon, 2011. Français. jNNT : 2011ISAL0033j. jtel-00665612j
- [34] Yang Zhao, Zhongxin Song, Xia Li, Qian Sun, Niancai Cheng, Stephen Lawes,

- Xueliang Sun, *Metal organic frameworks for energy storage and conversion*, Energy Storage Materials 2 (2016) 35–62
- [35] Felix Jeremias, Dominik Fröhlich, Christoph Janiak and Stefan K. Henninger, *Water and methanol adsorption on MOFs for cycling heat transformation processes*, New J. Chem., 2014, 38, 1846
- [36] Yuriy I. Aristov, *Challenging offers of material science for adsorption heat transformation: A review*, Applied Thermal Engineering 50 (2013) 1610-1618
- [37] Jérôme Canivet, Alexandra Fateeva, Youmin Guo, Benoit Coasne, and David Farrusseng, *Water adsorption in MOFs: fundamentals and applications*, DOI: 10.1039/x0xx00000x, 2012
- [38] Jérôme Canivet, Jonathan Bonnefoy, Cécile Daniel, Alexandre Legrand, Benoit Coasne and David Farrusseng, *Structure–property relationships of water adsorption in metal–organic frameworks*, New J.Chem., 2014, 38, 3102
- [39] Muhammad Sohail, Yang-No Yun, Eunkyung Lee, Sang Kyum Kim, Kanghee Cho, Jong-Nam Kim, Tae Woo Kim, Jong-Ho Moon, and Hyunuk Kim, *Synthesis of Highly Crystalline NH₂-MIL-125 (Ti) with S-Shaped Water Isotherms for Adsorption Heat Transformation*, Energy Materials Laboratory, Green Fuel Laboratory, and Greenhouse Gas Laboratory, Korea Institute of Energy Research, 152 Gajeong-ro, Yuseong-gu, Daejeon, 34129, Republic of Korea; Advanced Energy Technology, University of Science and Technology, 217 Gajeong-ro, Yuseong-gu, Daejeon 34113, Republic Of Korea.
- [40] Gregory E. Cmarik, Min Kim, Seth M. Cohen, and Krista S. Walton, *Tuning the Adsorption Properties of UiO-66 via Ligand Functionalization*, School of Chemical and Biomolecular Engineering, Georgia Institute of Technology, 311 Ferst Drive NW, Atlanta, Georgia 30332, United States; Department of Chemistry and Biochemistry, University of California, San Diego, La Jolla, California 92093, United States
- [41] Anupam Khutia, Holger Urs Rammelberg, Thomas Schmidt, Stefan Henninger, and Christoph Janiak, *Water Sorption Cycle Measurements on Functionalized MIL-101Cr for Heat Transformation Application*, Germany, 2013
- [42] Felix Jeremias, Vasile Lozan, Stefan K. Henninger and Christoph Janiak, *Programming MOFs for water sorption: amino-functionalized MIL-125 and UiO-66 for heat transformation and heat storage applications*, RSC Publishing, 2 July 2013
- [43] Stefan K. Henninger, Felix Jeremias, Harry Kummer, and Christoph Janiak, *MOFs for Use in Adsorption Heat Pump Processes*, DOI: 10.1002/ejic.201101056
- [44] N. C. Burch, H. Jasuja, K. S. Walton, Chem. Rev. 2014, 114, 10575
- [45] Anastasia Permyakova. Metal Organic Frameworks based materials for long term solar energy storage application. Material chemistry. Université Paris-Saclay, 2016. English. jNNT : 2016SACLV031j. jtel-01806324j
- [46] Fröhlich, Henninger, Janiak, *Multicycle water vapour stability of microporous breathing MOF aluminium isophthalate CAU-10-H*, Dalton Trans., 2014, 43, 15300
- [47] Eman Elsayed, Raya AL-Dadah, Saad Mahmoud, Paul.A. Anderson, Ahmed Elsayed, Peter G. Youssef, *CPO-27(Ni), aluminium fumarate and MIL-101(Cr) MOF materials for adsorption water desalination*, UK, 2016
- [48] Amandine Cadiou, Ji Sun Lee, Daiane Damasceno Borges, Paul Fabry, Thomas Devic, Michael T. Wharmby, Charlotte Martineau, Damien Foucher, Francis Taulelle, Chul-Ho Jun, Young Kyu Hwang, Norbert Stock, Martijn F. De Lange, Freek Kapteijn, Jorge Gascon, Guillaume Maurin, Jong-San Chang and Christian Serre,

- Design of Hydrophilic Metal Organic Framework Water Adsorbents for Heat Reallocation*, Adv. Mater. 2015, 27, 4775–4780
- [49] Lide DR. CRC Handbook of chemistry and physics. CRC Press; 2012.
- [50] Felix Jeremias, Anupam Khutia, Stefan K. Henninger and Christoph Janiak, *MIL-100(Al, Fe) as water adsorbents for heat transformation purposes— a promising application*, J. Mater. Chem., 2012, 22, 10148
- [51] Eman Elsayed, Raya AL-Dadah, Saad Mahmoud, Ahmed Elsayed, Paul A. Anderson, *Aluminium fumarate and CPO-27(Ni) MOFs: Characterization and thermodynamic analysis for adsorption heat pump applications*, UK, 2016
- [52] Salil U. Rege and Ralph T. Yang, *Corrected Horvath-Kawazoe Equations for Pore-Size Distribution*, Dept. of Chemical Engineering, University of Michigan, Ann Arbor, MI 48109